Computational Fluid Dynamics Modelling of PEM Fuel Cells to Investigate Transport Limitations

Sheikh Zahidul Islam

A thesis submitted in partial fulfilment of the requirements of the Robert Gordon University for the degree of Doctor of Philosophy.

April 2012

Title of Research Project:

Computational Fluid Dynamics Modelling of PEM Fuel Cells to Investigate Transport Limitations

Principal Supervisor: Dr. Mamdud Hossain

Supervisor's details:

Dr. Mamdud Hossain and Prof. Pat Pollard

School of Engineering, Robert Gordon University, Schoolhill,

AB10 1FR, Aberdeen, UK

Funding Organization:

Northern Research Partnership (NRP) and School of Engineering,

the Robert Gordon University, Aberdeen, United Kingdom.

Acknowledgements

I would like to take the opportunity to express my gratitude to all who have made substantial contributions towards my PhD thesis.

First of all, I would like to acknowledge my principal supervisor **Dr Mamdud Hossain** for giving me the opportunity to be a part of this project and. He supported my plans to continue the work and his constructive comments which led me to reconsider and improve many areas of my thesis. His constructive comments, encouragements, enthusiasm and expertise of this subject helped guiding me to complete the thesis work.

I would like to give thanks to **Professor Pat Pollard** for her encouragement and support throughout the project. Thanks go to **Northern Research Partnership (NRP)** for the financial support throughout the project which enables me to continue this PhD. I am grateful to **School of Engineering,** Robert Gordon University for providing me the tuition fees difference for my PhD study. I am also grateful to all my friends for valuable discussion and made my life enjoyable in RGU. I would like to thank **Tecplot** for providing me post-processing software for free throughout my studies.

Finally, I cannot express my gratefulness enough to my wife **Dr. Tahmina Arifa**, my daughter **Afsheen Aleena,** my father-in-law **MD. Shafiqul Islam** and rest of my family for their patience and endless moral support throughout my PhD study. Sometimes words are not enough to describe everything.

Dedication

This thesis is dedicated to my Father, Late **Sheikh Shahidul Islam**

Abstract

Modern technological advancements in our lifestyle have caused a significant increase in the consumption of energy. With this growing demand, people are more concerned about the rational use of existing limited energy and searching for alternative forms of environmentally friendly energy sources to reduce polluting emissions. Proton Exchange Membrane (PEM) fuel cell has shown and demonstrated that potential to be a suitable alternative power source because of its simplicity of design, load following capabilities, efficiency, feasibility and quick start-up. Although having these splendid advantages, cost and durability of PEM fuel cells are one of the major challenges that needed to be overcome.

Three-dimensional single-phase and multi-phase isothermal PEM fuel cell models have been developed to investigate the transport limitations of fresh reactants and its effect on cell performance. The governing equations (continuity, momentum and species transport) with appropriate source terms were solved using computational fluid dynamics (CFD) technique. A user defined function (UDF) code was developed considering source terms for porous zones, effective diffusivity models for species transport inside cells and electrochemical reactions at catalyst layers to predict cell voltage at an average current density. The average current density and net water transfer coefficient, used to calculate the source terms, were calculated using auxiliary equations and linked to the solver through UDFs. Parametric studies were performed to determine the optimal operating conditions and geometrical design of PEM fuel cell. The simulation results show that gas diffusion layer permeability has no effect on cell performance for a value lower than 10^{-11} m^2. GDL porosity is one of the major design parameters which have significant influence on limiting current density, hence on cell performance. Land area width of PEM fuel cell shows

influence on cell performance. Low membrane thickness provides higher cell performance and approximately 50% reduction in membrane thickness results approximately 100% improvement in cell performance at high current density of 1.0 Acm^{-2}.

Bruggeman correlation was used in most of previous modelling work for explaining the diffusion of species though porous GDL and CL, but this thesis considered other types of effective diffusion models and investigated the effect of diffusion models on cell performance at high current densities. Tomadakis and Sotirchos (1993) anisotropic model produces cell voltage much closer to the experimental values. Therefore, anisotropic diffusion model should be utilized in PEM fuel cell modelling to minimize modelling uncertainties.

A two-phase flow, steady-state, three-dimensional PEM fuel cell model considering the phase change effect of water has been developed in the final phase of the thesis. Flooding inside the cell was captured at high current density using the model for a condensation value of 10.0 s^{-1}. Finally, parametric studies were performed based on isotropic and anisotropic GDL permeability cases. Modelling results suggest that isotropic permeability cases have strong influence on cell performance compared to anisotropic cases at high current density.

Table of Contents

List of Figures

List of Tables

Nomenclature

a_k	water activity
A	specific area of the anode / cathode catalyst layer (m^{-1})
C	molar concentration of species (mol m^{-3})
D	diffusion coefficient of species (m^2 s^{-1})
E	equilibrium thermodynamic potential (V)
F	Faraday constant (96485.309 C mol^{-1})
H	height (m)
i	reaction rate (Am^{-3})
I	average current density (Acm^{-2})
K	permeability of porous layers (m^2)
k_c	condensation rate (s^{-1})
k_m	phase conductivity of membrane (S m^{-1})
L	length (m)
M	molar mass (kg mol^{-1})
$M_{m,dry}$	dry mass of membrane (Kg mol^{-1})
n	electron number for reactions
n_d	electro-osmotic drag coefficient
P	pressure (Pa)
R	gas constant (8.314 J mol^{-1} K^{-1})
RH	relative humidity (%)
S	source term
s	liquid water saturation
t_m	thickness of membrane (m)
T	temperature (K)
$\boldsymbol{u}$	velocity vector (m s^{-1})
V_{cell}	cell voltage (V)
W	width (m)
X	molar fraction

Greek symbols

α	net water transfer coefficient

ε	porosity
η	overpotential (V)
μ	viscosity (kg m^{-1} s^{-1})
ρ	density (kg m^{-3})
ω	species mass fraction
ζ	stoichiometric ratio

Subscripts and superscripts

0	before diffusion layer
a	anode
act	activation
av	average
c	cathode
conc	concentration
d	diffusion layer
eff	effective
el	electron
H_2	hydrogen
k	species
L	limiting
lq	liquid
m	membrane
O_2	oxygen
ohm	ohmic polarization
pro	proton
ref	reference
sat	saturation
wv	water vapour

1

Chapter 1: Introduction

Modern technological advancements in our lifestyle have caused a significant increase in the consumption of energy. With this growing demand, people are more concerned about the rational use of existing limited energy and searching for alternative forms of environmentally friendly energy sources to reduce pollution. According to world energy outlook 2010 (INTERNATIONAL ENERGY AGENCY, 2010), the total energy demand in the world is approximately 12271 million tonnes of oil equivalent (Mtoe). The sources of energies are coal (3315 Mtoe), oil (4059 Mtoe), gas (2596 Mtoe), nuclear (712 Mtoe), biomass (1225 Mtoe), hydro (276 Mtoe) and other forms of renewable energy (89 Mtoe). Over reliance on fossil fuels to meet growing energy demand already has major consequence in terms of climate change and increase in emission of CO_2. The supplies of modern renewable energy have shown the potential to meet the future demand for clean energy in this context. The supply of modern renewable energy ("hydro, wind, solar, geothermal, modern biomass and marine energy") is projected to increase from 840 Mtoe in 2008 to between

1900 Mtoe and nearly 3250 Mtoe in 2035, depending on the energy scenario. (INTERNATIONAL ENERGY AGENCY 2010)

Hydropower is leading the modern renewable in terms of electricity production (900 TWh increase between 2000 and 2008). However, other sources such as, wind, solar, geothermal and marine powers are growing rapidly in recent years and showing potential to contribute in primary energy supply. Among these sources, wind turbine technology has gained technical development and the wind energy installed capacity has reached 175 Gigawatt in 2010 (WORLD WIND ENERGY ASSOCIATION, 2011). Solar photovoltaic (PV) electricity production is also growing rapidly in recent years compared to wind energy. However, the main challenges of wind and solar energy are the intermittent availability and variation in energy density. (INTERNATIONAL ENERGY AGENCY, 2010)

In this regard, fuel cells are one of the clean sources of energy that can make real contribution in the reduction of CO_2 emission. Among many fuel cells (such as alkaline, direct methanol, solid oxide, molten carbonate), proton exchange membrane (PEM) fuel cell is the most versatile that can be used in both residential and transport sectors. A comparison of fuel cell technologies is shown in the Table 1.1. Proton Exchange Membrane (PEM) fuel cell has shown and demonstrated that potential to be a suitable alternative power source because of its simplicity of design, load following capabilities, efficiency, feasibility and quick start-up. Although PEM fuel cells received much attention at fundamental research and technology development levels, the commercialization of PEM fuel cells are still in initial stages because of its relatively high cost of fuel cell prototypes, durability, hydrogen storage and hydrogen fuel infrastructure and insufficient lifetime for stationary power generation. (Barbir 2007, Lum 2003, Larminie and Dicks 2003)

Table 1.1 Comparisons of fuel cell technologies (U.S. DEPARTMENT OF ENERGY 2011).

Types of Fuel cell	Operating Temperature	Typical Stack Size	Efficiency	Applications
Proton Exchange Membrane Fuel Cell (PEMFC)	50-80°C	< 1 kW–100 kW	35-60% depending on application	• Automobiles, light duty vehicles, • Backup power • Portable power • Distributed generation
Alkaline Fuel Cell (AFC)	90-100°C	10 kW–100 kW	60%	• Military • Space
Phosphoric Acid Fuel Cell (PAFC)	150-200°C	400 kW	40%	• Distributed generation
Molten Carbonate Fuel Cell (MCFC)	600-700°C	300 kW-3 MW	45-50%	• Electric utility • Distributed generation
Solid Oxide Fuel Cell (SOFC)	700-1000°C	1 kW–2 MW	60%	• Auxiliary power • Electric utility • Distributed generation

One of the major solutions to reduce cost is to have cheaper catalyst layers with reduced Pt. loading. In addition, different membrane thicknesses play a key role to the cost of PEM fuel cell. In order to develop a cost-competitive PEM fuel cell system, researchers' are performing material research to innovate new design and material for catalyst layer and membrane. An alternative approach to reduce cost and improve durability is to have design and operation optimisation through fundamental understandings. PEM fuel cell experimental

researches only address the global parameters such as polarization characteristics at different current densities by examining a voltage-current curve. However, detailed understanding of species transport inside the PEM fuel cell is not possible due to the size constraint. The operation of PEM fuel cell not only involves electrochemical reactions but also current distribution, fluid mechanics, species transport, water and thermal management. It is difficult to understand these complex electrochemical reactions and the transport limitations of fresh reactants using experiments. While, modelling of PEM fuel cell provides better understanding of these electrochemical reactions and transport phenomena. However, uncertainty associated with available models make it difficult to predict fuel cell performance accurately at higher current densities. That's why recent PEM fuel cell research focus is to have better and complete understanding of the fuel cell operation by improving available models and hence to reduce the cost. (Larminie and Dicks 2003, Lum 2003, Barbir 2007, U.S. DEPARTMENT OF ENERGY 2011, Yu et al. 2009, Yuan et al. 2010, Min 2010, Liu, Lou and Wen 2010, Jung, Lee and Chen 2012)

1.1 Operating principle of a PEM fuel cell

A schematic diagram of a PEM fuel cell configuration and basic operating principle is shown in Figure 1.1. A proton exchange membrane fuel cell works as an electro-chemical device and the membrane is the heart of the PEM fuel cell. It conducts protons but at the same time it is impermeable to gases. The membrane is placed between two porous, electrically conductive electrodes. The platinum supported on carbon catalyst layer, where the electrochemical reactions occur, act as an interface between the porous electrode and the membrane. The membrane separates the PEM fuel cell into two

sides. One is the anode side (left side in Figure. 1.1) and another is cathode side (Right side in Figure.1.1). (Barbir 2007)

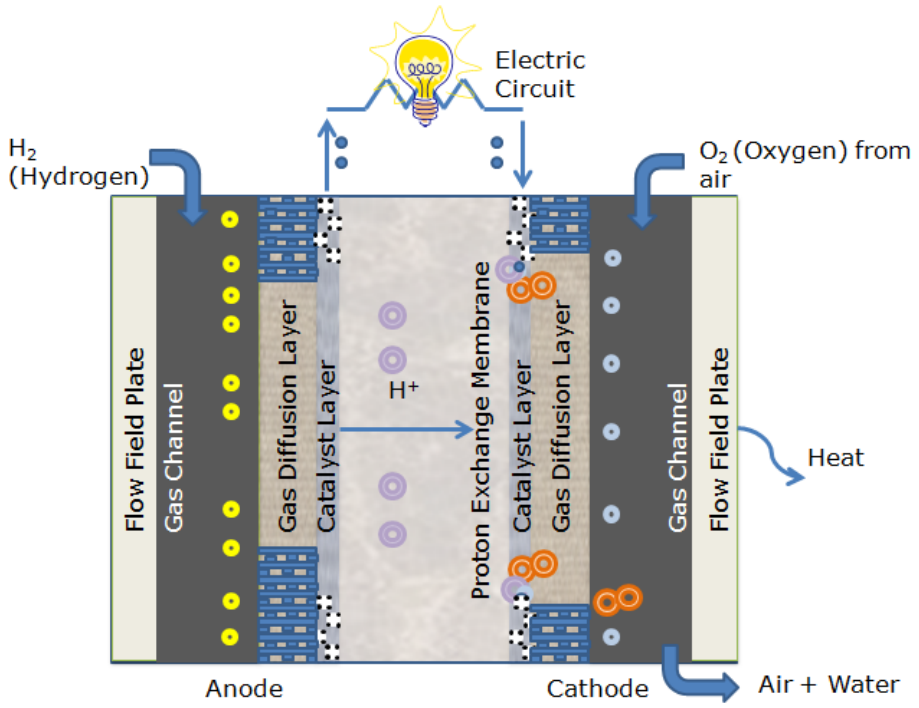

Figure 1.1 Schematic diagram of a PEM fuel cell showing anode (left) and cathode (right) side.

Hydrogen, fed on the anode side, splits into proton and electron at the catalyst layer. Protons travel through the membrane to the cathode side and the electron travel through the electrode and through the external circuit and finally return to cathode side of the PEM fuel cell. At the same time, oxygen is fed to the cathode side and water is created as output due to electrochemical reaction. Thus continuous electron flow is observed in the external circuit due to these simultaneous reactions. Typically, "a PEM fuel cell operating at atmospheric pressure should generate more than 0.6 A/cm^2 at 0.6 V and the operating temperature is between 60^{o}C and 80^{o}C" (Barbir 2007 p.29). A fuel cell stack is formed by stacking up a large number of single PEM fuel cells. Water and heat are generated as a by-product

of the continuous electrochemical reactions. PEM fuel cell efficiency depends upon the appropriate water and thermal management of the cell. In order to maintain desired temperature and operating conditions inside the cell and stack, water and heat must be taken away from the cells and from the stack. Otherwise, significant reduction of cell efficiency was observed. (Barbir 2007)

The basic PEM fuel cell components and their features are shown in the following Table 1.2.

Table 1.2 Basic PEM fuel cell components (Spiegel 2008 p. 4, Table 1-1, Barbir 2007).

Component	Description	Common Types
Proton exchange membrane (PEM)	Transfer proton from anode to cathode side and impermeable to reactant transport	Nafion membranes
Catalyst layers (CL)	Electrochemical reaction occurs. Hydrogen breaks to proton and electron in anode side. Proton combines with oxygen and produce water in the cathode side.	Platinum catalyst (Small Platinum particles on large carbon catalyst surface)
Gas diffusion layers (GDL)	Allows reactants to travel from gas channels to catalyst layers and collects electron	Carbon fiber paper or carbon cloth
Flow field or Bipolar plates	Distributes reactants to gas diffusion layers	Graphite sheet, carbon polymer composites
Gaskets	Provides sealing to prevent leakage	Silicone, Teflon and Graphite
End Plates	Provide structural support for stack	Stainless steel, graphite

1.2 Polarization Characteristics

The conversion of chemical energy into electrical energy happens simultaneously inside fuel cell. The overall chemical reactions taking place inside a PEM fuel cell are as follows (Spiegel 2008):

Anode: $H_2 \rightarrow 2H^+ + 2e^-$

Cathode: $½\ O_2 + 2H^+ + 2e^- \rightarrow H_2O$

Overall: $H_2 + ½\ O_2 \rightarrow H_2O$ + electric energy + waste heat

Voltage losses observed in a fuel cell are illustrated in the following Figure.1.2. When electrical energy is drawn from the cell, the cell potential is dropped due to irreversible losses (polarization, overpotential and overvoltage losses).

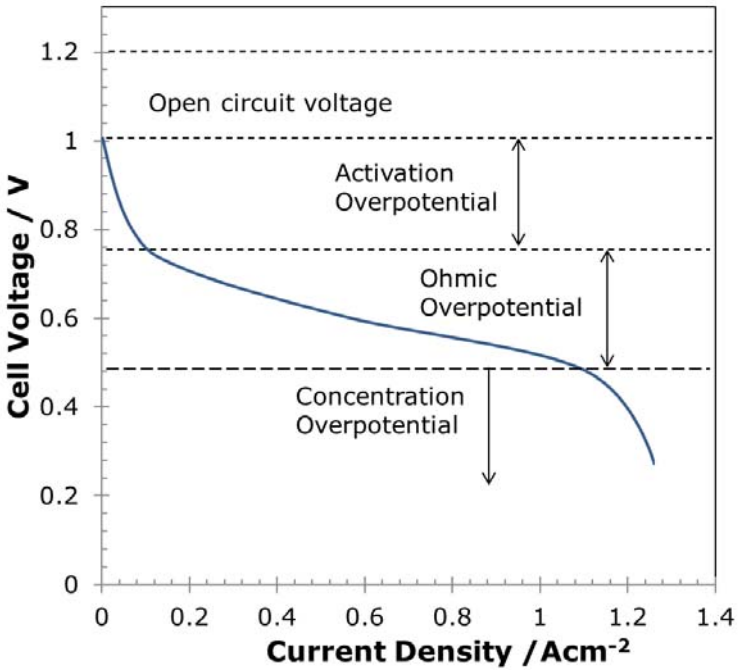

Figure 1.2 Polarization curve of a PEM fuel cell showing voltage losses.

Activation overpotential (η_{act}):

The activation overpotential arises from slowness of reactions and electron transfer to and from the electrode. The hydrogen oxidation in the anode side is faster compared to the oxygen reduction at cathode side. Therefore, cathode side conditions control the overall reaction rate inside fuel cell. The activation overpotential is a function of local current density, exchange current density and concentration of oxygen. The activation overpotential is expressed by Butler-Volmer equation. (Min 2009)

Ohmic Overpotential (η_{ohm}):

The ohmic overpotential occurs due to resistance of the porous electrode to electron and resistance of membrane to proton transfer. (Min 2009)

Concentration Overpotential (η_{conc}):

At high current densities, polarization losses are dominated by concentration overpotential which is caused by slow diffusion of gas phase through the porous regions. (Min 2009)

1.3 Challenges in Efficient Fuel Cell Design and Performance Optimization

A proton exchange membrane enables hydrogen proton to travel from anode to cathode side as long as the membrane is properly hydrated. A well-hydrated membrane is highly proton conductive, which results in lower cell resistance and higher cell voltage. If the membrane becomes dehydrated during the fuel cell operation, then its proton conductivity decreases and poor performance of the fuel cell is observed. However too much water inside the cell cause flooding and block the pores in gas diffusion layer and electrodes. Therefore a

proper balance of water inside the cell is essential to achieve maximum efficiency. Sometimes a good engineering design can be useful to achieve suitable hydration, but several complications associated to the fuel cell operation make it more difficult to understand in real operation. (Larminie and Dicks 2003)

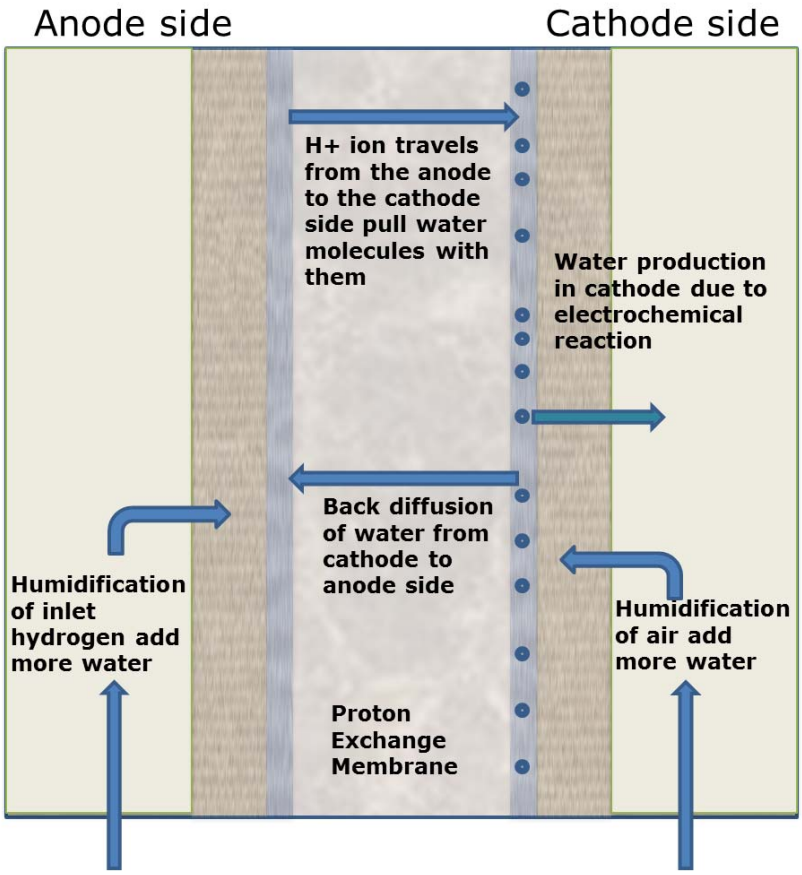

Figure 1.3 Water movements to, within, and from the membrane of a PEM fuel cell.

When an H+ ion travels from the anode to the cathode side, the ions pull water molecules with them and eventually complete dried out anode side is observed at higher current densities. This effect is known

as the electro-osmotic drag. The operating temperature of a PEM fuel cell is over 50^{o} C. Drying out of air in the electrodes is observed at that temperature range, as the water production by electrochemical reaction is slower than the required amount. Humidification of inlet air is one of the possible solutions for this complexity to improve fuel cell performance, but it is effectively adding a by-product of the reaction to the inputs in the process. Again, Back diffusion of water from cathode to anode side depends on the relative humidity. Figure 1.3 shows these complex water movements inside the PEM fuel cell. (Larminie and Dicks 2003)

The operation of PEM fuel cell not only involves electrochemical reactions but also current distribution, fluid mechanics, species transport, water and thermal management. It is difficult to understand these complex electrochemical reactions and transport limitations of fresh reactants using experiments. Therefore, it is essential to develop a complete mathematical PEM fuel cell model that would provide better understanding of these electrochemical reactions and transport phenomena in PEM fuel cells.

1.4 Research Aims and Objectives

The main focus of this PhD thesis is to develop three-dimensional models of a single PEM fuel cell and investigate the fuel cell performance for steady state condition using CFD. The aims and objectives of the PhD work are summarized as follows:

Aims:

To develop a comprehensive PEM fuel cell model for better understanding the electrochemical reactions and transport phenomena.

Objectives:

i. Develop an improved single-phase flow PEM fuel cell model (Development of sub-models for gas diffusion layers, membrane and catalyst layers and integration of sub-models into CFD based model);

ii. Investigate the complex interactions of different electrochemical processes and transport phenomena under steady state conditions for various operating conditions and design parameters;

iii. Investigate the uncertainty of modelling accuracy related to effective diffusivity and permeability of gas diffusion layers;

iv. Develop a two-phase flow PEM fuel cell model to take into account liquid/water vapour phase change for better performance prediction at high current density and validation of model against experimental results.

1.5 Outline of the thesis

The outline of the thesis is provided below:

Chapter 1: An introduction to world energy scenario and fuel cells potentials to meet the future energy demand are provided in the first sections. Transport limitations in PEM fuel cells are discussed. The aim and objectives for the thesis are described.

Chapter 2: Computational modelling of PEM fuel cell is a valuable tool for design optimization and developing efficient fuel cells as the models provide information about mass transport process in porous layer, validation of model results to improve the model, effect of operating

parameters, and design constraints of fuel cell components. A brief literature review of existing single-phase and multi-phase PEM fuel cell modelling work are described in the chapter.

Chapter 3: In this chapter, the governing equations and auxiliary equations for modelling PEM fuel cells are explained. The numerical procedure used for solving the equations is presented. A brief description of the UDF code is also presented. Finally modelling parameters are provided with appropriate boundary conditions.

Chapter 4: In this chapter, the predicted cell performance using the developed single-phase PEM fuel cell model is discussed. Predicted cell performance is validated with experimental results. The species mass fraction distribution for oxygen and water vapour are studied and possible dehydration areas are identified. A parametric study is performed based on operating conditions and design parameters are presented.

Chapter 5: Bruggeman model has widely been used to represent species diffusion through porous GDL and CL. In this chapter, Bruggeman model is compared against diffusion models based on particle porous media, multi-length scales particle and percolation type correlation. The effects of these models on cell performance prediction are discussed in the chapter.

Chapter 6: A multi-phase model based on water vapour to liquid phase change has been created and reactants distributions along the channel are presented in this chapter. The effects of condensation rate and saturation models on PEM fuel cell performance predictions are discussed.

Chapter 7: The permeability of gas diffusion layer (GDL) is one of the significant parameters that influence the PEM fuel cell performance. The effect of anisotropic GDL permeability on PEM fuel cell using multi-phase model is presented in this chapter.

Chapter 8: The chapter summarizes the outcomes of the thesis. A conclusion and future work is also presented in the chapter.

2

Chapter 2: Literature Review

Computational fluid dynamics (CFD) modelling of PEM fuel cell is a valuable tool for design optimization and developing efficient fuel cells as the models provide information about mass transport process in porous layers, validation of model results to improve the model, effect of operating parameters, and design constraints of fuel cell components.

Over the last two decades, empirical studies are carried out to investigate the PEM fuel cells performance, control and optimization. Most of the pioneering PEM fuel cell models are either two-dimensional or single-phase (for example, Gurau, Liu and Kakac 1998, Nguyen and White 1993, Yi and Nguyen 1998, Singh, Lu and Djilali 1999, Dutta, Shimpalee and Van Zee 2001) which are not sufficient to investigate the fuel cell performance at high current density. Furthermore, the water produced during electrochemical reactions inside the cell is considered to be in vapour phase. As the operating temperature of the PEM fuel cell is within the range of 50^{o}C to 80^{o}C, both the vapour and liquid phase of water need to be considered. Therefore, a two-phase

PEM fuel model is essential to investigate the water transport and transport limitations inside the cell. The following sections describe a brief literature review of existing single-phase and multi-phase PEM fuel cell modelling works.

2.1 Single-Phase modelling of PEM fuel cells

Ju, Meng and Wang (2005) investigated the water management by developing a three dimensional, non-isothermal PEM fuel cell model based on previous fuel cell modelling work (Um, Wang, and Chen 2000, Gu and Wang 2000). The authors identified that thermal conductivity, relative humidity and operating cell voltage are the critical parameters affecting the cell performance. According to their observation, fully humidified operating conditions can cause severe electrode flooding. Although they suggested using high membrane temperature to alleviate flooding, no validation of the hypothesis against experimental data was presented in the paper.

Ju et al. (2005) further investigated the effect of humidity on cell performance using the above model (Ju, Meng and Wang 2005). The authors found that fully humidified anode side shows higher current density distribution at the same voltage along channel compared to other inlet humidity combination. A good agreement between simulation results and experimental results (Dong et al. 2005) was achieved. Carcadea et al. (2007) investigated the effect of flow field design (interdigitated and straight channel) to the operations of PEM fuel cells using a steady-state, isothermal, three-dimensional model. However, no validations of simulation results were presented in the paper. In addition, the simulation studies were performed for a higher value of GDL porosity (0.8) which is far above the porosity value used in most of existing models.

Rismanchi et al. (2008) developed a steady-state, three-dimensional, single-phase PEMFC model to predict the fuel cell behaviour for different operating conditions. The authors found that diffusion parameters of GDL and CL highly influence the overall reactant transport. In addition, the simulation results depend on the value of charge transfer coefficient and small decrease of charge transfer coefficient results in significant reduction of cell voltage at any current density. However, the model is not capable of predicting cell performance for intermediate and higher current densities (higher than 0.2 Acm^{-2}) due to not considering the liquid water effect.

Peng and Lee (2006) developed a single-phase non-isothermal model for PEM fuel cell at high operating temperature and identified width of gas channel and land area as key optimization parameters for cell performance improvement. Lum and McGuirk (2005) formulated a steady state, isothermal, three-dimensional, single-phase complete PEM fuel cell model. The model was validated both globally and locally using experimental data (Potter 1999, Shimpalee et al. 1999). A deviation in the simulated results from experimental results was observed at high current densities and high humidity condition. Limiting permeability for the model was identified and performance deterioration of the cell was monitored. Dawes et al. (2009) improved a single-phase PEM fuel cell model similar to model developed by Lum and McGuirk (2005), Dutta, Shimpalee and Van Zee (2001) and Springer et al. (1991). The effect of water flooding and variation of effective diffusivity models were investigated. The model was validated against the work of Shimpalee et al. (1999). The author suggested that a multi-phase model is essential to investigate liquid water saturation in porous regions.

You and Liu (2002) found the limitations of single-phase models and suggested to use a two-phase model for more realistic simulation

results. Liu et al. (2006) developed a three-dimensional, steady state, isothermal, multicomponent transport model to investigate the mass transfer limitations at different current densities. The authors used a constant value of membrane phase conductivity and net water transfer rate. Al-Baghdadi and Al-Janabi (2007a) performed detailed numerical analyses of PEM fuel cell performance at various conditions using constant value of membrane proton conductivity. However, membrane proton conductivity and net water transfer depend upon water concentration, temperature, current densities and inlet humidity conditions and influence the overall cell voltage prediction.

Meng (2006, 2007a) presented a mixed-domain method for consistent water transport treatment in membrane electrode assembly. Limitations of single-domain method for water transport through membrane were identified. The new mixed domain approach shows better accuracy than the single-domain method. Recently, Dokkar et al. (2011) examined species transport phenomena using a single-phase, non-isothermal, three-dimensional PEM fuel cell model. Good Agreement with experimental results (Wang et al. 2003) is observed at intermediate current densities. The authors also investigated the cell behaviour at varying operating pressure. The authors recommend the single-phase model as a first approximation to investigate transport phenomena inside fuel cell and obtain cell performance at different conditions. However, the simulations were performed for low membrane thickness value of 0.108 mm and porosity values of the GDL and CL were not mentioned in the paper. Inamuddin et al. (2011) investigated the effect of porosity and thickness of a GDL on PEMFC performance using a three-dimensional model. Higher cell performance was observed for higher porosity of GDL. In addition, optimization study shows that an increase in GDL thickness results higher reactant concentration at cathode side. However, no validation of the model

results with experimental results was presented in the paper to justify their investigation.

Hashemi, Rowshanzamir and Rezakazemi (2012) compared the performance between straight and serpentine PEM fuel cells using a three-dimensional, single-phase model. The authors investigated reactants mass fractions distribution, current density and temperature distribution along the channel at various locations. The simulation studies were performed for a constant value of membrane proton conductivity which is adding uncertainty in analysis.

2.2 Multi-phase modelling of PEM fuel cells

Karimi, Jafarpoura and Li (2009) investigated the water management issue and identified some key factors (humidification, flow inlet temperature and flow pressure) affecting the cell performance. Liquid water injection at the anode channel inlet shows improvement in the cell performance but proper humidification remains as a crucial factor to maximize the performance (Matamoros and Bruggemann 2006, Zhou et al. 2006, Karnik , Stefanopoulou and Sun 2007, Chen et al. 2004, Zong, Zhou and Sobiesiak 2006,).

Ahmed and Sung (2007) investigated water management using a three-dimensional model. They found that water activity on anode side determines the membrane conductivity and hence, affect local current density distribution. The author observed that water mostly accumulates under the land area in the cathode side at higher current density. They suggest having a higher cathode side stoichiometric flow ratio to improve the cell performance. However, the model results were not supported by any experimental results.

Meng et al. (2007b) developed a two-phase non-isothermal two dimensional model to investigate water transport in membrane electrode assembly. The model shows potential regions of water accumulation and dry region. However, model verification data at low humidity condition was not presented in the paper. Ahmed et al. (2008) proposed that higher anode humidity condition results in better cell performance at higher current densities. However, the model was validated against the results from modelling work of Dutta, Shimpalee and Van Zee (2000), which shows cell performance at a very high current density of 2.4 Acm^{-2}. This cell performance at this high current density value is contradicting most of published experimental work.

Yuan et al. (2004) developed a three-dimensional, two-phase, PEMFC cathode duct model. The authors solved the governing equations (continuity, momentum, energy and species transport) and liquid water effect due to phase change was added to the solver. Liquid water saturation was used to describe the liquid water volume fraction at the cathode duct. The author found that the current density distribution depends on saturation levels and inlet humidity conditions of reactants. However, the simulation was carried out for a constant activation potential value of 0.3V. This added uncertainty to the simulation results.

Hu et al. (2004) developed a two-phase flow model and compared the performance against the single-phase (Um, Wang, and Chen 2000) and experimental results (Ticianelli, Derouin, and Srinivasan 1988). The authors developed a multiple phase mixture model to investigate cell performance. Liquid water saturation effect was added in the diffusion of reactants. It was observed that single-phase flow model over predict cell voltage at higher current density. The author also examined the effect of flow field design on fuel cell performance and

found that conventional flow field provide better performance for non-humidified cathode inlet air.

Meng and Wang (2005) developed a three-dimensional, multi-phase mixture model to investigate flooding dynamics in PEM fuel cells. The authors compared the simulation results with single phase results. In addition, liquid water effect at higher current density was predicted using two-phase model. According to their observation, a single-phase model over predicting current density distribution under land area where most of the water vapour accumulates. A two-phase model is capable of predicting the cell performance accurately by considering phase change effect under the land area.

Hu and Fan (2006) investigate transport phenomena and electrochemical kinetics in PEM fuel cell using three-dimensional, steady-state model. According to their research, it was observed that gas humidification temperature of cathode, inlet velocity of cathode gas and shoulder-to-channel ratios have significant influence on cell performance. The authors suggest that low humidity inlet conditions for low current density and high humidity inlet conditions for high current density operation are favourable to achieve better performance.

Schwarz and Djilali (2007) used FLUENT PEM fuel cell module to investigate water management issues inside cells. The authors improved the existing multi-phase transport model by incorporating thin film agglomerate catalyst layer model. The authors identified possible dehydration inside anode side of the PEM fuel cell. Higher value of liquid saturation shows significant reduction in cell voltage. Catalyst layer composition and structure were identified as crucial design parameters for PEM fuel cell. Al-Baghdadi and Al-Janabi (2007b) developed a comprehensive three-dimensional, multi-phase CFD model of a PEM fuel cell to improve the fundamental understanding of

transport phenomena. The model includes phase change and saturation to predict liquid water in the gas diffusion layer. An optimization study was performed based on operating, design and material parameters. Berning (2008) investigated multi-phase flow through porous media using multi-fluid PEM fuel cell model. The author found that flooding occurs under the land area. Yu et al. (2009) investigated cell performance and transport phenomena using a three-dimensional, gas-liquid two-phase flow, isothermal PEM fuel cell model. Phase change and water transport mechanisms are added to the model. However, the effect of saturation is not included to the overall species diffusion equation.

Yuan et al. (2010) developed three-dimensional, multiphase fuel cell model to predict cell performance at different operating parameters using polarization curves (I-V and I-P curves). Saturation model was used to investigate liquid water transport in FLUENT. The authors conducted experimental and validated the model predicted results. A small deviation in cell voltage prediction over the entire current density range was observed. The authors found that anode humidification is more important factor than cathode side humidification as it affects the electro-osmotic drag mechanisms. Low cathode humidity with high anode humidity was recommended by authors.

More recently, Obut and Alper (2011) developed a three-dimensional, non-isothermal, half channel two-phase CFD model of PEM fuel cell to investigate the dependence of performance on cathode catalyst layer parameters. The effect of liquid water is added in the reactant diffusion through porous regions. The authors recommended an optimum design of catalyst layer based on simulation results. Jung, Lee and Chen (2012) used a multi-phase cathode side computational domain to reduce the computation time. They ignored the anode side electro-chemistry and over-potential and made simplified assumptions for

overall domain. The author examined three different geometries and validated against experimental results (Ticianelli, Derouin, and Srinivasan 1988). Predicted cell performance suggests that their modelling approach can be a solution to reduce the large computation time and provide better understanding for researchers to design optimized fuel cells.

A steady-state, non-isothermal, three-dimensional PEM fuel cell transport model was developed by Liu, Lou and Wen (2010). They performed the study with a dry cathode and saturated anode conditions and considered two-phase transport of water. They found that water content in membrane depends on current density. Very low velocity of liquid water was observed through porous regions. The net water transfer values changes from 0.5 to 0.1 for low to high current densities.

Min (2010) developed a three-dimensional, two-phase PEM fuel cell model to investigate cell performance at different humidity conditions. The author considers phase change effect (condensation and evaporation) of water in the model. At higher current densities significant difference, between the predicted cell performance and experimental results of Ticianelli, Derouin, and Srinivasan, 1988, are observed. According to the author, lower humidity at cathode inlet significantly improves cell performance which actually contradicts previous published results. More recently, Khan, Sundén, and Yuan (2011) reviewed the existing two-phase modelling approaches in PEM fuel cell modelling and identified modelling discrepancies. The authors found that the equations and assumptions used to define the saturation effect in porous media and phase change between water vapour to water liquid add uncertainty in analysis.

2.3 Modelling Uncertainty for flow through gas diffusion layer

Gas diffusion layer is one of the key components of a PEM fuel cell design. The main purpose of a gas diffusion layer (GDL) is to transport fresh reactants from the flow channel to the catalyst layer where reactions occur. In addition, GDL removes the produced water and carries electron to facilitate reactions. The effective transport coefficients of species through GDL inside PEM fuel cells have traditionally been modelled using Bruggeman model. Such as, some of the initial three-dimensional PEM fuel cell models implemented effective diffusivity model based on Bruggeman model (Dutta, Shimpalee and Van Zee 2001, Um and Wang 2004, Nguyen, Berning, and Djilali 2004, Lum and McGuirk 2005, Siversten and Djilali 2005).

Pharoah, Karan and Sun (2006) cited a comprehensive review of 100 papers in modelling of proton exchange membrane and direct methanol fuel cells and stated that majority of the published modelling works considered species transport on gas diffusion layer using Bruggeman correlations that were initially developed for granular porous media (beds od spherical particles of different sizes). The microstructure of gas diffusion layer is made of randomly distributed carbon fibres of 7-10 μm diameters and several millimetres long formed into paper or cloth. This microstructure of GDL differs from the granular porous media and include anisotropic behaviour in the transport of reactants though GDL (Pharoah, Karan and Sun 2006). Nam and Kaviany (2003) developed an effective gas diffusivity model for GDL based on pore network modelling of fibrous web. The model was compared against percolation based model of Tomadakis and Sotirchos (1993) and a multi-length scale, particle based porous media model of Mezedur, Kaviany and Moore (2002). It was observed from the study that Tomadakis and Sotirchos (1993) model better represented the anisotropic behaviour of GDL. Gostick et al. (2006)

experimentally studied in-plane and through-plane permeability of several commercially available GDLs and showed that the in-plane permeability was much higher than the through-plane permeability. The authors showed that Tomadakis and Sotirchos (1993) percolation based model could represent the anisotropic permeability of all the commercial GDLs studied and capable of accounting for anisotropy in diffusivity by modelling tortuosity more accurately.

Above literature review suggests that Bruggeman correlation does not appear to represent diffusivity of species through a GDL. However, it would be interesting to investigate the effects of various effective diffusivity models on fuel cell performance prediction. The study would provide information about the uncertainty in modelling effective diffusivity contributes to the actual modelling uncertainty of a PEM fuel cell.

Pharoah, Karan and Sun (2006) treated the anisotropic gas transport in GDL by percolation based anisotropic model of Tomadakis and Sotirchos (1993) and showed that anisotropic treatment had significant effects on the prediction of fuel cell potential at current densities between 0.8 - 1.2 Acm^{-2}. At lower current densities, though effects of anisotropy on voltage appeared to be small, there were significant differences in the distribution of local current densities especially under the land area. Dawes et al. (2009) developed a percolation based isotropic diffusivity model and performed a parametric study of effective diffusivity by arbitrarily changing the diffusivity values. The author showed that gradual reduction of the diffusivity coefficients reduced the predicted average current density and brought it closer to the experimental data. The suggested percolation based isotropic diffusivity model also provided slightly better results compared to the Bruggeman model. A systematic comparison of various diffusivity

models in predicting the performance of a PEM fuel cell has been presented in chapter 5.

Therefore, one of the objectives set in this thesis is to develop a three-dimensional, steady state, PEM fuel cell models to predict fuel cell voltage more accurately at higher current density. A single-phase PEM fuel cell model is essential to provide first approximation of reactants transport through porous regions (gas diffusion layers and catalyst layers), transport limitations at different operating conditions and opportunity to develop further to a multi-phase model by considering modelling uncertainty for flow though GDL and water vapour to liquid phase change effect.

3

Chapter 3: Methodology

The diversity and complexity of electrochemical reactions and transport phenomena occurring at disparate length and scale requires a systematic framework and computational fluid dynamics code to solve the comprehensive mathematical model. The computational fuel cell dynamics involve the following steps:

i. Physicochemical model development;
ii. Advanced numerical algorithms to solve the model;
iii. Material characterization and appropriate boundary conditions, and
iv. Finally the model validation.

The focus of this research is to develop a complete three-dimensional steady state PEM fuel cell model based on electrochemistry, species transport considerations, and an appropriate computational fluid dynamics (CFD) code has been applied to solve the model.

In this chapter, the governing equations and auxiliary equations for modelling PEM fuel cells are explained. The numerical procedures for solving the equations are presented. Source terms, effective diffusion of species in porous layers and electrochemical reactions at catalyst layers are written in C++ user defined functions (UDF) which are interpreted by the CFD solver (ANSYS Fluent 12.0). A brief description of the UDF code is also presented. Finally modelling parameters are provided with appropriate boundary conditions.

3.1 Modelling of PEM fuel cells

Computational fluid dynamics (CFD) modelling of PEM fuel cell is useful tool to design and develop efficient fuel cells. These models present the following information related to operation a PEM fuel cell (Ziegler 2005):

- Mass transport process through the porous regions of the cell, which is very important to identify the transport limitations.

- Validation of modelling results with experimental results to improve the model and assumptions.

- Investigation of time dependence phenomena of the cell such as the liquid water movement.

- Fuel cell variables and parameters, such as reactants concentration and current density distribution at the catalyst layer/ membrane interface; those are difficult to get using experiments.

- Design constraints of fuel cell components such as the flow channel, gas diffusion layer by parametric studies.

- Finally control strategies for improved cell performance.

3.2 Model development

A schematic diagram of a three-dimensional PEM fuel cell stack is shown in Figure. 3.1. A single cell is considered as a computational domain. The numerical model consists of anode and cathode sides (gas channel, gas diffusion layer (GDL) and catalyst layer (CL) on both sides). The gas channel is transporting the reactants (oxygen and hydrogen) and the product (water) mixed in air to and from the porous gas diffusion layers. The GDL transports the fresh reactants to the CL where the electrochemical reactions occur. The polymer electrolyte membrane is sandwiched between the catalyst layers. Protons and water are transported through the membrane.

3.3 Modelling Assumptions

The three-dimensional model is solved based on the following assumptions:

i. the fuel cell operates under steady state conditions;

ii. fuel cell operates under isothermal conditions;

iii. gas mixtures are assumed as the ideal gas;

iv. laminar flow in the flow channels (Reynolds number < 100);

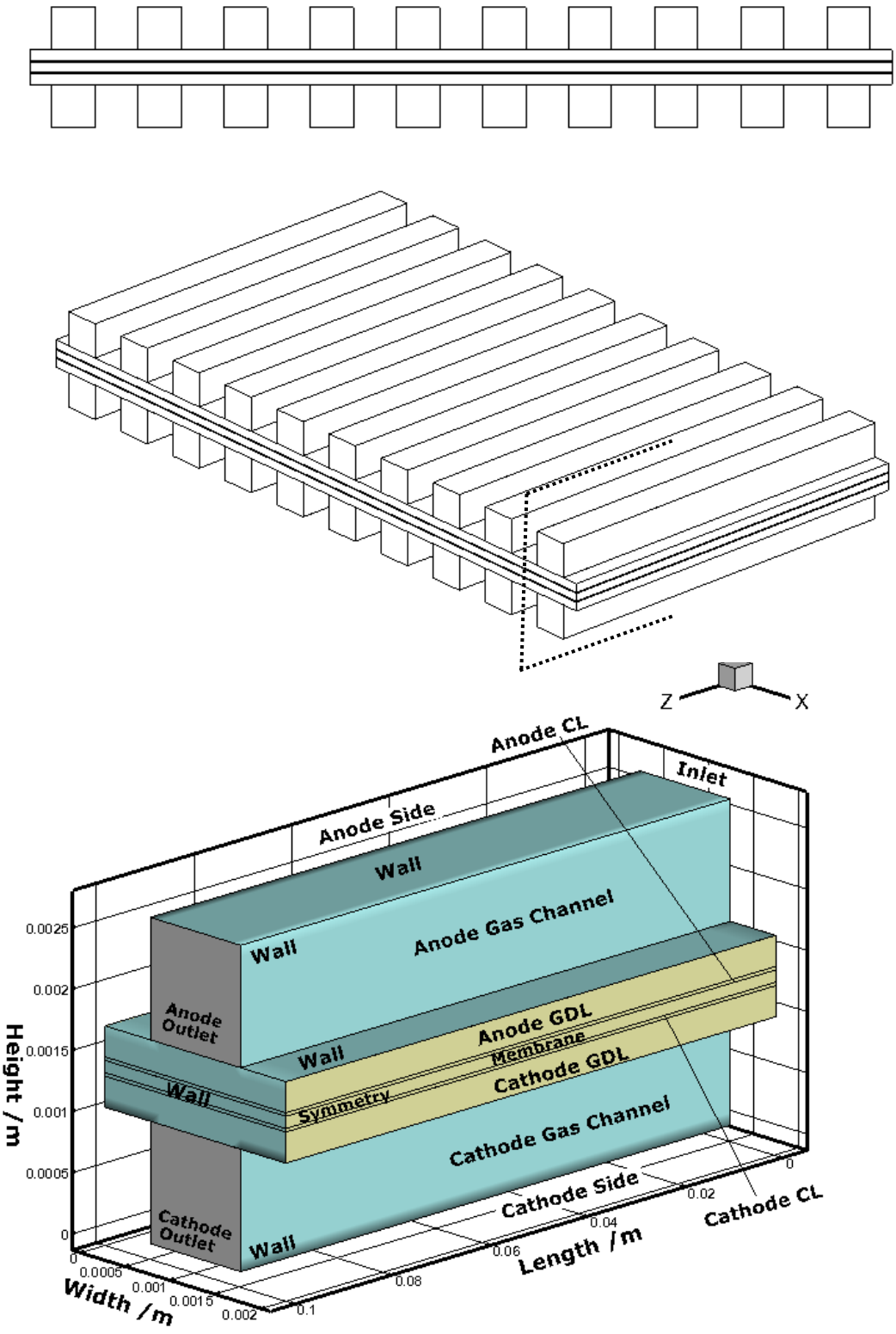

Figure 3.1 Schematic diagram of a three-dimensional PEM fuel cell model.

v. the membrane is considered impervious to reactant gases,

vi. water produced on the cathode side is in vapour phase in the single phase model, and

vii. At the catalyst layer and membrane interface, zero velocity gradient ($\triangledown u$= 0) and zero species gradient ($\triangledown X_k$ = 0) boundary conditions are applied.

3.4 Governing Equations

The governing equations for the steady-state PEM fuel cell model consist of continuity, conservation of momentum and species transport equation. To represent the electrochemistry and transport phenomena through membrane, appropriate source terms are applied at the anode and cathode catalyst layers. As isothermal model is assumed, energy equation is not considered in the present steady state model.

The mass conservation equation (continuity equation):

$$\nabla.(\rho\vec{u}) = S_m \tag{3.1}$$

where ρ is the fluid density and $\vec{u}$ is the velocity vector and S_m is the source term.

The momentum conservation equation:

$$\nabla.(\rho\vec{u}\vec{u}) = -\nabla P + \nabla.(\mu\nabla.\vec{u}) + S_u \tag{3.2}$$

where *P* is the pressure and S_u is the source term.

In porous region, Darcy's law term is added to the momentum equations to represent the momentum related with the surface forces. The source term is expressed as:

$$S_u = -\frac{\mu \vec{u}}{K} \tag{3.3}$$

The species conservation equation:

$$\nabla.\left(\rho \vec{u} \vec{X}_k\right) = \nabla.\left(D_k^{eff} \rho \nabla \vec{X}_k\right) + S_k \tag{3.4}$$

where index *k* refers to different species, X_k is the mass fraction of species *k* and D_k^{eff} is the effective diffusion coefficient of species *k*. The species conservation equations for hydrogen and water vapour are solved in anode side:

$$\nabla.\left(\rho \vec{u} \vec{X}_{H_2}\right) = \nabla.\left(D_{H_2}^{eff} \rho \nabla \vec{X}_{H_2}\right) + S_{H_2} \tag{3.4a}$$

$$\nabla.\left(\rho \vec{u} \vec{X}_{wv_a}\right) = \nabla.\left(D_{wv_a}^{eff} \rho \nabla \vec{X}_{wv_a}\right) + S_{aw} \tag{3.4b}$$

The species conservation equations for oxygen and water vapour are solved in cathode side:

$$\nabla.\left(\rho \vec{u} \vec{X}_{O_2}\right) = \nabla.\left(D_{O_2}^{eff} \rho \nabla \vec{X}_{O_2}\right) + S_{O_2} \tag{3.4c}$$

$$\nabla.\left(\rho \vec{u} \vec{X}_{wv_c}\right) = \nabla.\left(D_{wv_c}^{eff} \rho \nabla \vec{X}_{wv_c}\right) + S_{cw} \tag{3.4d}$$

The nitrogen mass fraction mass fraction in the cathode side is calculated using the following equation:

$$X_{N_2} = 1 - X_{O_2} - X_{wv_c} \tag{3.5}$$

The diffusion coefficient in gas channel is expressed as (Ju, Meng and Wang 2005):

$$D_k = D_{k,ref}\left(\frac{T}{T_{ref}}\right)^{3/2}\left(\frac{P_{ref}}{P}\right) \quad (3.6)$$

where $D_{k,ref}$ is the reference value at T_{ref} and P_{ref}.

The effective diffusivity of the species in the porous zones is described by the Bruggeman correction (Min 2009):

$$D_k^{eff} = \epsilon^{1.5} D_k \quad (3.7)$$

The source terms (S_k) in the species conservation equation are defined as zero for all regions of the model except the catalyst layers. Species source term for anode and cathode catalyst layers are expressed as (Min 2009):

- Consumption of hydrogen due to electrochemical effects at the anode catalyst layer

$$S_{H_2} = -\frac{IA}{2F} M_{H_2} \quad (3.8)$$

- Consumption of oxygen due to electrochemical effects at the cathode catalyst layer

$$S_{O_2} = -\frac{IA}{4F} M_{O_2} \quad (3.9)$$

- Production of water and flux of water due to electrochemical effects at the cathode catalyst layer

$$S_{cw} = \frac{[1+2\alpha]IA}{2F} M_{H_2O} \quad (3.10)$$

- Flux of water due to electrochemical effects at the anode catalyst layer

$$S_{aw} = -\frac{\alpha IA}{F} M_{H_2O} \tag{3.11}$$

The average current density I and net water transfer coefficient α are used to determine these source terms. A number of auxiliary equations need to be solved to model the electrochemical reactions and determine the cell voltage and net water transfer coefficient. The empirical equations are based on the assumption of Nafion 117, and taken from the work of Springer et al. (1991). The source terms used in the single-phase model are summarized in the following Table 3.1.

Table 3.1 Source Terms for single phase model.

PEM fuel cell Zones	S_m	S_u	S_k
Gas channels	0	0	0
Gas diffusion layers	0	$S_u = -\frac{\mu \vec{u}}{K}$	0
Catalyst layers	0	$S_u = -\frac{\mu \vec{u}}{K}$	Cathode Side: $S_{O_2} = -\frac{IA}{4F} M_{O_2}$ $S_{cw} = \frac{[1+2\alpha]IA}{2F} M_{H_2O}$ Anode side $S_{H_2} = -\frac{IA}{2F} M_{H_2}$ $S_{aw} = -\frac{\alpha IA}{F} M_{H_2O}$
Membrane	0	0	0

For the multiphase model, the source term for water liquid phase change is added in both anode and cathode side. (Yu et al. 2009)

$$S_{wlp} = -S_{wvp} = \frac{(P_{wv} - P_{wv}^{sat})}{RT} \times M_{H_2O} \times k_c \quad (3.12)$$

Where k_c is the condensation rate and P_{wv} is partial pressure of water vapour. Phase change of water depends on partial pressure of water vapour and saturation water vapour pressure at a specific temperature. Condensation occurs when water vapour partial pressure is higher than water vapour saturation pressure, whereas evaporation takes place for opposite situation. (Ahmed and Sung 2006)

The species conservation equations for hydrogen, water vapour and water liquid are solved in anode side for the multiphase model:

$$\nabla.\left(\rho\vec{u}\vec{X}_{H_2}\right) = \nabla.\left(D_{H_2}^{eff}\rho\nabla\vec{X}_{H_2}\right) + S_{H_2} \quad (3.13a)$$

$$\nabla.\left(\rho\vec{u}\vec{X}_{wv_a}\right) = \nabla.\left(D_{wv_a}^{eff}\rho\nabla\vec{X}_{wv_a}\right) + S_{aw} \quad (3.13b)$$

$$\nabla.\left(\rho\vec{u}\vec{X}_{lq_a}\right) = \nabla.\left(D_{lq}\rho\nabla\vec{X}_{wv_a}\right) + S_{wlp} \quad (3.13c)$$

The species conservation equations for oxygen, water vapour and water liquid are solved in cathode side:

$$\nabla.\left(\rho\vec{u}\vec{X}_{O_2}\right) = \nabla.\left(D_{O_2}^{eff}\rho\nabla\vec{X}_{O_2}\right) + S_{O_2} \quad (3.13d)$$

$$\nabla.\left(\rho\vec{u}\vec{X}_{wv_c}\right) = \nabla.\left(D_{wv_c}^{eff}\rho\nabla\vec{X}_{wv_c}\right) + S_{cw} \quad (3.13e)$$

$$\nabla.\left(\rho\vec{u}\vec{X}_{lq_c}\right) = \nabla.\left(D_{lq}\rho\nabla\vec{X}_{wv_c}\right) + S_{wlp} \quad (3.13f)$$

The nitrogen mass fraction mass fraction in the cathode side is calculated using the following equation:

$$X_{N_2} = 1 - X_{O_2} - X_{wv_c} - X_{lq} \tag{3.14}$$

The diffusion coefficient in porous regions is expressed as

$$D_k^{eff} = D_k f(\epsilon) g(s) \left(\frac{T}{T_{ref}}\right)^{3/2} \left(\frac{P_{ref}}{P}\right) \tag{3.15}$$

Tomadakis and Sotirchos (1993) suggested the following percolation theory based diffusion model for random fibrous porous medium

$$f(\varepsilon) = \varepsilon \left(\frac{\varepsilon - \varepsilon_p}{1 - \varepsilon_p}\right)^{\alpha} \tag{3.16}$$

where ε_p is the percolation threshold and equal to 0.11. α is the empirical constant depends on the direction. The value of α is 0.521 for in-plane and 0.785 for cross-plane diffusion. More description about diffusion models are provided in chapter 5.

Saturation function is defined as,

$$g(s) = (1 - s)^m \tag{3.17}$$

Where *s* is the liquid water saturation and *m* is power law model constant. More description about the constant is provided in chapter 6.

Table 3.2 shows the summary of source terms used in two phase model.

Table 3.2 Source Terms for two phase model.

PEM fuel cell Zones	S_m	S_u	S_k
Gas channels	0	0	liquid water phase change: $S_{wlp} = -S_{wvp}$
Gas diffusion layers	0	$S_u = -\frac{\mu\vec{u}}{K.K_{rg}}$ $K_{rg} = (1-s)^3$	liquid water phase change: $S_{wlp} = -S_{wvp}$
Catalyst layers	0	$S_u = -\frac{\mu\vec{u}}{K.K_{rg}}$ $K_{rg} = (1-s)^3$	liquid water phase change: $S_{wlp} = -S_{wvp}$ Cathode Side: $S_{O_2} + S_{cw} + S_{wvp}$ Anode side $S_{H_2} + S_{aw} + S_{wvp}$
Membrane	0	0	0

3.5 Auxiliary Equations

The auxiliary model equations, need to be solved to determine the net water transfer coefficient and cell voltage at an average current density, are summarized in next section:

Net water transfer coefficient (Lum and McGuirk 2005) describes the transport of water across the membrane by considering electro-osmotic drag and back diffusion.

$$\alpha = n_d - \frac{FD_{H_2O}(C_{H_2O_c} - C_{H_2O_a})}{It_m} \tag{3.18}$$

Where D_{H_2O} represents the water diffusion coefficient, and $C_{H_2O_a}$ and $C_{H_2O_c}$ represent the molar concentration of water at the anode and cathode side respectively, I is the average current density and t_m is the membrane thickness and *F* is the Faraday's constant.

Electro-osmotic drag coefficient describes the amount of water dragged by each proton across the membrane from anode to cathode side and expressed as, (Lum and McGuirk 2005)

$$n_d = 0.0049 + 2.02a_a - 4.53a_a^2 + 4.09a_a^3 \; ; \; a_a \leq 1$$

$$n_d = 1.59 + 0.159(a_a - 1); \qquad a_a > 1 \tag{3.19}$$

Electro-osmotic drag is a function of water activity of anode side, a and is defined as, (Lum and McGuirk 2005)

$$a_k = \frac{X_{H_2O,K}\, P}{P^{sat}_{H_2O,K}} \tag{3.20}$$

where P is the cell pressure and $X_{H_2O.K}$ is the mole fraction of water on either the anode or cathode side.

Water diffusion coefficient is expressed as a function of electro-osmotic drag coefficient and the cell temperature and defined as

$$D_{H_2O} = 5.5e^{-11} n_d \exp[2416(\frac{1}{303} - \frac{1}{T})] \quad (3.21)$$

Water vapour saturation pressure (Lum and McGuirk 2005) depends on the cell temperature

$$P^{sat}_{H_2O,K} = [0.000644367 + 0.000213948(T - 273.0) + 3.4329e^{-5}(T - 273.0)^2 - 2.70381e^{-7}(T - 273.0)^3 + 8.77696e^{-9}(T - 273.0)^4 - 3.14035e^{-13}(T - 273.0)^5 + 3.82148e^{-14}(T - 273.0)^6]1.013e^5 \quad (3.22)$$

Water concentration on the anode and cathode side depends on water activity, (Lum and McGuirk 2005)

$$C_{H_2OK} = \frac{\rho_{m,dry}}{M_{m,dry}}(0.043 + 17.8a_k - 39.8{a_k}^2 + 36.0{a_k}^3; a_k \le 1$$

$$C_{H_2OK} = \frac{\rho_{m,dry}}{M_{m,dry}}(14 + 1.4(a_k - 1)); a_k > 1 \quad (3.23)$$

Polarization Characteristics

The cell potential drops due to irreversible losses (polarization, overpotential and overvoltage losses). The cell voltage is expressed by the following equation (Min 2009):

$$V_{\text{cell}} = E - \eta_{\text{act}} - \eta_{\text{ohm}} - \eta_{\text{conc}} \quad (3.24)$$

where E is the equilibrium thermodynamic potential which is calculated using the Nernst equation (Min 2009,):

$$E = 1.23 - 0.9 \times 10^{-3}(T - 298) + 2.3\frac{RT}{4F}\log(p_{\text{h}}^2 p_{\text{o}}) \quad (3.25)$$

η_{act} is the activation overpotential, η_{ohm} is the ohmic overpotential and η_{conc} is the concentration overpotential.

- Activation overpotential (η_{act}):

The activation overpotential is a function of local current density, exchange current density and concentration of oxygen. The activation overpotential is expressed by Butler-Volmer equation, (Min 2009):

$$i_a = 2\, i_{a,ref} \left(\frac{C_h}{C_{h,ref}}\right)^{\frac{1}{2}} sinh\left(\frac{\alpha_a n_a F \eta_a}{RT}\right)$$

$$i_c = 2\, i_{c,ref} \left(\frac{C_o}{C_{o,ref}}\right) sinh\left(\frac{\alpha_c n_c F \eta_c}{RT}\right) \quad (3.26)$$

Where $i_{a,ref}$ and $i_{c,ref}$ are the exchange current density multiply specific area, n is electron number of reaction at anode or cathode and α is the transfer coefficient. (Min 2009)

- Ohmic Overpotential (η_{ohm}):

The ohmic overpotential occurs due to resistance to electron and ion transfer and is expressed as (Min 2009):

$$\eta_{\text{ohm}} = \eta_{\text{ohm}}^{\text{el}} + \eta_{\text{ohm}}^{\text{pro}} = I(R^{\text{el}} + R^{\text{pro}}) \quad (3.27)$$

Where R^{el} is the resistance to electron transfer and R^{pro} is the resistance to proton transfer. In the present model, R^{el} = 0.1 Ω cm^2 is used (Min 2009). R^{pro} is calculated using following expression:

$$R^{pro} = \frac{t_m}{k_m} \quad (3.28)$$

t_m is the height of the membrane and k_m is the phase conductivity of the membrane. The membrane phase conductivity depends on temperature and water concentration at anode side and expressed as

$$k_m = 100(0.00514\left(\frac{M_{m,dry}}{\rho_{m,dry}}\right)C_{H_2O_a} - 0.00326) \times \exp\left[1268(\frac{1}{303} - \frac{1}{T})\right] \quad (3.29)$$

- Concentration Overpotential (η_{conc}):

At high current densities, polarization losses are dominated by concentration overpotential which is caused by slow diffusion of gas phase through the porous regions. These losses is determined by

$$\eta_{\text{conc}} = -\frac{RT}{nF}\ln\left(1 - \frac{I}{I_L}\right) \quad (3.30)$$

where I_L is the limiting current density (Min 2009):

$$i_L = \frac{nFD_hC_{k,0}}{H_d} \quad (3.31)$$

3.6 Boundary Conditions

Dirichlet boundary conditions are applied at cathode and anode inlet. The inlet velocity is a function of stoichiometric flow ratio, ζ, geometrical area of membrane A_m and cross-section area of gas channel, A_{ch}, reference current density, I_{ref} and concentration of reactants. (Min 2009)

$$u_{c,in} = \zeta \frac{I_{ref}}{4F}\frac{1}{x_{O2,in}}\frac{RT}{P}\frac{A_m}{A_{ch}}$$

$$u_{a,in} = \zeta \frac{I_{ref}}{2F}\frac{1}{x_{H2,in}}\frac{RT}{P}\frac{A_m}{A_{ch}} \quad (3.32)$$

A pressure outlet condition was assumed. A symmetry boundary condition is applied on the side surfaces of the porous regions (Figure.3.1). No slip condition is applied to the external walls.

3.7 Computational procedure

The computational domain has been meshed with quadrilateral grids of 12700 cells. A grid sensitivity test using up to 60000 cells has proved that the grid size is sufficient to provide grid independency. Simulations have been carried out on a quad core Xeon workstation running on serial server. Each simulation took approximately 1000 iterations to converge in approximately 15 minutes of run time for single-phase model. However, each simulation took approximately 2500 iterations to converge in approximately 1.5 hours of run time for a two-phase model.

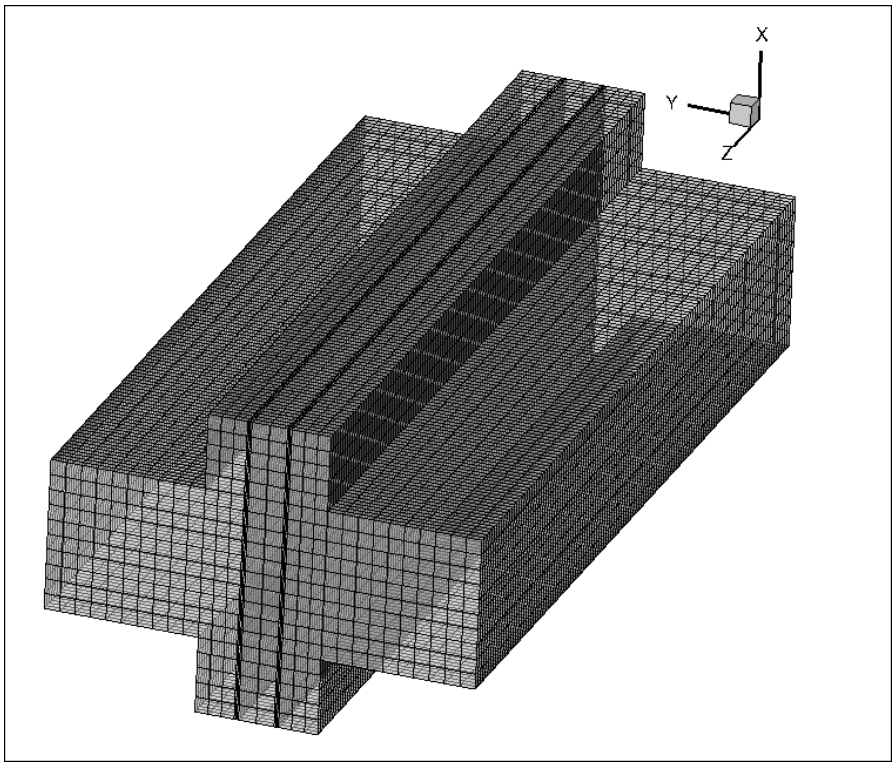

Figure 3.2 Numerical grid of the model.

GAMBIT 2.4 and ANSYS DesignModeler were used as a pre-processor and mesh creation purpose (Figure. 3.2). The governing equations and auxiliary equations have been solved to investigate the complex electrochemical processes and transport phenomena using a finite volume CFD method with convection terms being discretised with second order upwind and the diffusion terms with hybrid scheme. The SIMPLE algorithm has been selected for the pressure-velocity coupling. Appropriate source terms have been applied to the governing equations for the catalyst layers using user defined functions. Source terms, species diffusion through porous layers and electrochemical reactions at catalyst layers were written in C++ UDFs which has been interpreted by the CFD solver FLUENT. An explicit electro-chemistry model has been used where an average current density has been specified and all other electro-chemical parameters have been calculated based on the iterative solution of governing mass fraction of species. The relative error is considered less than 10^{-6} for convergence. Postprocessing is done using Tecplot 360 2010 and Microsoft Excel 2007. A brief description of UDF code is provided in the following section and single-phase UDF code is presented in Appendix section. The solving process flow diagram is shown in Figure. 3.3.

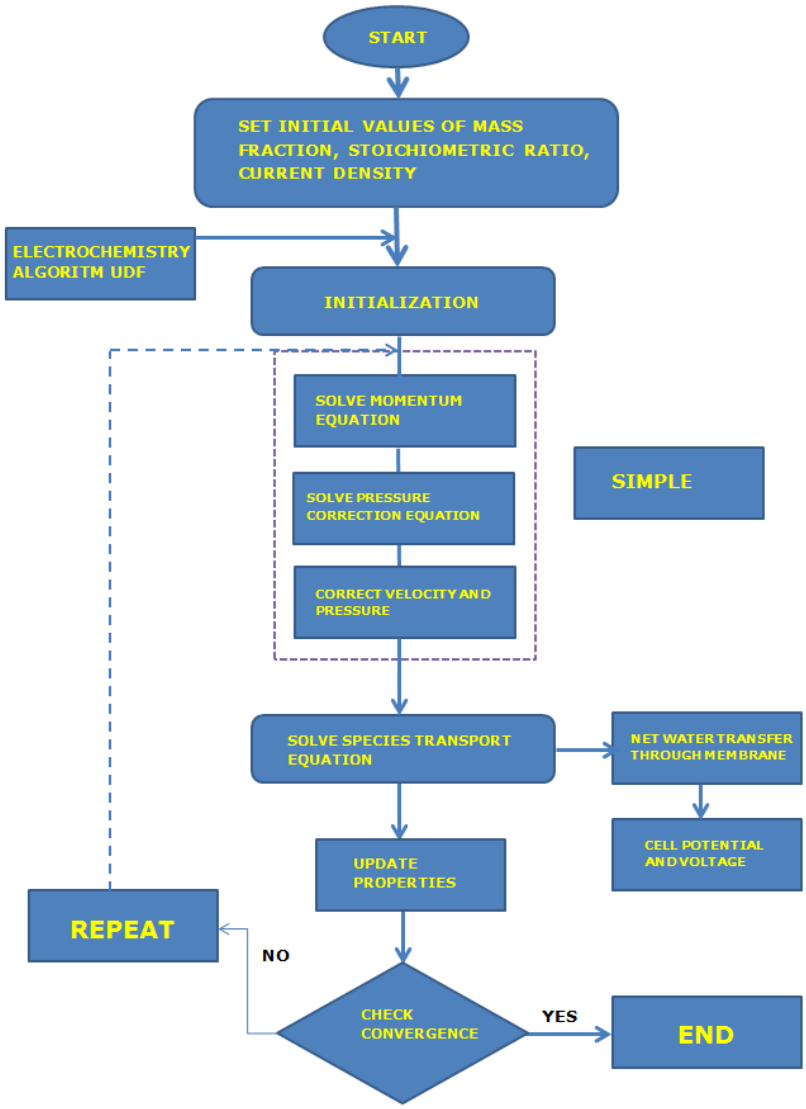

Figure 3.3 Numerical process flow diagram.

3.7.1 User defined functions

Anode and cathode side velocity is calculated using DEFINE_PROFILE macro. Stoichiometric flow ratio, mole fraction of reactants, operating pressure, and other parameters values are given to calculate the velocity. (ANSYS FLUENT UDF 12.0 Manual 2010)

Mixture density and viscosity are calculated using DEFINE_PROPERTY macro.

Momentum source terms are calculated using DEFINE_SOURCE macro for anode and cathode GDL and CL. GDL and CL for anode and cathode are assigned using THREAD_ID(t). (ANSYS FLUENT UDF 12.0 Manual 2010)

Species diffusion are calculated using DEFINE_DIFFUSIVITY macro for isotropic and DEFINE_ANISOTROPIC_DIFFUSIVITY macros for anisotropic diffusion through porous zones. Porosity and saturation was used for calculating effective diffusion coefficients for each reactant. (ANSYS FLUENT UDF 12.0 Manual 2010)

Species transport source terms are calculated using DEFINE_SOURCE macros for anode and cathode CLs. GL and CL for anode and cathode are assigned using THREAD_ID(t). Species mass fractions are defined as user defined scalars (UDS) and solved. Liquid water phase change source terms are added in gas channels, gas diffusion layers and catalyst layers. (ANSYS FLUENT UDF 12.0 Manual 2010)

Electro-chemistry algorithms, net water transfer and cell voltage are calculated using DEFINE_ADJUST macros for both anode and cathode catalyst layers. (ANSYS FLUENT UDF 12.0 Manual 2010)

3.8 Modelling Parameters

The fuel cell geometry is similar to the computational work of Min (2010), Mazumder and Cole (2003) and Liu, Lou and Wen (2010). Physical dimensions of the computational domain as well as relevant fuel cell parameters are given in Table 3.3.

Table 3.3 Physical parameters and boundary conditions used for the simulations.

Model Parameters	Symbol and Value	Reference
Gas channel length	L= 100 mm	
Gas channel width	W = 1 mm	
Gas channel height	H_{ch} = 1 mm	
Diffusion layer height	H_d = 0.254 mm	Mazumder and Cole (2003), Min (2010), Liu, Lou and Wen (2010)
Catalyst layer height	H_{ct} = 0.0287 mm	Mazumder and Cole (2003), Min (2010), Liu, Lou and Wen (2010)
Land area width	W_l = 1 mm	
Membrane thickness	t_m = 0.23 mm	Mazumder and Cole (2003), Min (2010), Liu, Lou and Wen (2010)
Permeability	K = 1.76x 10^{-11} m^2	Mazumder and Cole (2003), Liu, Lou and Wen (2010), Min (2010)
Faraday Constant	F = 96485.309 C mol^{-1}	Min (2010)
Operating pressure at	P = 1/1 atm	Liu, Lou and

anode and cathode		Wen (2010)
Operating temperature	T = 323 K	Mazumder and Cole (2003), Liu, Lou and Wen (2010)
GDL porosity	ε_{gdl} = 0.4	Mazumder and Cole (2003), Liu, Lou and Wen (2010), Min (2010)
CL porosity	ε_{cl} = 0.4	Mazumder and Cole (2003), Liu, Lou and Wen (2010)
Dry mass of membrane	$M_{m,dry}$ = 1.1kgmol^{-1}	Dawes et al. 2009
Dry density of membrane	$\rho_{m,dry}$ = 2000 kgm^{-3}	Dawes et al. 2009
Fuel/ air stoichiometric ratio	ξ_a/ξ_c= 5/5	Min (2010)
Electron number of anode reaction	n_a = 4	Min (2010)
Electron number of cathode reaction	n_c = 2	Min (2010)
Relative humidity of inlet hydrogen	RH_a = 100%	Liu, Lou and Wen (2010), Min (2010)
Relative humidity of inlet air	RH_c = 0%	Liu, Lou and Wen (2010)
Oxygen mass fraction of inlet air	ω_O = 0.232	Liu, Lou and Wen (2010)

H_2 diffusion coefficient at 307.1 K	$D_{h,\,ref} = 0.915 \times 10^{-4}$ m^2s^{-1}	Liu, Lou and Wen (2010)
O_2 diffusion coefficient at 293.2 K	$D_{O,\,ref} = 0.22 \times 10^{-4}$ m^2s^{-1}	Liu, Lou and Wen (2010)
Water vapour diffusion coefficient at 307.1 K	$D_{w,\,ref} = 0.256 \times 10^{-4}$ m^2s^{-1}	Liu, Lou and Wen (2010)
Exchange current density at anode	$i_{a,ref} = 2.0 \times 10^8$ Am^{-3}	Liu, Lou and Wen (2010)
Exchange current density at cathode	$i_{c,ref} = 160$ Am^{-3}	Liu, Lou and Wen (2010)
Hydrogen reference concentration	$C_{h,ref} = 56.4$ mol m^{-3}	Liu, Lou and Wen (2010), Min (2010)
Oxygen reference concentration	$C_{o,ref} = 3.39$ mol m^{-3}	Liu, Lou and Wen (2010), Min (2010)
Anode transfer coefficient	$a_a = 0.5$	Min (2010)
Cathode transfer coefficient	$a_c = 0.5$	Liu, Lou and Wen (2010)
Water vapour condensation rate	$k_c = 1$ and 10 s^{-1}	Ahmed, Sung and Bae (2008)
Water liquid diffusion coefficient	$D_{lq} = = 1 \times 10^{-6}$ m^2s^{-1}	

4

Chapter 4: Single Phase Model Results

In this chapter, the predicted cell performance using the developed single-phase PEM fuel cell model is discussed. Predicted cell performance is validated with experimental results. The species mass fraction distribution for oxygen and water vapour are studied and possible dehydration areas are identified. A parametric study is performed based on operating conditions and design parameters are presented.

4.1 Grid Independence Study

In order to check the convergence of the current single-phase model, a grid independence study is performed. The numerical method needs to be consistent and stable. Truncation error occurs due to difference between discretized equation and exact solution. An unstable method is divergent in nature and that's why error increases in the numerical solution process. Therefore, the truncation error should be zero when the mesh spacing tends to zero. (Versteeg and Malasakera 2007)

Three different case studies are presented here. Mesh created with different cell sizes, Case 1: 12800 cells, case 2: 24000 cells and case 3: 60000 cells, respectively. The simulations are carried out at same conditions for all the three cases. The polarization curves obtained for the cases are shown in the Figure. 4.1. Almost identical cell voltage prediction was observed for different computation time. This indicates that case 1 is adequate to provide cell performance at different current density with minimum computation time.

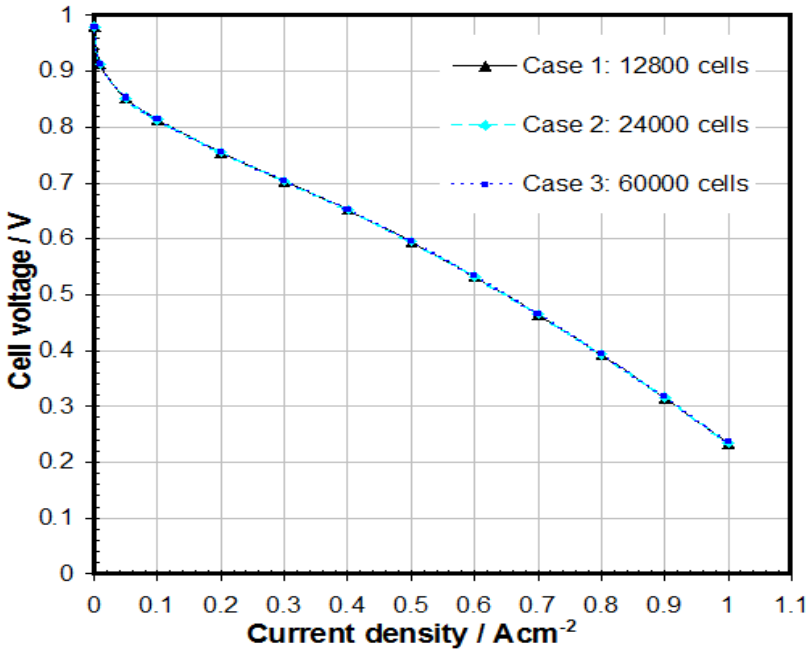

Figure 4.1 Grid independence test of present model at different mesh sizes.

4.2 Model Validation

The predicted fuel cell polarization curve of the single-phase model is shown in Figure.4.2. As the model is similar to the geometry of Mazumder and Cole (2003) and Liu, Lou and Wen (2010), the predicted cell voltage is compared with the predicted results from

these models. Mazumder and Cole (2003) and Liu, Lou and Wen (2010), compared their model predicted results with experimental results by Ticianelli, Derouin, and Srinivasan (1988) to establish the accuracy of the simulated results. A good agreement with experimental results was observed at lower current densities for the present single-phase model. While with increasing current densities, deviation from experimental results was observed for single-phase model. This variation occurs due to single-phase model cannot illuminate the liquid water effect on PEM fuel cell performance at higher current densities. This agrees with the work of Mazumder and Cole (2003) and Liu, Lou and Wen (2010).

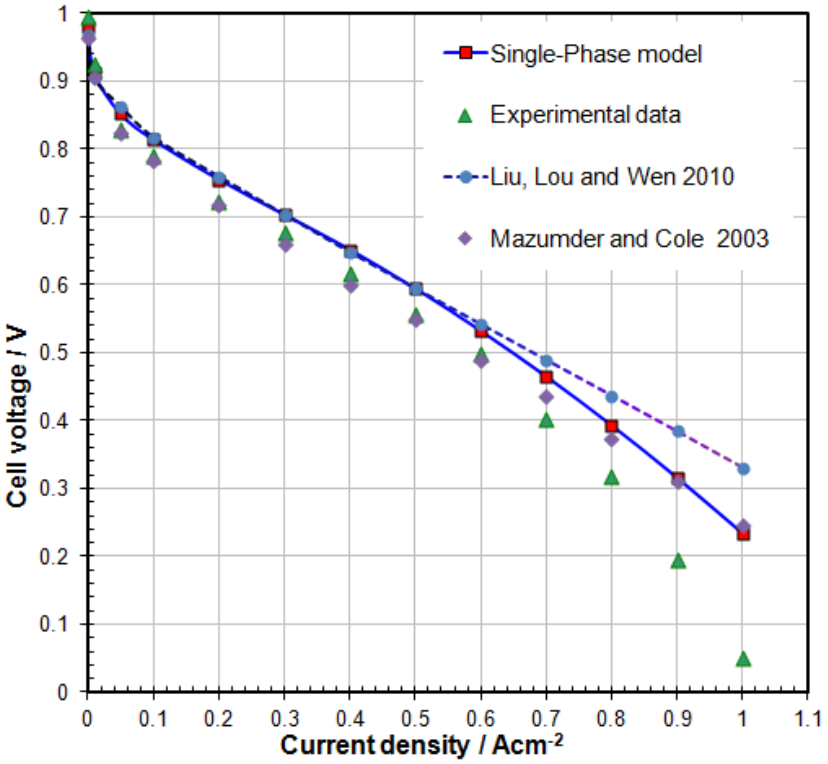

Figure 4.2 Comparison between the single-phase model results with model results of Mazumder and Cole (2003), Liu, Lou and Wen (2010) and experiments (Ticianelli, Derouin, and Srinivasan 1988).

An excellent agreement was observed at low and intermediate current densities (< 0.7 Acm^{-2}) between model results of Mazumder and Cole (2003) and experimental work of Ticianelli, Derouin, and Srinivasan (1988). The stoichiometric flow ratios for anode and cathode sides for the present model are equal to 5.0 (Min 2010), whereas Mazumder and Cole (2003) used lower values of stoichiometric flow ratios (anode 2.8 and cathode 3.0). Hence, the present model is overestimating the amount of oxygen diffusing towards the cathode catalyst layer and taking part in the reaction. That is why the model is slightly over predicting voltage at low and intermediate current densities. A systematic study of the effect of stoichiometric flow ratios on PEM fuel cell performance can lead to better prediction and excellent agreement between predicted results of present model and experimental results at higher current densities.

Liu, Lou and Wen (2010) model predicted results showed an excellent agreement with the present model results for current density value less than 0.5 Acm^{-2}. However, with increasing current density, significant difference was observed compared to present model and experimental results. Although the authors used stoichiometric flow ratios equal to 3.0, they assumed constant value of membrane phase conductivity (17 S m^{-1}) and net water transfer rate (0.2). These values depend on current density and water concentration and using a fixed value would provide inaccurate prediction of cell voltage at higher current densities. Mazumder and Cole (2003) and Liu, Lou and Wen (2010) and the present model used Bruggeman model to estimate effective diffusion of species through porous GDL. The effect of over-estimating species concentration at catalyst can be another reason for deviation of model predicted results at higher current densities. A comprehensive study based on effective diffusivity models to predict the cell performance at higher current density can identify the modelling uncertainty.

4.3 Reactant Distribution inside the Fuel Cell

The pressure distribution within the single-phase model is shown in Figure.4.3. The figure shows that the pressure decreases linearly from inlet to outlet of the PEM fuel cell (approximately 180 Pa on cathode side and 40 Pa on the anode side). The porous regions in anode and cathode sides cause the local variations in the pressure and relative mixture velocity determines the increasing or decreasing pressure across the gas diffusion layer and catalyst layer inside the PEM fuel cell. The velocity vectors along the length in the gas channels are shown in Figure.4.4. The flow takes on parabolic profile due to the assumption of wall no slip conditions and become fully developed on both the sides of the PEM fuel cell. The primary flow is pressure driven and the gauge pressure reduces to zero along both the channels. In GDL and CL, much slower velocity magnitude was observed. This suggests the transport limitations of fresh reactants through the porous regions. Transport of reactants through porous zones are one of the critical parameters as it determines the reaction rates, thus, defines the overall power output of the cell. (Dawes et al. 2009)

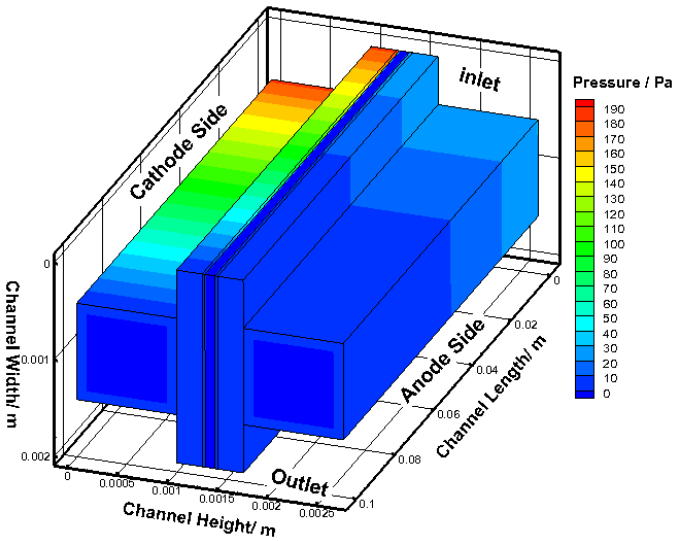

Figure 4.3 Three-dimensional pressure contours along the length of the model.

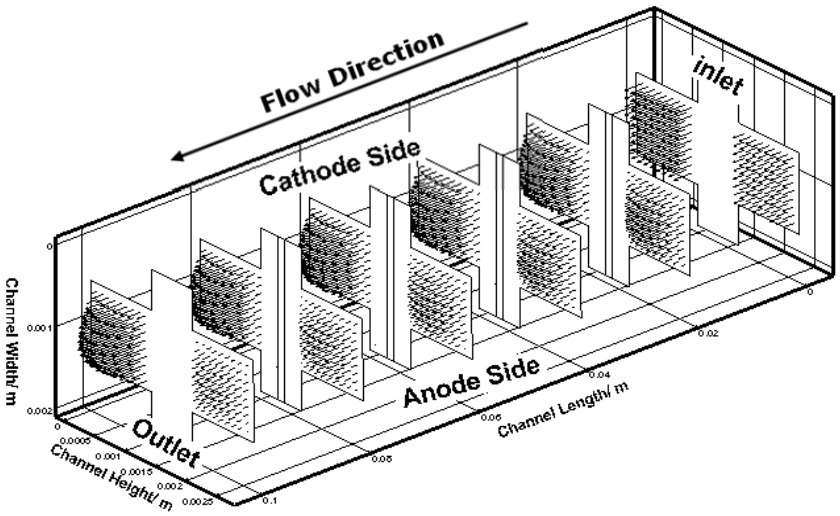

Figure 4.4 Velocity vectors along the length of the model.

It is important to study the species distribution at cathode catalyst layer where the byproduct of reaction is created. At higher current densities, excess water is produced and low rate of water removal causes flooding in the cathode side. Condensation occurs at this condition and the liquid water blocks the pores of the porous regions and limits the fresh oxygen to reach catalyst layers. Again, the overall performance of the PEM fuel cell depends on the concentration of the fresh oxygen diffusing towards cathode catalyst layer. Due to low diffusion coefficient of oxygen compared to hydrogen in anode side, cathode side operating conditions are critical parameter as it determines the limiting current density of the PEM fuel cell. Study of species distribution in that zone would provide a comprehensive understanding of transport limitations.

Figure 4.5 shows oxygen mass fraction contour plot at longitudinal slices at cathode side at low and high average current densities. Oxygen reaches the cathode catalyst layer by diffusion from gas channel through GDL and takes part in the electrochemical reaction to create water. It is observed from the curved contour plot that the

diffusion of oxygen is outward into GDL and into the land area. Oxygen concentration decreases along the gas channel and with increasing current densities (0.5 Acm^{-2} and 1 Acm^{-2}). The reason for this is that the consumption of oxygen increases with increasing current densities. The mass fraction of water vapour produced as a by-product of electrochemical reactions increases along the channel and tends to replace the oxygen.

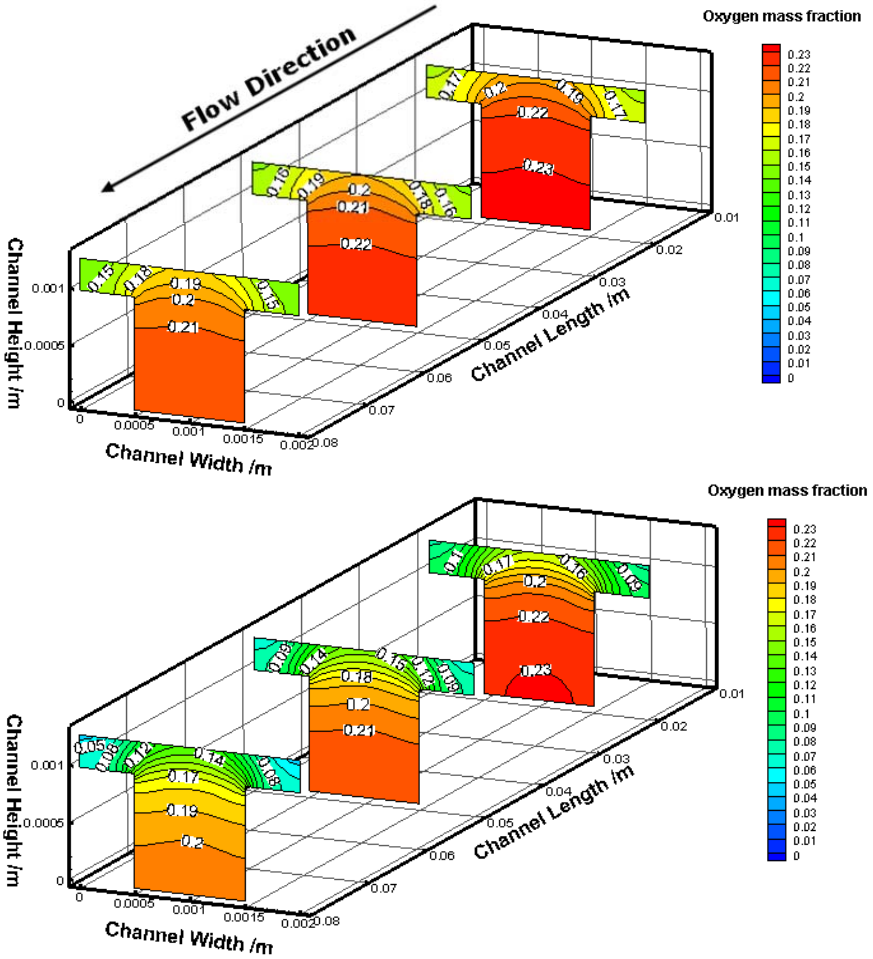

Figure 4.5 Oxygen mass fraction contour plot at cathode side at different average current densities: (upper) I = 0.5 Acm^{-2} and (lower) I = 1.0 Acm^{-2}.

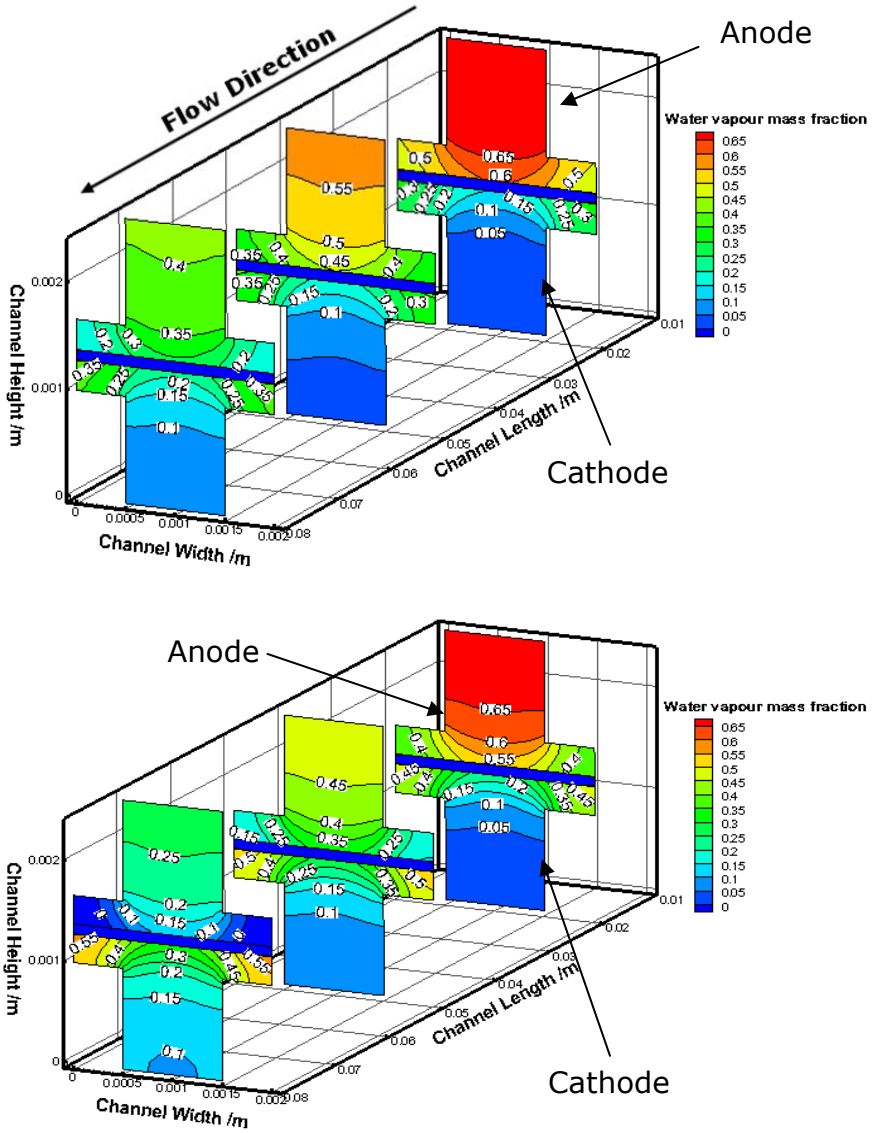

Figure 4.6 Water vapour mass fraction contour plot at different average current densities: (upper) I = 0.5 Acm^{-2} and (lower) I = 1.0 Acm^{-2}.

Figure 4.6 shows water vapour mass fraction contour plot (longitudinal slices) at anode and cathode sides at different average current densities (0.5 Acm^{-2} and 1.0 Acm^{-2}). It is observed that the water vapour mass fraction increases along the channel due to the depletion of oxygen in the cathode catalyst layer. Most of the water accumulation was observed under the land area in the cathode gas

diffusion layer and increased along the channel. This gives an idea about the potential regions where reactant transport becomes lower due to formation of liquid water. In these regions water vapour condense to form liquid water droplets. The produced liquid water droplet blocks the pore and, hence cell performance is reduced due to limitations of fresh reactants reaching catalyst layer. At higher current densities, a dried anode condition at the outlet was observed which leads to higher ohmic overpotential and reduced the cell voltage. Therefore, a multiphase model would be beneficial to investigate the water flooding in cathode GDL and CL.

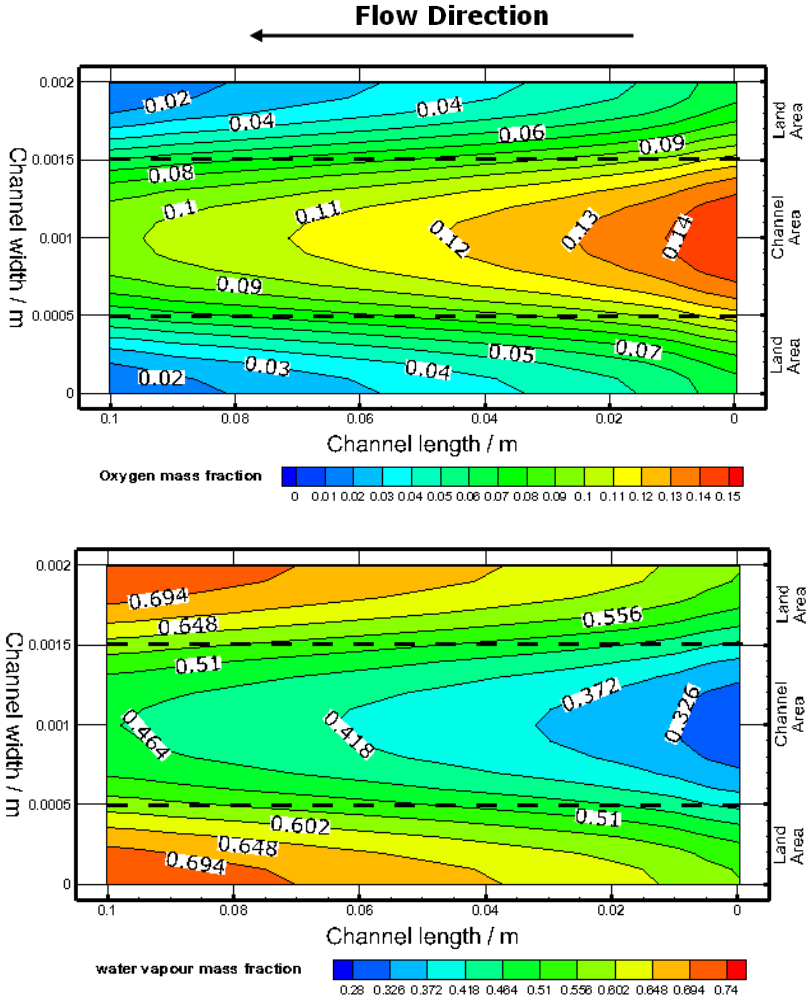

Figure 4.7 Oxygen and water vapour distribution at cathode catalyst layer/membrane interface.

Further detailed investigation is carried out to explore the transport limitation at higher current density using the current single-phase model. Figure 4.7 shows the oxygen and water vapour distribution at the cathode catalyst layer/membrane interface for average current density 1.0 Acm^{-2}. It is observed that oxygen concentration is reduced along the length and under the land area. A near zero oxygen mass fraction was observed at near the exit land area. In addition, more water vapour is formed under the land area. The amount of water vapour increases along the channel and close to exit is the most critical region where flooding is most likely to occur.

4.4 Parametric Study Using the Single-Phase PEM Fuel Cell Model

Parametric studies are conducted to investigate the effect of different parameters on PEM fuel cell performance. Based on the parametric study, an optimum PEM fuel cell design is proposed for improved performance. Several authors tried to examine the cell performance based on parametric studies. A brief summary of some of those research findings are presented in the next paragraph.

Berning and Djilali (2003) performed a parametric study to investigate the effect of operational parameters (for example, pressure, temperature) and geometrical and material parameters (for example, gas diffusion electrode thickness, porosity, and channel width and land area ratio) on PEM fuel cell performance. According to their study, it was observed that increasing temperature and pressure significantly improves the cell performance. The predicted cell performance reproduced the similar trends of experimental results (Ticianelli,

Derouin, and Srinivasan 1988, Kim et al. 1995). Stoichiometric flow ratio, gas diffusion porosity and thickness have a significant influence on limiting current density of PEM fuel cell as it controls the concentration of reactants to catalyst layer. Wang et al. (2003) conducted a parametric study based on experiments and compared model predicted results with an experimental data. Increasing fuel cell temperature and pressure showed an increasing trend in the cell performance. However, considerable effect of anode humidification temperature was observed at low current density. Similar trends were observed in the modelling results of Al-Baghdadi and Al-Janabi (2007 a, 2007 c) and Yuan et al. (2010).

Shimpalee and Zee (2007) investigated different serpentine flow field configurations to minimize the water flooding. According to their observation, narrow channel with wider land area configuration gives higher cell performance for stationary conditions. Therefore, flow field geometrical configurations and shoulder width plays a vital role on PEM fuel cell performance at high current density. (Ahmed and Sung 2006)

Lum and McGuirk (2005) found that decreasing shoulder width increase the cell potential significantly. Effect of decreasing permeability of porous regions on cell performance was investigated and a limiting permeability value (10^{-9} m^2) was identified from their study. Dawes et al. (2009) further investigate the effect of GDL permeability on cell performance and found the limiting value of 5×10^{-11} m^2. Rismanchi and Akbari (2008) showed that increase in gas diffusion parameters increase the cell performance, while no marked effect was observed by changing catalyst diffusion parameters.

Therefore, parametric studies are performed to identify optimum operating conditions and design parameters for the present model. The single-phase model is used to investigate the cell performance at high

current densities and fully humidified inlet conditions. Reactant flow along the channel is observed and possible transport limitation zones were identified.

4.4.1 Effect of Stoichiometric Flow Ratio

The effect of stoichiometric flow ratio is summarized in Figure. 4.8. An increase in stoichiometric flow ratio results in increasing the gas mixture velocities in both anode and cathode sides while all other parameters remain constant. Simulation studies were carried out for a range of stoichiometric ratio and significant influence on cell performance was observed.

It is shown in the Figure. 4.8 that cell performance is improved for higher values of stoichiometric ratio from 1.0 to 7.0. The model predicted results show an excellent agreement with experimental results for value equal to 3.0. However, the deviation at higher current density still exists. Therefore, this value can be used for better cell performance prediction at lower and intermediate current densities. A higher stoichiometric ratio means higher gas mixtures velocity. Therefore, more oxygen reaches at cathode catalyst layer and improves the reaction rate. In addition, excessive water productions at higher current densities cause flooding inside cell. Higher gas mixtures velocities help to improve water disposal rate from cathode. At low stoichiometric ratio, cell voltage dropped rapidly due to low amount of oxygen in catalyst layer at high current density. A large gain was observed for changing the value from 1.0 to 3.0, and increasing trend for increasing stoichiometric ratio. However, small increase in cell voltage was observed for a stoichiometric ratio above 5.0. In addition, higher gas mixture velocities cause excess water removal from anode side and dehydration state of membrane. Therefore, an optimum value

of stoichiometric ratio is between 3.0 and 5.0 for maximizing cell performance at various operating conditions.

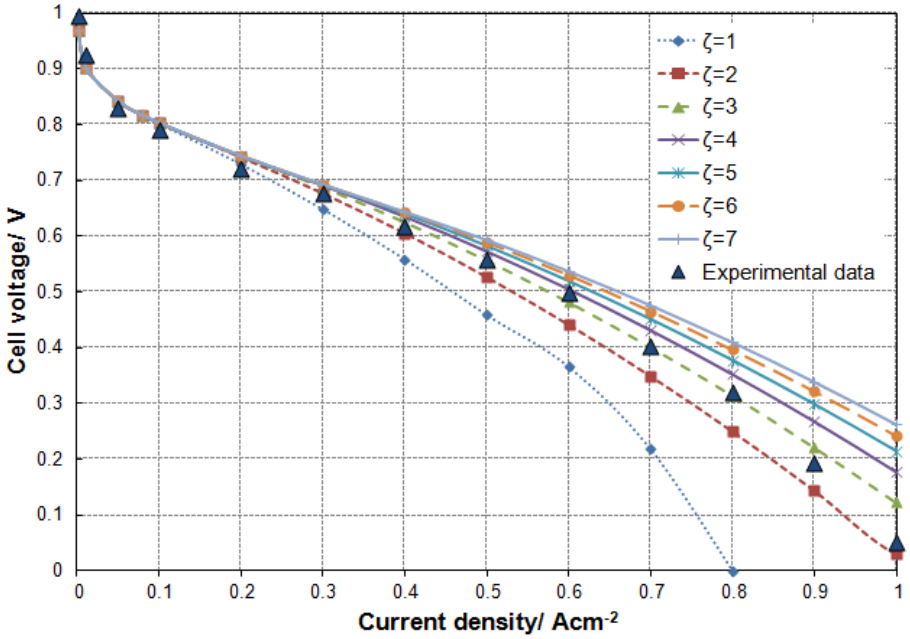

Figure 4.8 Effect of stoichiometric flow ratio on cell performance at different average current densities.

Oxygen mass fraction contour plots at different locations of cathode side along the length for different stoichiometric ratio at an average current density of 1.0 Acm^{-2} are shown in Figure. 4.9. A gradually decreasing trend along the length is observed. Low oxygen concentration is monitored at GDL and CL for lower stoichiometric ratio. Oxygen mass fraction becomes zero under the land area near the exit of the channel. While, for higher stoichiometric ratio, more evenly distribution of oxygen is observed in the porous zones.

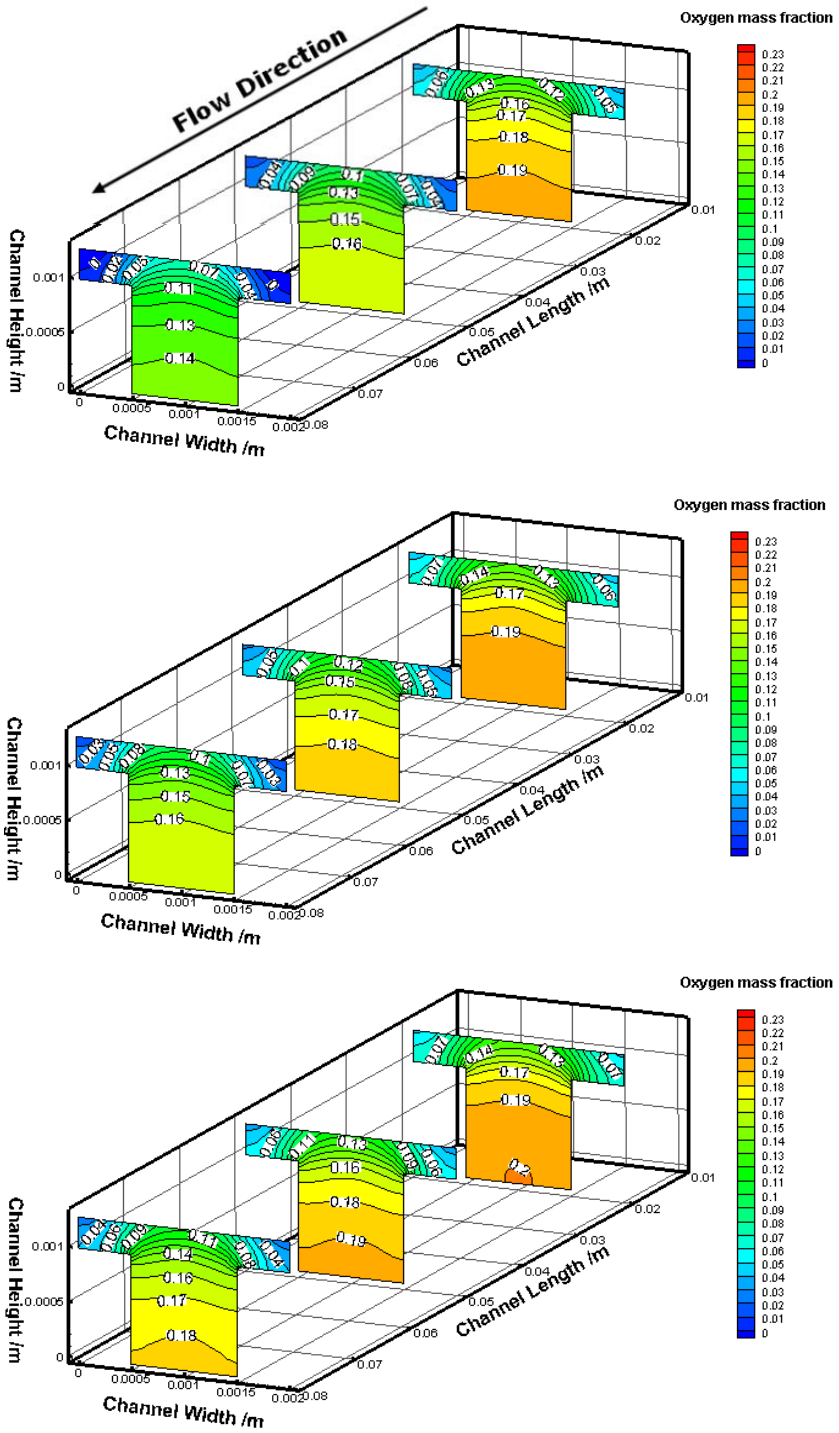

Figure 4.9 Oxygen mass fraction contours at different longitudinal direction for ζ = 2 (upper), ζ=5 (middle) and ζ= 7 (Lower) at I = 1.0 Acm^{-2}.

4.4.2 Effect of GDL Permeability

Simulations were performed for different values of GDL permeability and the results are summarized in the Figure. 4.10. The cell performance decreases for decreasing GDL permeability up to a certain range. From the Figure. 4.10, it is clear that no change in cell voltage is observed for a permeability value lower than 10^{-11} m^2. At lower current densities, the change in GDL permeability has no effect on cell performance. However, GDL permeability influences the cell at higher current densities. Lower permeability exhibit higher resistance to flow through porous medium, hence limits the disposal of water. In order to investigate this influence further, oxygen mass fraction contour plots at different locations of cathode side along the length for an average current density of 1.0 Acm^{-2} are plotted in Figure. 4.11.

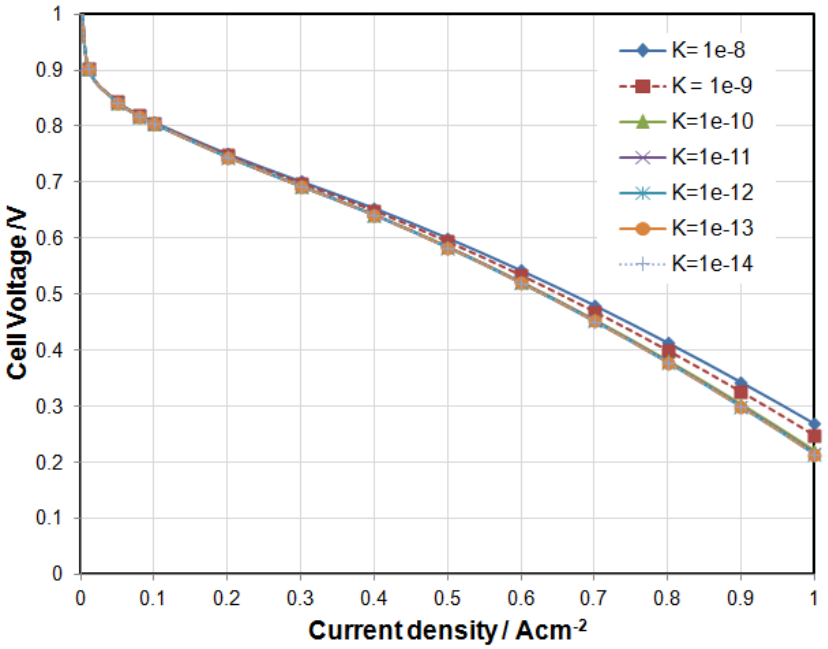

Figure 4.10 Effect of GDL permeability on cell performance at different average current densities.

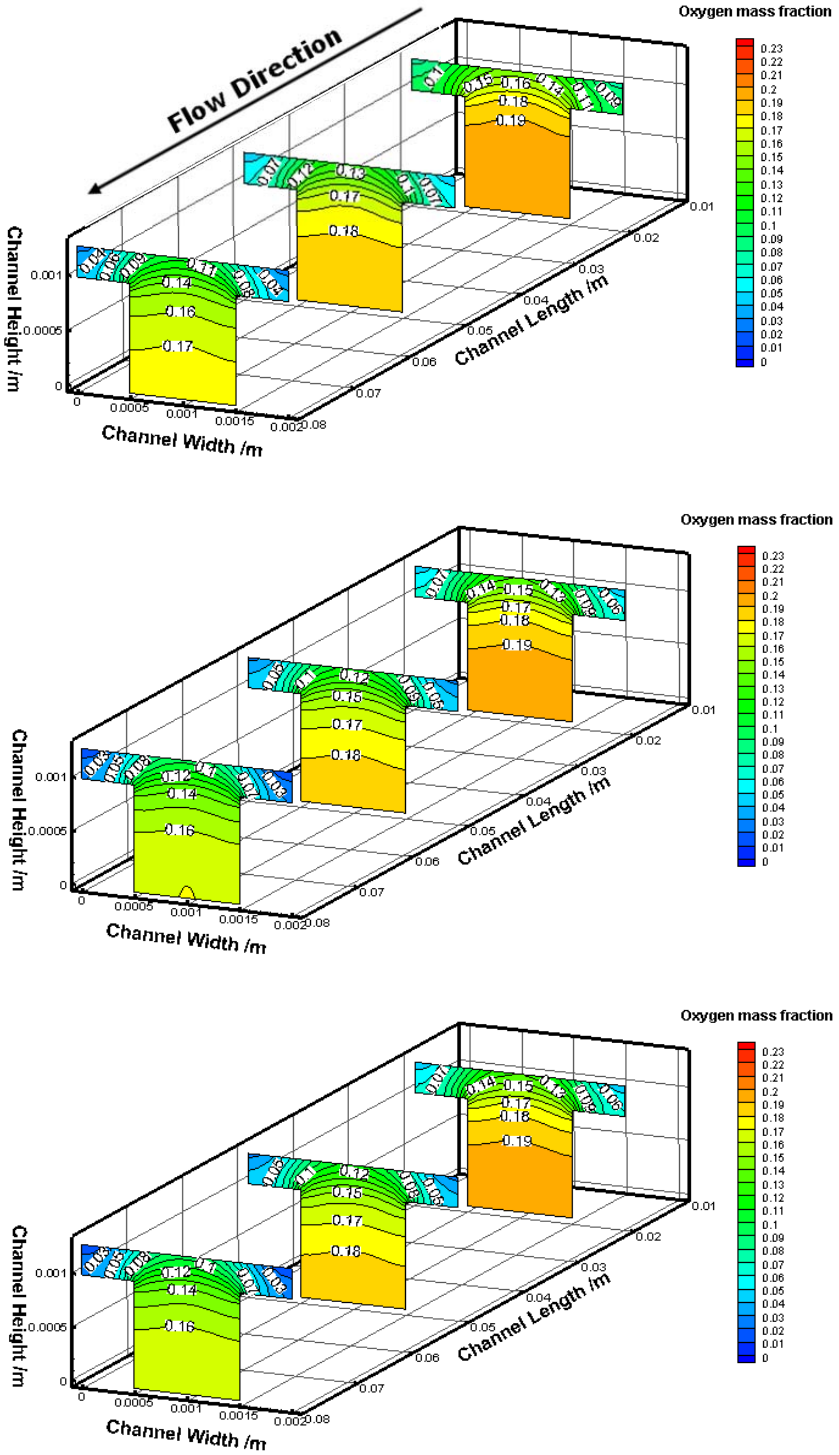

Figure 4.11 Oxygen mass fraction contours along the channel length for permeability 10^{-8} m^2 (upper), 10^{-10} m^2 (middle) and 10^{-12} m^2 (Lower) at I = 1.0 Acm^{-2}.

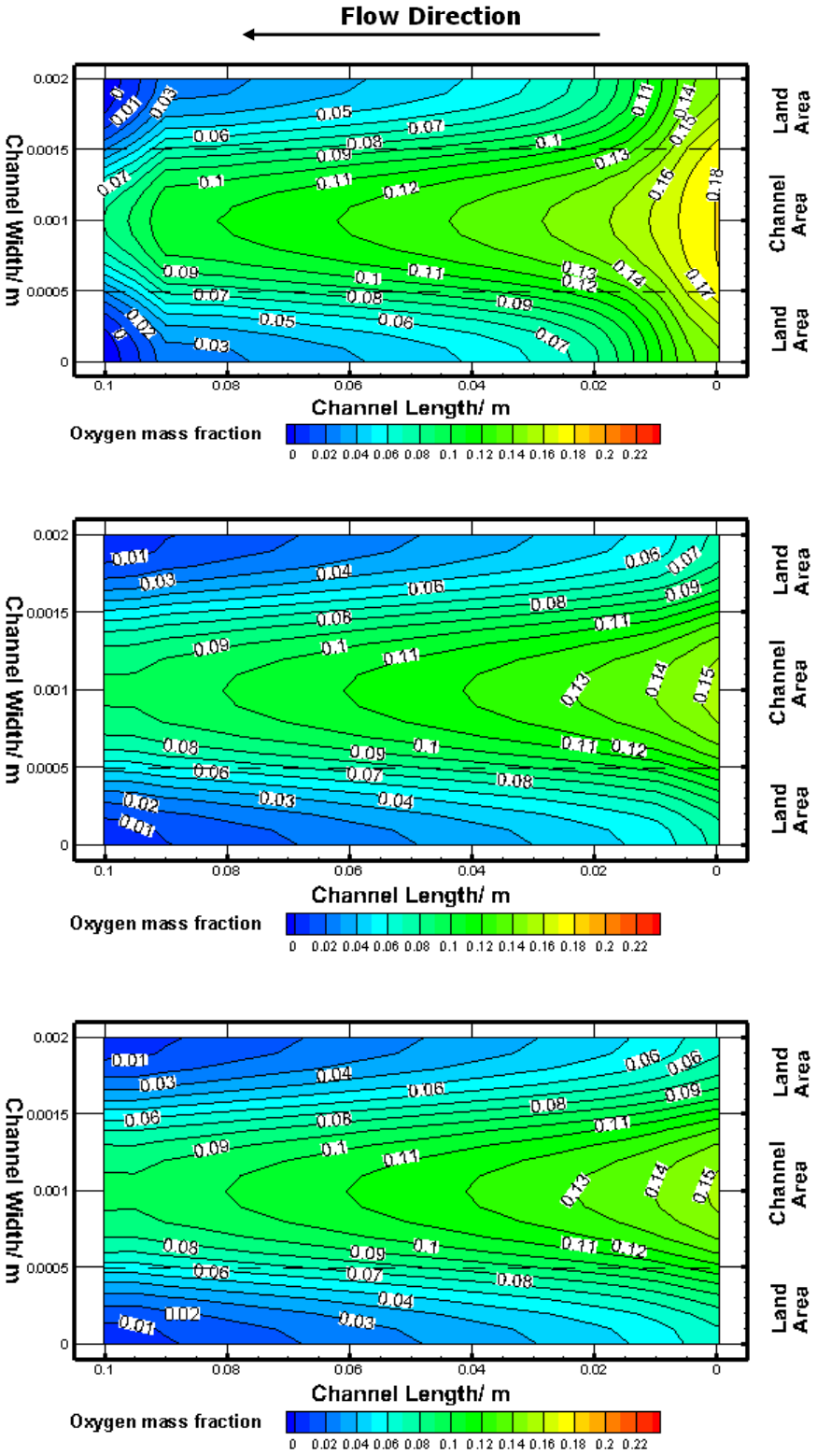

Figure 4.12 Oxygen mass fraction contours at GDL/CL interface for permeability 10^{-8} m^2 (upper), 10^{-10} m^2 (middle) and 10^{-12} m^2 (Lower) at I = 1.0 Acm^{-2}.

Higher concentration of oxygen in the GDL and CL section was observed for higher permeability. As the permeability decreased, the concentration of oxygen is decreased for higher flow restriction. However, no significant changes in mass fraction distribution were monitored for value 10^{-12} m^2 compared to 10^{-10} m^2. Oxygen mass fraction contours are plotted at GDL/CL interface in the Figure. 4.12. Higher distribution of oxygen concentration is observed at the interface for higher value of permeability. More oxygen concentration under the land area is monitored compared to lower permeability. Furthermore, no significant change in the distribution was observed for the lower range of permeability values.

4.4.3 Effect of CL Permeability

Simulations were carried out for different values of CL permeability and the results are summarized in the Figure. 4.13. From the Figure. 4.13, it is clear that no significant change in cell voltage is observed for the range of permeability values.

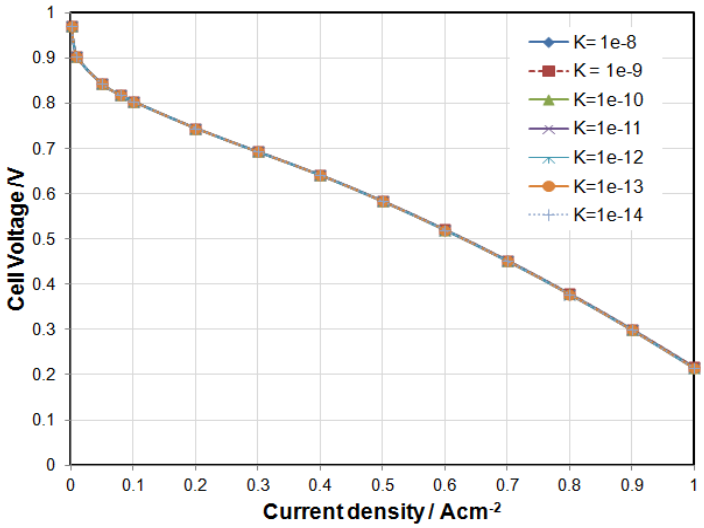

Figure 4.13 Effect of CL permeability on cell performance at different average current densities.

This is due to the same value used in the model for GDL permeability (10^{-10} m^2). The reactant receives similar restriction in the GDL before coming to the catalyst layer and oxygen concentration remains unchanged before reaching CL. In order to investigate this influence further, oxygen mass fraction contour plots at CL/membrane interface at different locations of cathode side along the length for an average current density of 1.0 Acm^{-2} are plotted in Figure. 4.14. No significant change in distribution is observed from the Figure.4.14.

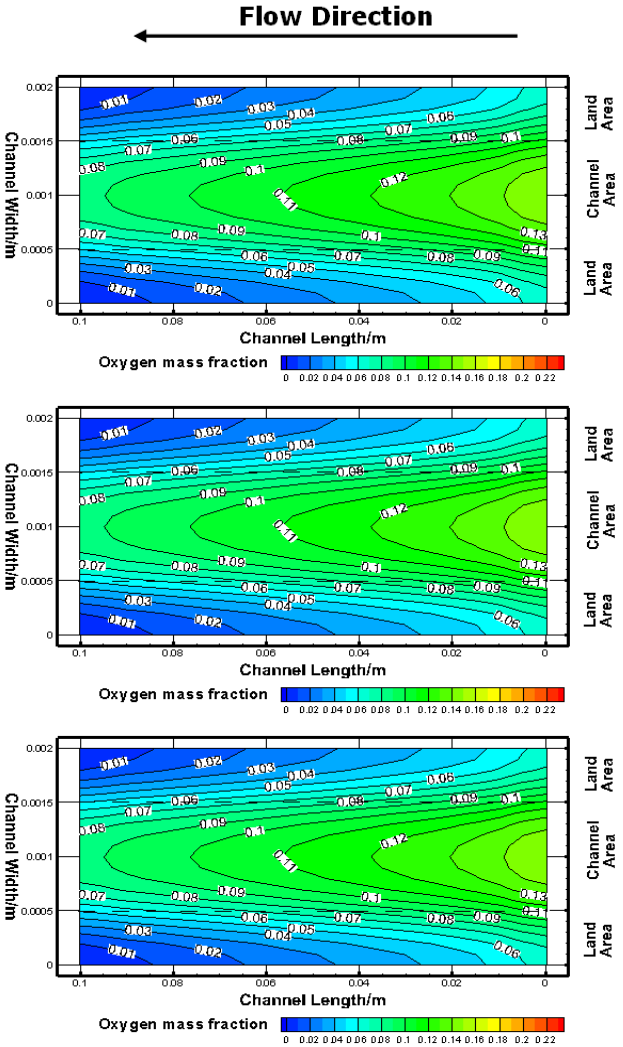

Figure 4.14 Oxygen mass fraction contours at CL/membrane interface for permeability 10^{-8} m^2 (upper), 10^{-10} m^2 (middle) and 10^{-12} m^2 (Lower) at I = 1.0 Acm^{-2}.

4.4.4 Effect of GDL Porosity

Simulations were performed for different values of GDL porosity and the results are summarized in the Figure. 4.15. It is observed that porosity has a strong influence on cell performance as the transport of reactant is primarily diffusive in porous medium. Higher values of porosity means higher void fraction available for the reactants in the porous medium with lower restriction to flow. Higher concentrations of reactants lead to higher limiting current density for the fuel cell. Figure 4.15 shows that cell performance increases with increasing GDL porosity. No significant influence was observed for a value higher than 0.5. In addition, rapid drop in cell voltage is observed for lower GDL porosity. Oxygen mass fraction contours along the length are plotted in Figure. 4.16. Starvation for reactants was observed at GDL and CL for lower GDL porosity.

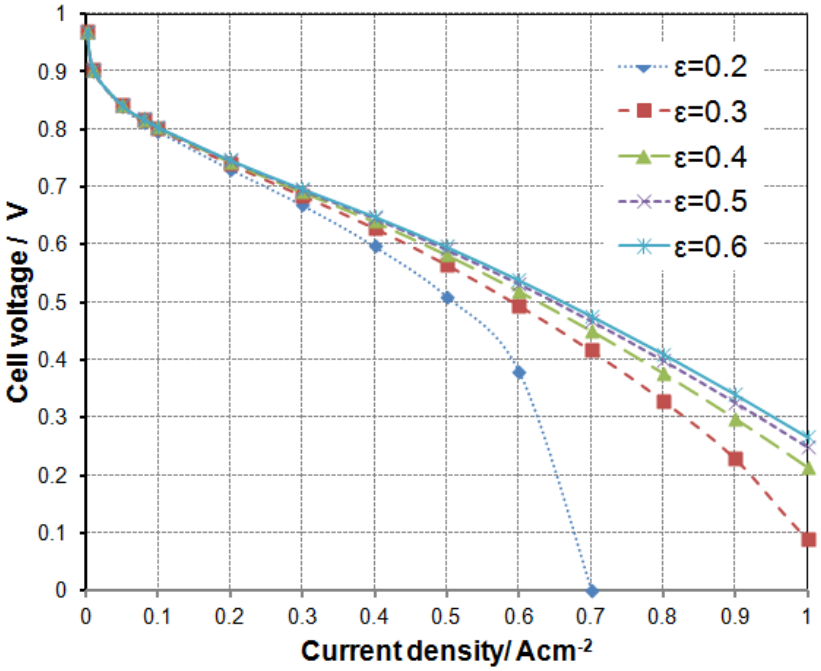

Figure 4.15 Effect of GDL porosity on cell performance at different average current densities.

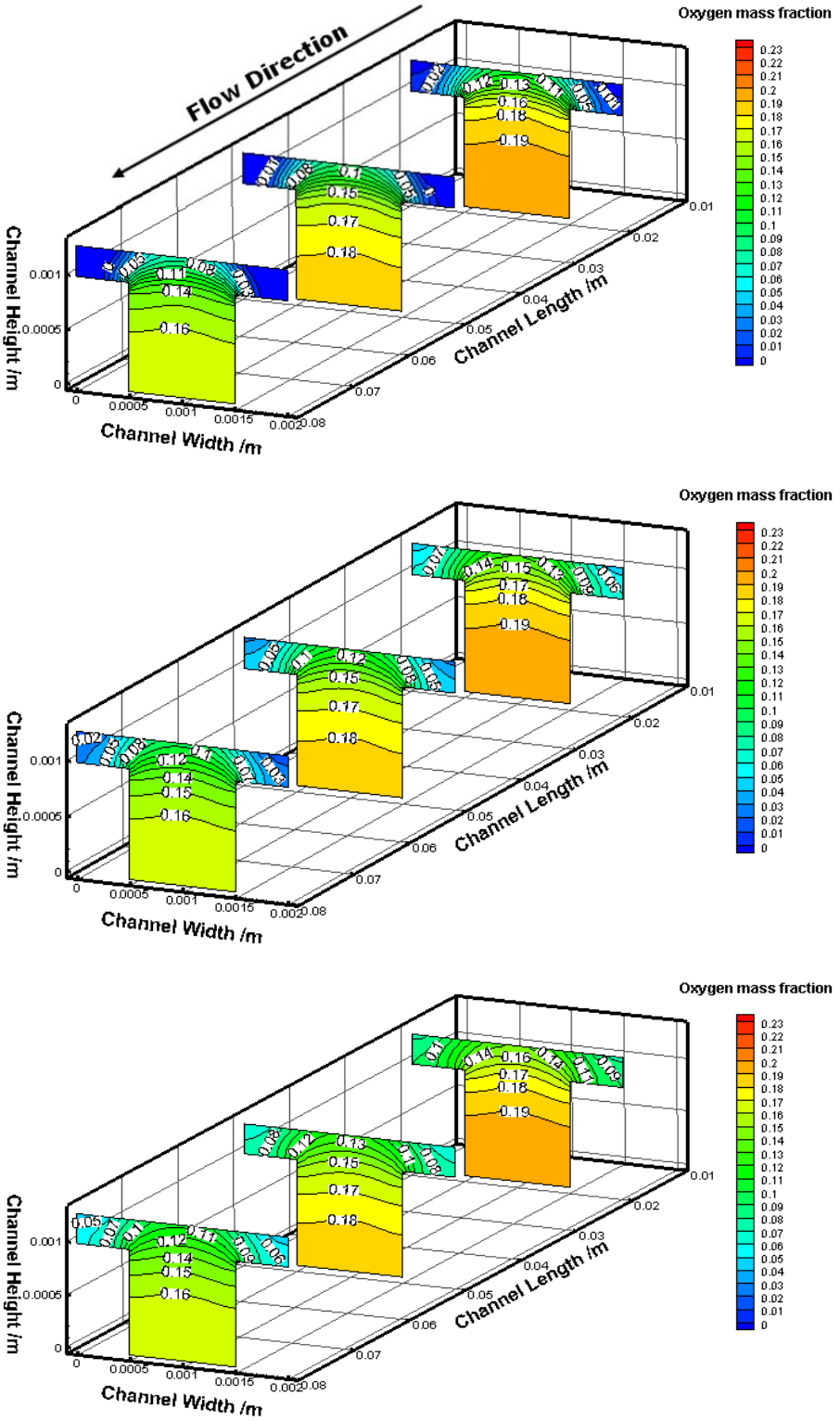

Figure 4.16 Oxygen mass fraction contours along the length for ε = 0.3 (upper), ε=0.4 (middle) and ε= 0.5 (Lower) at I = 1.0 Acm^{-2}.

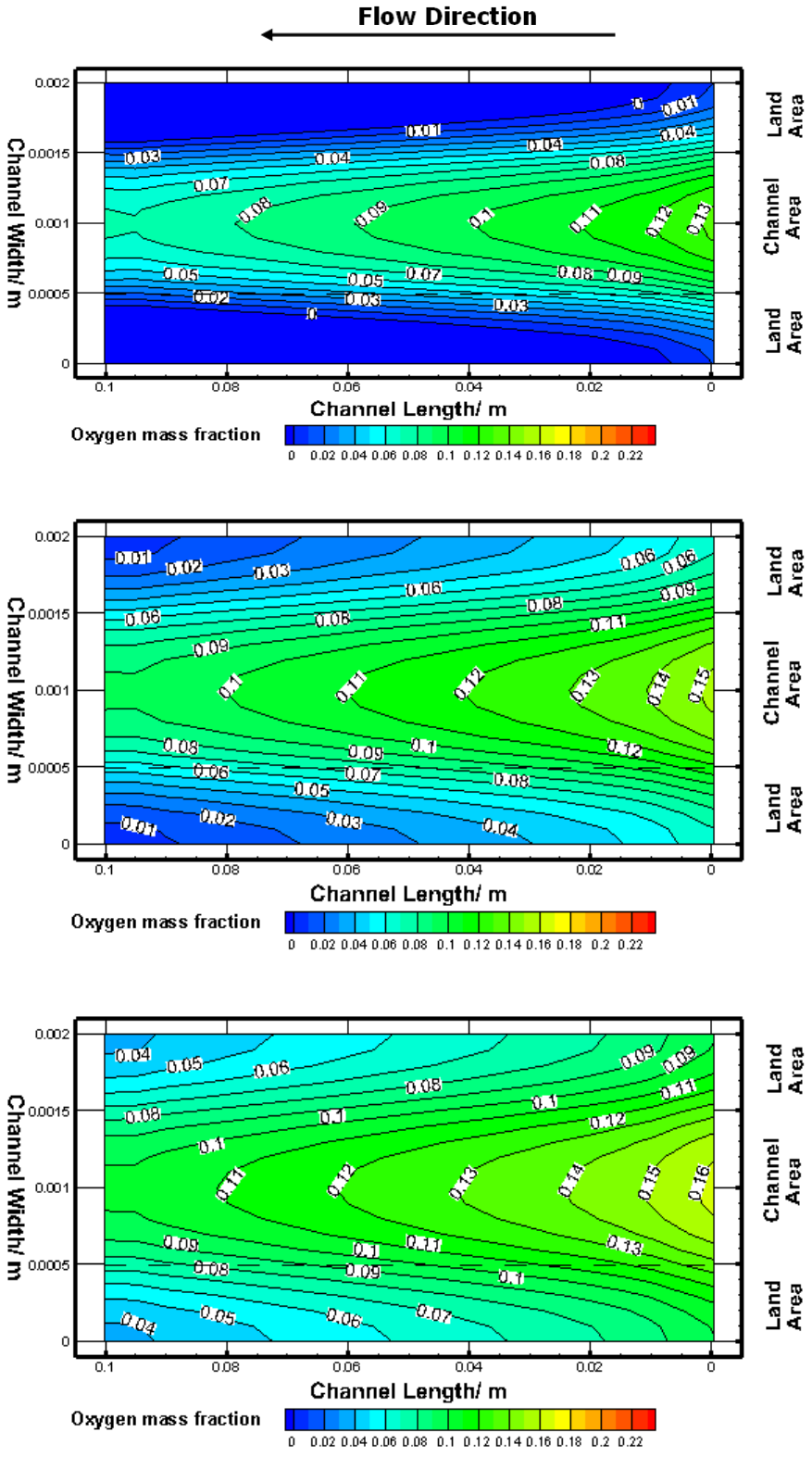

Figure 4.17 Oxygen mass fraction contours at GDL/CL interface for ε = 0.3 (upper), ε=0.4 (middle) and ε= 0.5 (Lower) at I = 1.0 Acm^{-2}.

4.4.5 Effect of CL Porosity

Simulations were performed for different values of CL porosity and the results are summarized in the Figure. 4.18. It is observed that there is a small deviation in cell voltage. Small decrease in cell voltage was monitored for decreasing porosity of CL. The simulation studies assumed a constant value of GDL porosity to be 0.4. Therefore, equal amount of oxygen are reaching catalyst layer to take part in the reaction. A higher CL porosity value would facilitate oxygen inside the CL. However, the effect is not as significant as the GDL porosity. Oxygen mass fraction contours along the length at CL/membrane interface are shown in Figure. 4.19. Very small difference in oxygen concentration distribution at CL near the exit of the channel for lower GDL porosity was observed.

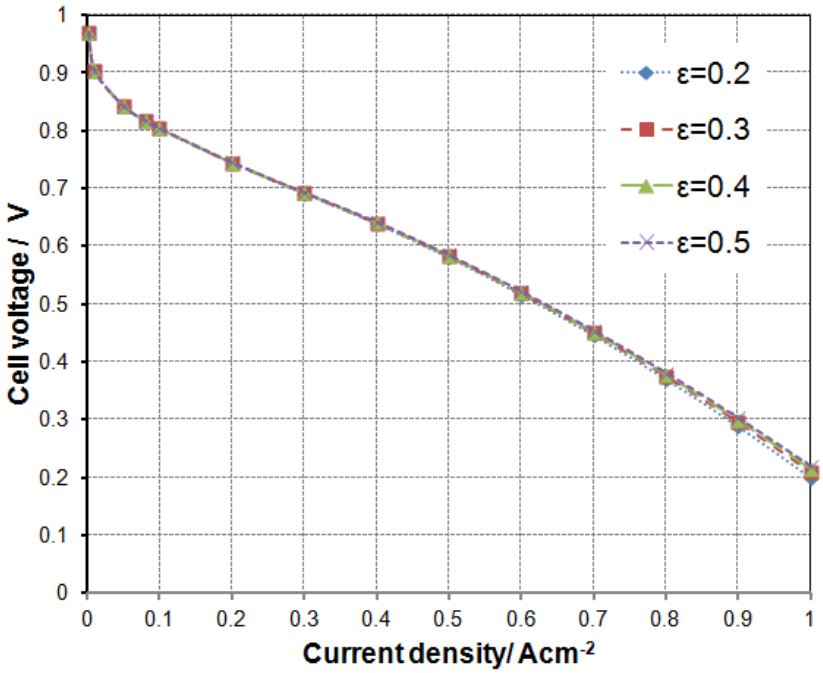

Figure 4.18 Effect of CL porosity on cell performance at different average current densities.

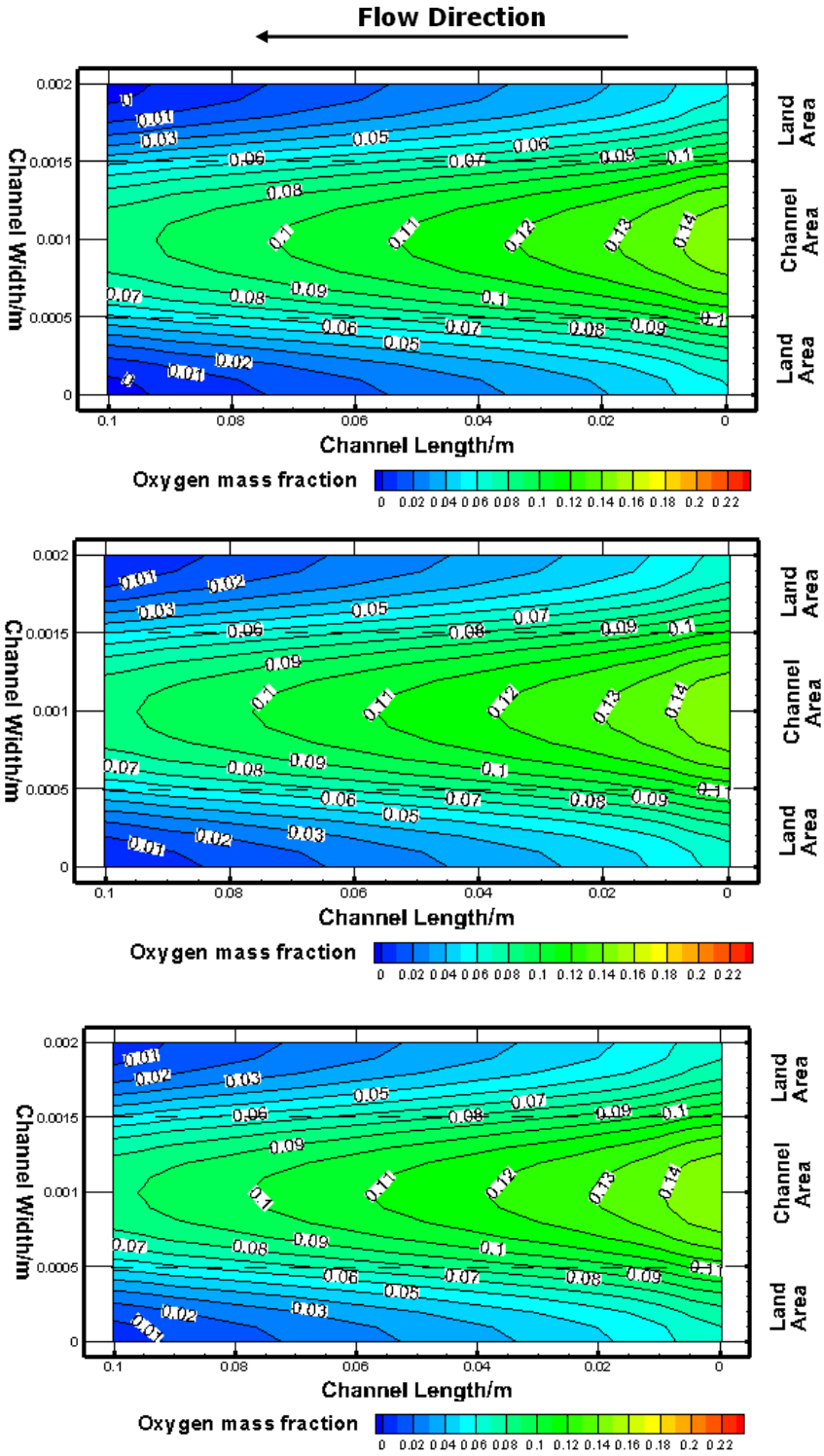

Figure 4.19 Oxygen mass fraction contours at CL/membrane interface for ε = 0.3 (upper), ε = 0.4 (middle) and ε = 0.5 (Lower) at I = 1.0 Acm^{-2}.

4.4.6 Effect of GDL Thickness

GDL thickness has an effect on mass transport losses inside cell. A thinner layer increase reactant transport through GDL, hence higher cell voltage is observed due to lower mass transport losses. Figure 4.20 shows that the cell voltage remains almost constant for the thickness value between 0.204mm and 0.254mm. Fuel cell voltage deteriorates for increasing the thickness to 0.304mm at higher current densities. Oxygen contour plots along the length for values of GDL thickness are shown in figure 4.21. It is obvious from the Figure 4.21 that thinner layer would increase oxygen concentration in the CL and improve the cell performance.

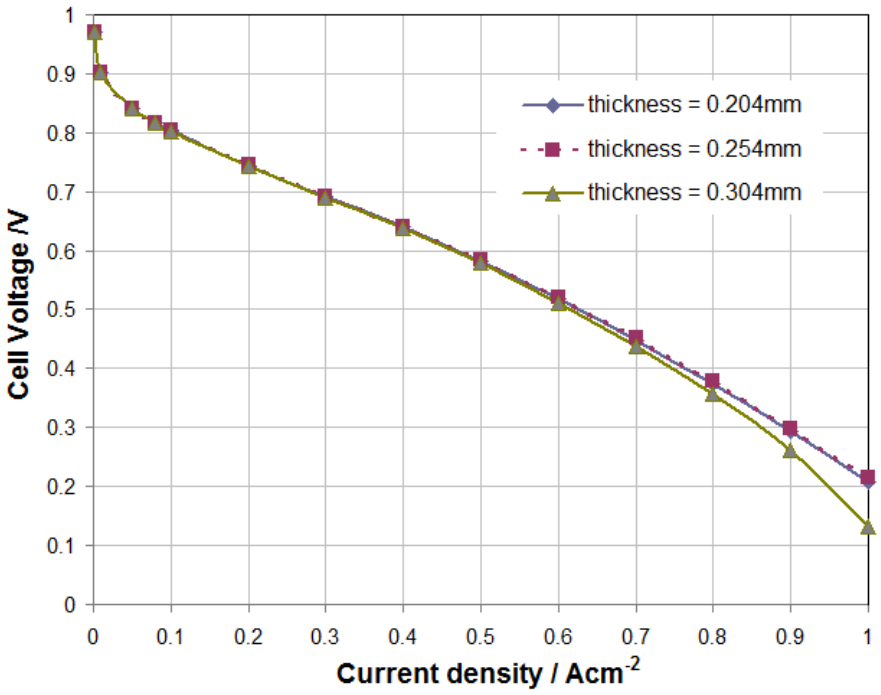

Figure 4.20 Effect of GDL thickness on cell performance at different average current densities.

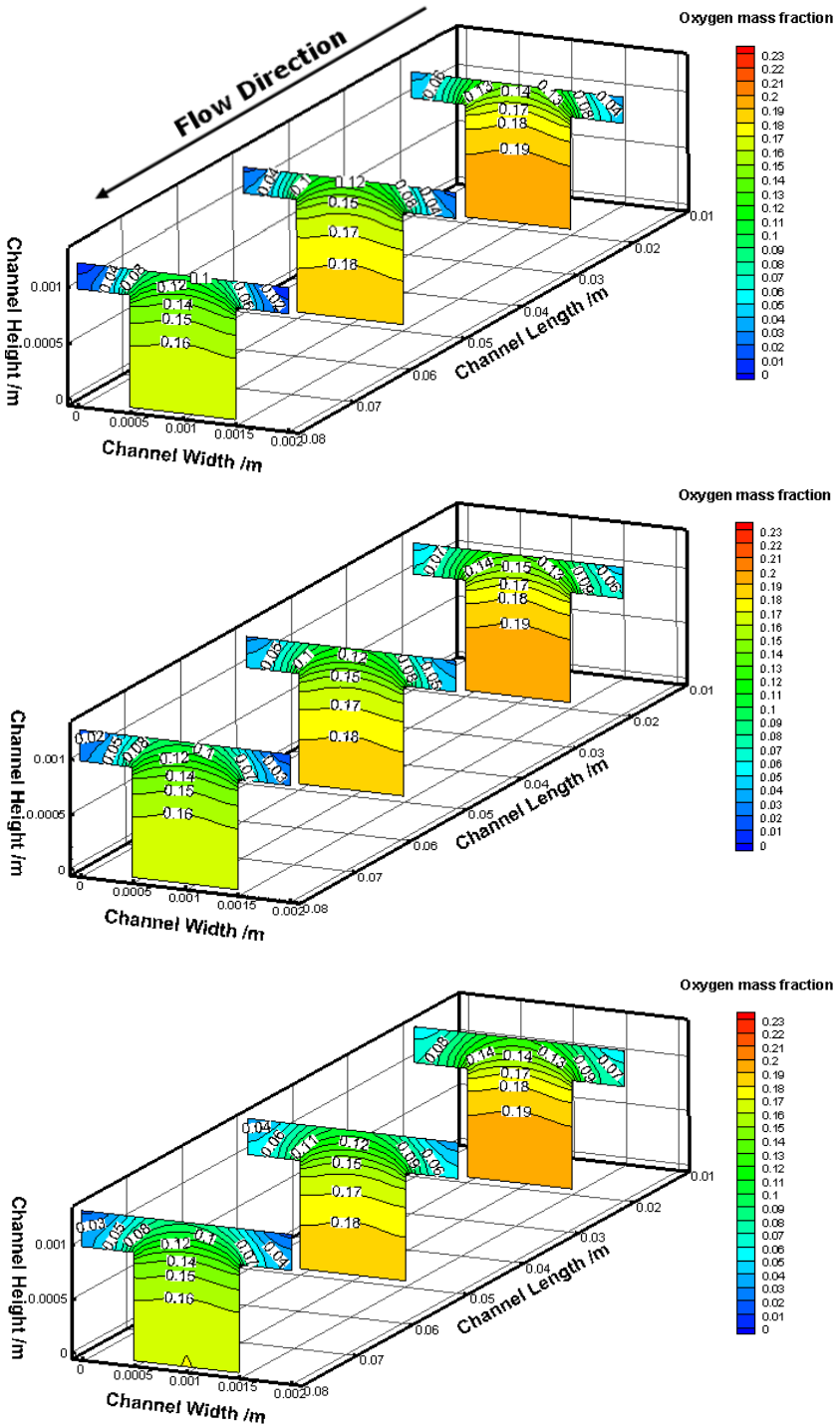

Figure 4.21 Oxygen mass fraction contours along the length for thickness 0.204mm (upper), 0.254mm (middle) and 0.304mm (Lower) at I = 1.0 Acm^{-2}.

4.4.7 Effect of CL Thickness

Parametric studies are performed based on CL thickness. The simulation results are summarized in the Figure.4.22. For a constant GDL thickness (0.254 mm), the values of CL layer thickness are changed from 0.0187 mm to 0.0387 mm. Almost similar cell voltage is predicted by the model. This is because the same amount of oxygen is coming to CL layer through GDL and the thickness of CL is not affecting the reaction rate. Oxygen contour plot at CL/membrane interface at an average current density of 1.0 Acm^{-2} suggests the negligible effect of CL thickness on cell performance. (Figure 4.23)

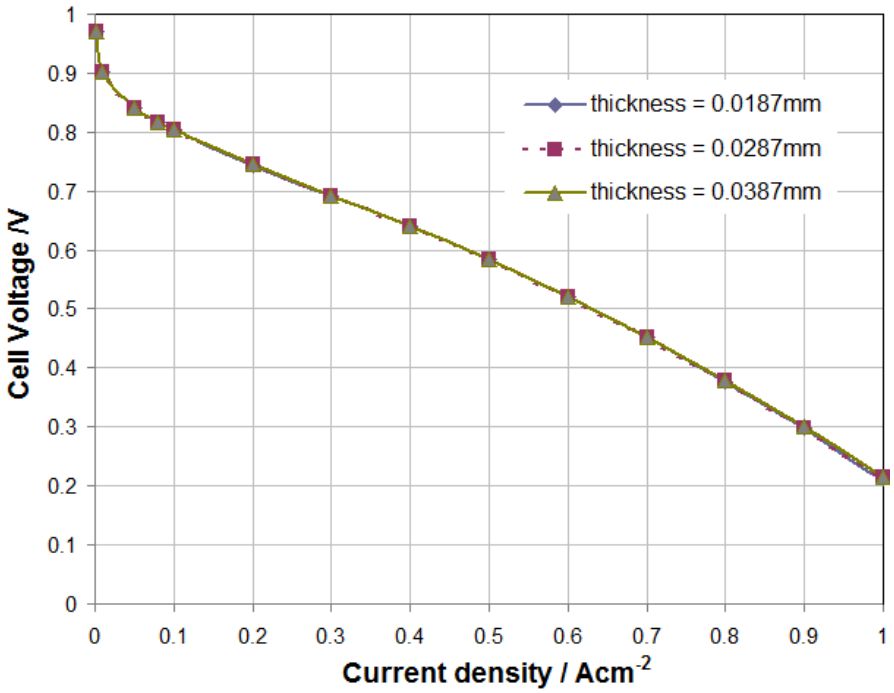

Figure 4.22 Effect of CL thickness on cell performance at different average current densities.

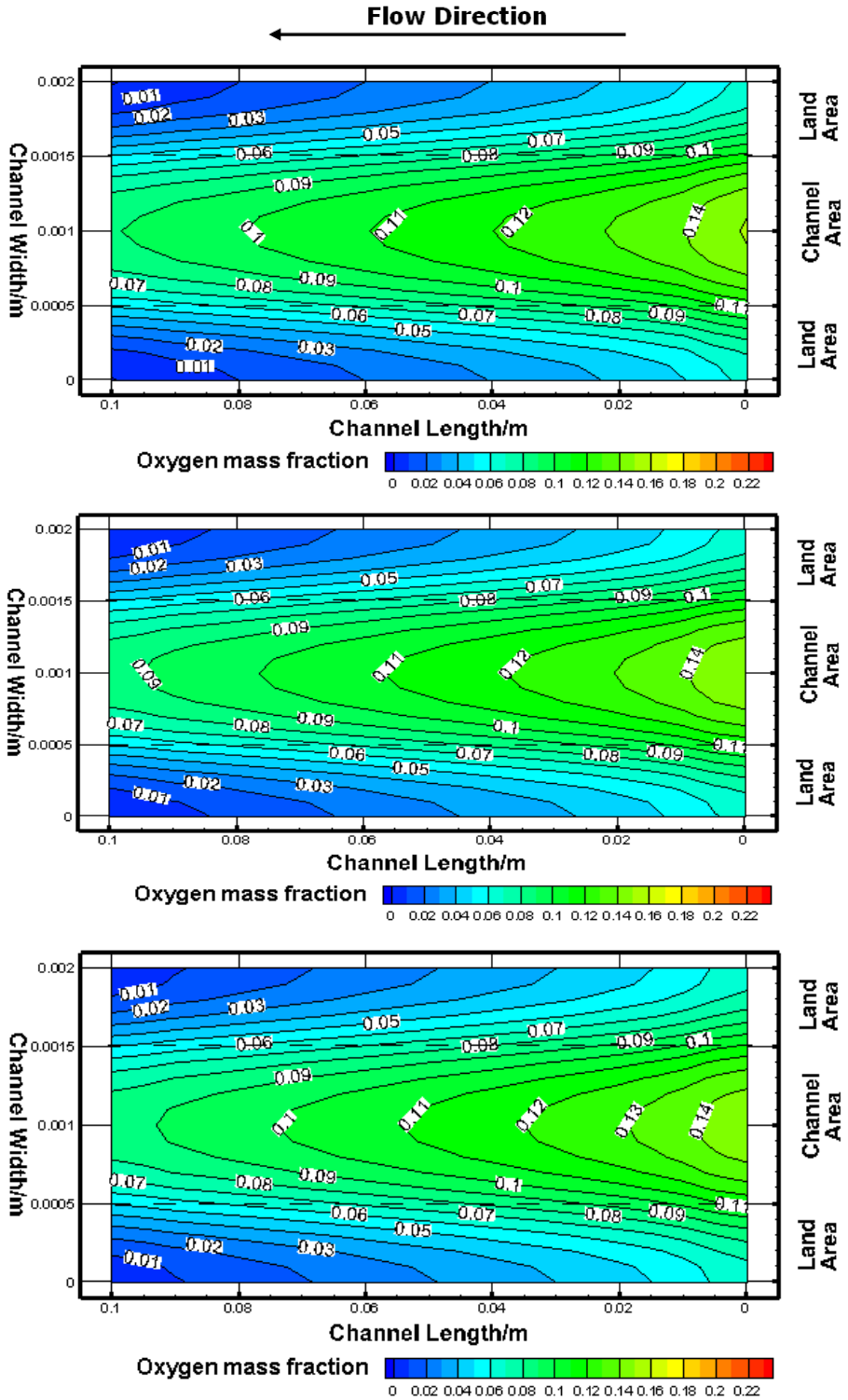

Figure 4.23 Oxygen mass fraction contours at CL/membrane interface for thickness 0.0187mm (upper), 0.0287mm (middle) and 0.0387mm (Lower) at I = 1.0 Acm^{-2}.

4.4.8 Effect of Channel-Width-to-Land-Area Ratio

A reduction in land area width increases the oxygen transport to catalyst layer. Simulations are performed for a constant channel area width of 1 mm and land area width values between 0.8 mm to 1.2 mm. From Figure 4.24, it is observed that decreasing the land area width has no effect at lower current densities. However, it has a strong influence at higher current densities. The cell voltage increases with decreasing land area width. This is due to more oxygen concentration in the CL and evenly distribution under land area. Oxygen mass fraction distributions at CL/membrane interface were studied to understand this effect further and shown in Figure. 4.25. At high current density, increase in land area width shows starvation of oxygen under the land area. Small land area facilitates more oxygen to reach CL layer for reaction.

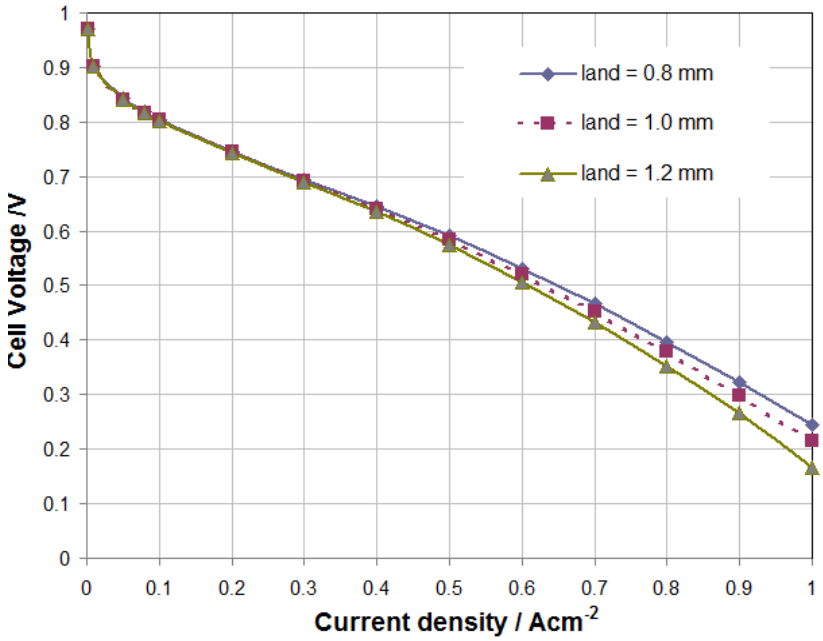

Figure 4.24 Effect of land area on cell performance at different average current densities.

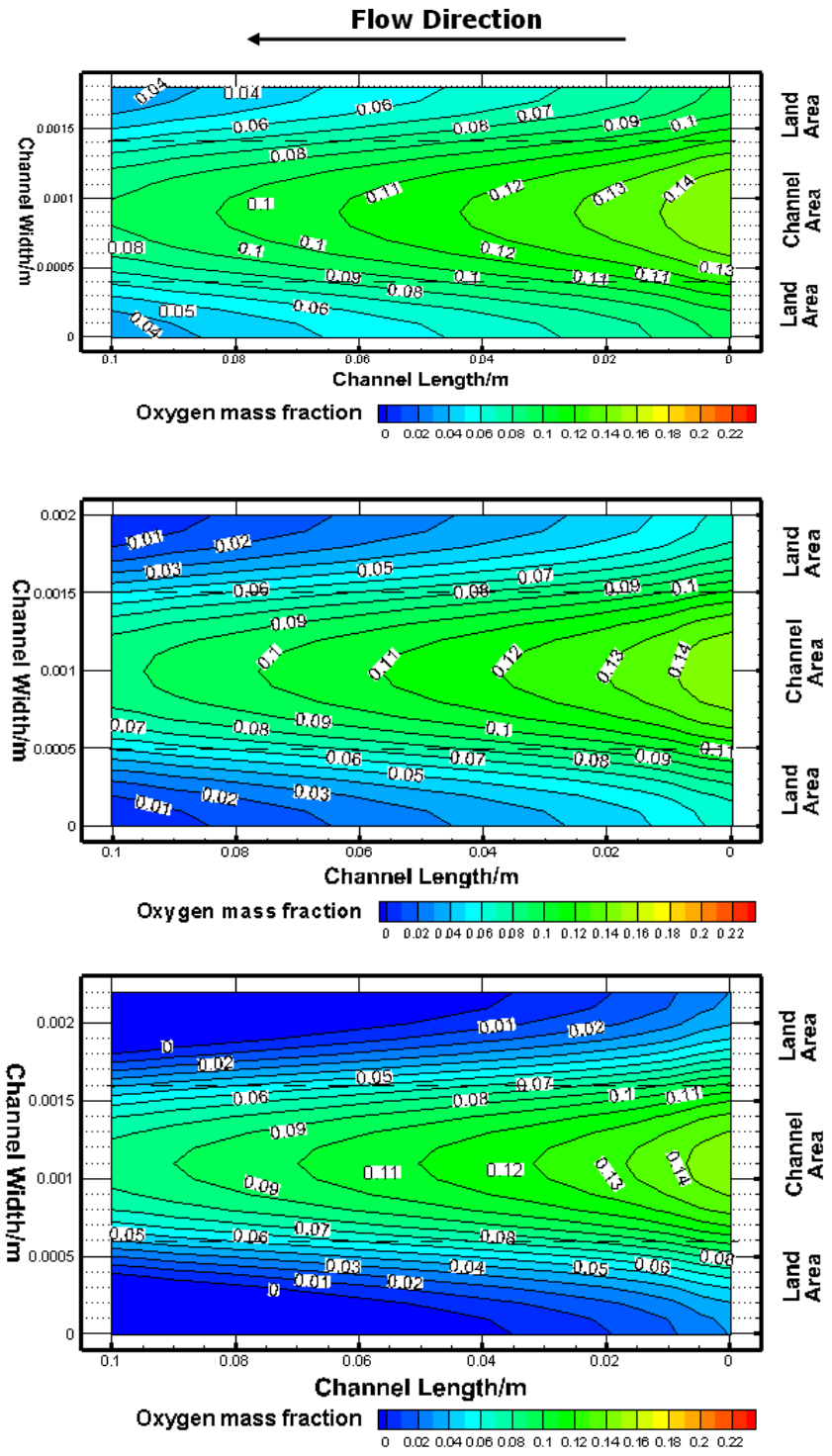

Figure 4.25 Oxygen mass fraction contours at CL/membrane interface for land area width 0.8mm (upper), 1.0mm (middle) and 1.2mm (Lower) at I = 1.0 Acm^{-2}.

4.4.9 Effect of Membrane Thickness

Membrane thickness affects the resistance of proton transport across the membrane. The ohmic overpotential occurs due to resistance to proton transfer across the membrane from anode CL to cathode CL. Lower values in membrane thickness suggest lower path need to be travelled and hence lower potential loss. Reducing membrane thickness leads to higher cell voltage and shown in Figure. 4.26.

In addition, the thickness of membrane has a strong influence on net water transfer across membrane. Lower membrane thickness facilitates more water to be transferred from anode side to cathode side. However dehydration in anode side is observed at higher rate of net water transfer and therefore increases the ohmic overpotential loss.

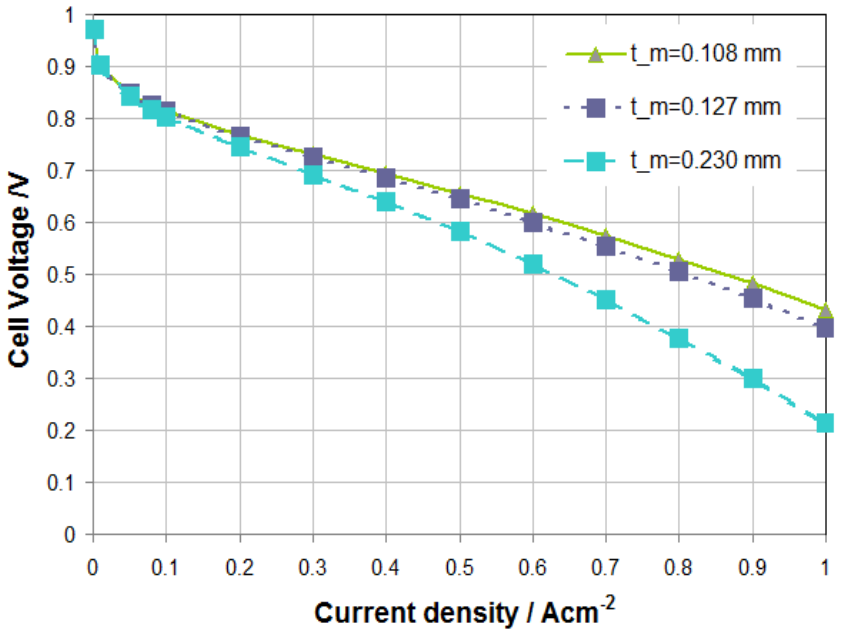

Figure 4.26 Effect of membrane thickness on cell performance at different average current densities.

4.5 Summary of Single-Phase Results

The simulated results obtained from the three-dimensional single-phase isothermal PEM fuel cell model have been presented in this chapter. A good agreement between simulated results and experimental results was observed for low current densities. The distributions of reactants in the cathode side along the length were presented to investigate the transport limitations inside cell at higher current densities.

The single-phase model is used to provide first approximation of the limitations of reactants transport in the porous layers at high current densities and identify the possible dehydration inside the cell. A parametric study was performed using this model to identify the optimum design parameters and operating conditions to improve fuel cell performance.

5

Chapter 5: Modelling optimization of effective diffusivity of Gas Diffusion Layers

As described in the last chapter that Bruggeman model has widely been used to represent species diffusion through porous GDL and CL. In this chapter, Bruggeman model is compared against diffusion models based on particle porous media, multi-length scales particle and percolation type correlation. The effects of these models on cell performance prediction are discussed in the following sections.

5.1 Diffusion Models

The effective diffusivity through porous medium is expressed as

$$D_k^{eff} = f(\varepsilon) D_k \tag{5.1}$$

where D_k^{eff} is the effective diffusivity and D_k is diffusivity of species in plain medium. $f(\varepsilon)$ is a function of porosity and various correlations are

available to determine the function. Most of the PEM fuel cell models use Bruggeman correlation to explain the diffusion of species through porous gas diffusion layers and catalyst layers.

According to Bruggeman correlation, the function is expressed as,

$$\boldsymbol{f(\varepsilon) = \varepsilon^{1.5}} \tag{5.2}$$

Dawes et al. (2009) developed a percolation theory based effective diffusivity model, where the function is expressed as,

$$\boldsymbol{f(\varepsilon) = \frac{(\varepsilon - 0.11)^{0.9}}{(1 - 0.11)^{0.9}}} \tag{5.3}$$

Neale and Nader (1973) used the following correlation to explain the diffusion through isotropic porous medium;

$$\boldsymbol{f(\varepsilon) = \frac{2\varepsilon}{3 - \varepsilon}} \tag{5.4}$$

Mezedur, Kaviany and Moore (2002) suggested diffusion model for multi-length scale, particle based porous medium as

$$f(\varepsilon) = 1 - \left(1 - \varepsilon\right)^{0.46} \tag{5.5}$$

Tomadakis and Sotirchos (1993) suggested the following percolation theory based diffusion model for random fibrous porous medium

$$\boldsymbol{f(\varepsilon) = \varepsilon \left(\frac{\varepsilon - \varepsilon_p}{1 - \varepsilon_p}\right)^{\alpha}} \tag{5.6}$$

where ε_p is the percolation threshold and equal to 0.11. α is an empirical constant which depends on the direction. The value of α is 0.521 for in-plane and 0.785 for cross-plane diffusion.

Predominate gas flow direction within a parallel or serpentine fuel cell channel is longitudinal. However, in order for the reaction to take place, reactant species diffuse through the GDL to the catalyst layer in perpendicular to main the flow direction. It is therefore expected that the diffusion of species plays a key role in species transport and this is the focus of this comparative study. Figure 5.1 shows a comparison of various diffusivity models against the most widely used Bruggeman model.

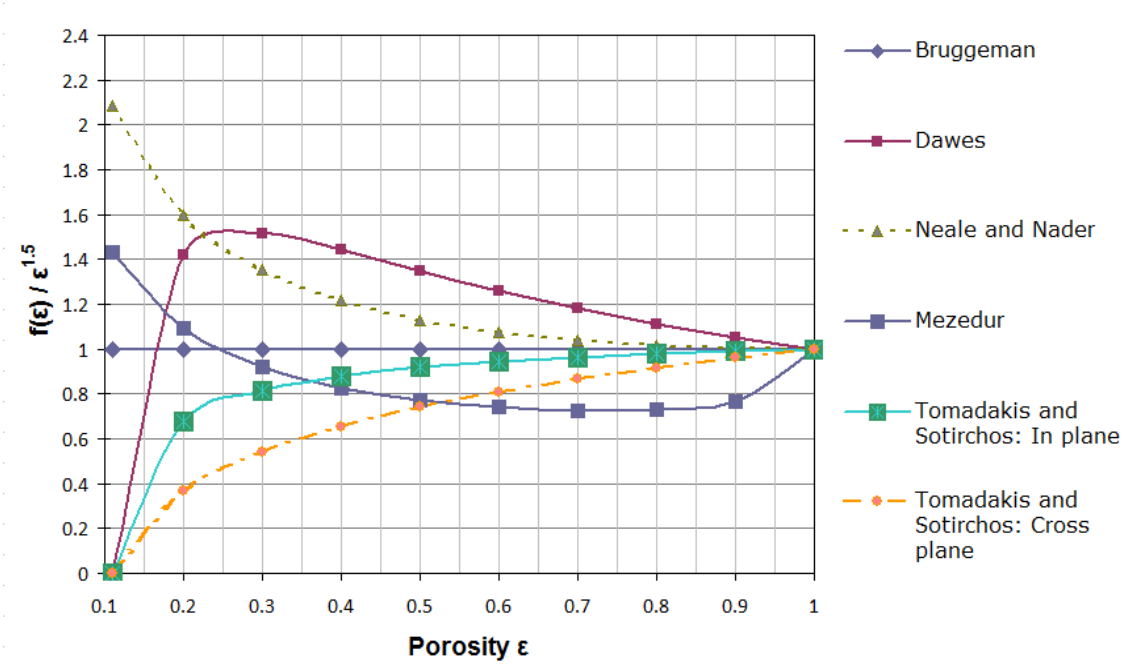

Figure 5.1 A comparison of various diffusivity models against the most widely used Bruggeman model.

It is observed from the Figure. 5.1 that Dawes et al. (2009) and Neale and Nader (1973) models produce higher values of effective diffusivity compared to the Bruggeman for a porosity value higher than 0.2, whereas Mezedur, Kaviany and Moore (2002) model starts at higher values of effective diffusivity, but quickly falls below the Bruggeman model for porosity values above 0.25. Tomadakis and Sotirchos (1993) is the only model that takes into account the anisotropy of GDL layer and shows in-plane diffusion is greater than the cross-plane diffusion and both in-plane and through-plane diffusion is lower than the Bruggeman model. The porosity of the GDL in the present single-phase model has been taken as 0.4. At this porosity, Dawes et al. (2009) model predicts approximately 40% and Neale and Nader model (1973) predicts 20% higher effective diffusivity compared to the Bruggeman model and Mezedur, Kaviany and Moore (2002), Tomadakis and Sotirchos (1993) in-plane and cross-plane models predict approximately 15%, 20% and 35% less diffusivity respectively, compared to the Bruggeman model. The extents to which these differences in effective diffusivity contribute to the overall fuel cell performances are discussed below.

5.2 Cell performance for different diffusivity models

Figure 5.2 shows the effect of effective diffusion coefficients on the fuel cell performance at different average current densities. The figure also shows experimental data of Ticianelli, Derouin, and Srinivasan (1988). For average current densities below 0.5 Acm^{-2}, not so much differences in cell voltages prediction among different diffusivity models have been observed. While, for higher current densities significant variations have been observed up to average current density of 1.0 Acm^{-2}. Both Mezedur, Kaviany and Moore (2002) and Tomadakis and Sotirchos (1993) anisotropic model provide much closer prediction compared to

the experimental data. In particular, Tomadakis and Sotirchos (1993) anisotropic model prediction is very close to experimental data, though there is still discrepancy between the simulation and experimental value. This difference is attributed to the single phase modelling of water in vapour form.

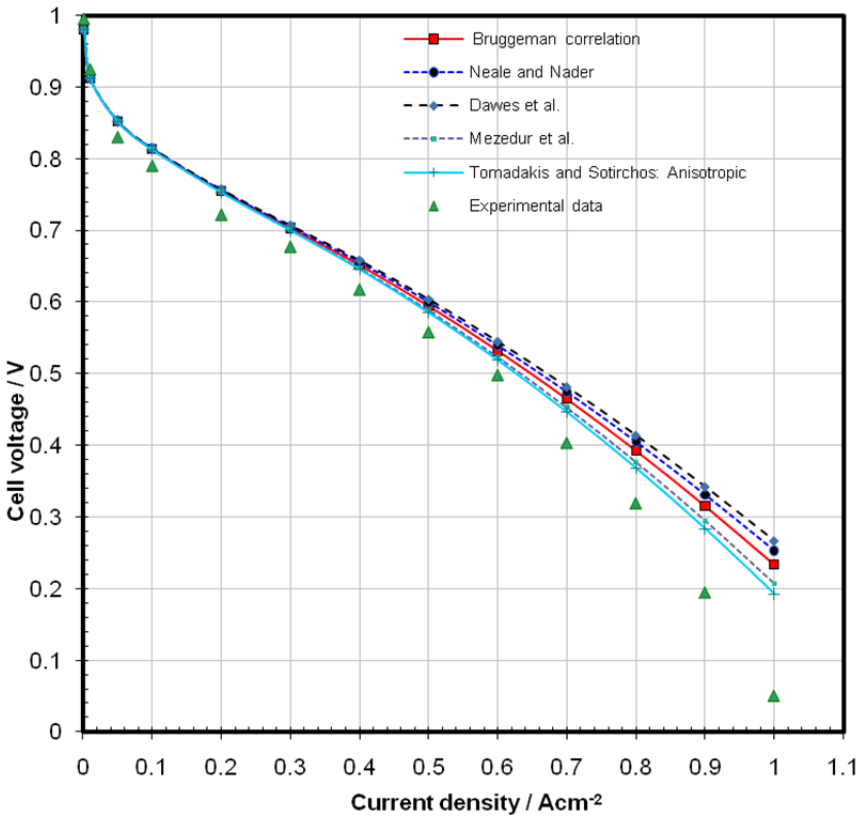

Figure 5.2 The effect of effective diffusion coefficients on the fuel cell performance at different current densities. (experimental data of Ticianelli, Derouin, and Srinivasan 1988)

To understand the variation of cell performance with different diffusivity models, oxygen and water vapour contour plots in the cathode side have been plotted. Figure 5.3 shows the oxygen contour plots at middle section of PEM fuel cell model for three different

effective diffusivity correlations. The variations were investigated along the length of the fuel cell. It is observed from the figure that Dawes et al. (2009) percolation based effective diffusivity model over-predict the oxygen concentration in the catalyst layer compared to Bruggeman correlation and Tomadakis and Sotirchos (1993) in plane diffusion model. Therefore, a higher cell voltage was observed for higher current densities using Dawes et al. (2009) model. In addition, changing the effective diffusivity models has an effect on the limiting current density of the fuel cell. Hence, the concentration overpotential would vary for the models.

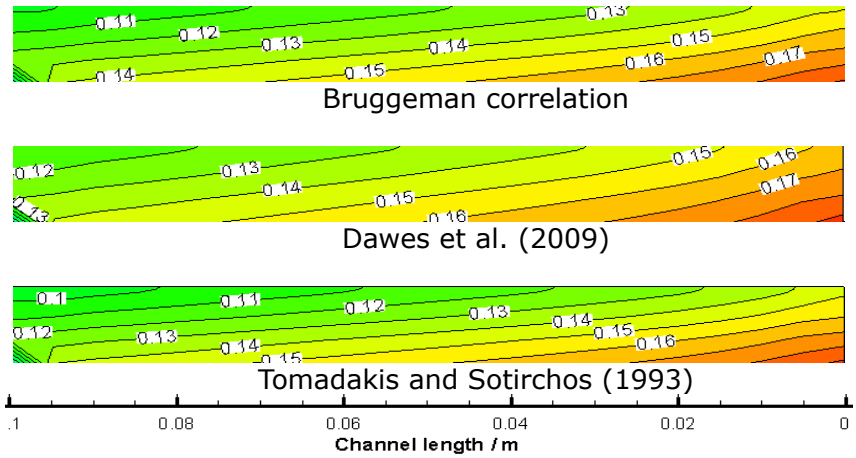

Figure 5.3 oxygen contour plot in cathode GDL and CL for different effective diffusion models.

Figure 5.4 shows the oxygen contour plots at catalyst/membrane interface at average current density of 0.5 Acm^{-2} and 1.0 Acm^{-2}. At both current densities, mass fraction of oxygen has been over-predicted by Dawes et al. (2009) and Neale and Nader (1973) models compared to the Bruggeman correlation, while Mezedur, Kaviany and Moore (2002) and Tomadakis and Sotirchos (1993) model under-predict the mass fraction of oxygen.

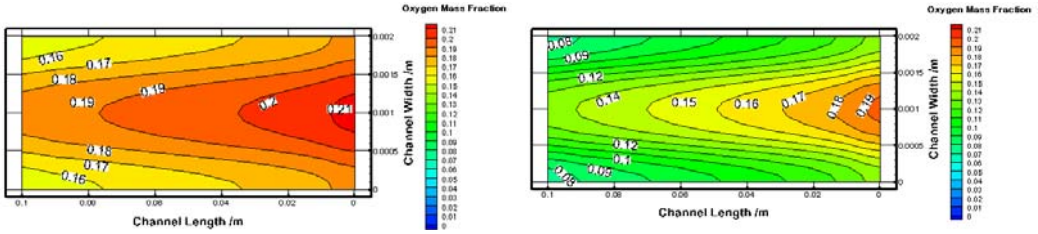

(a) Dawes et al. (2009)

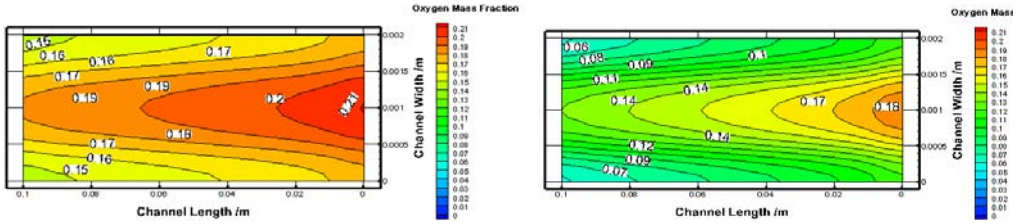

(b) Neale and Nader (1973)

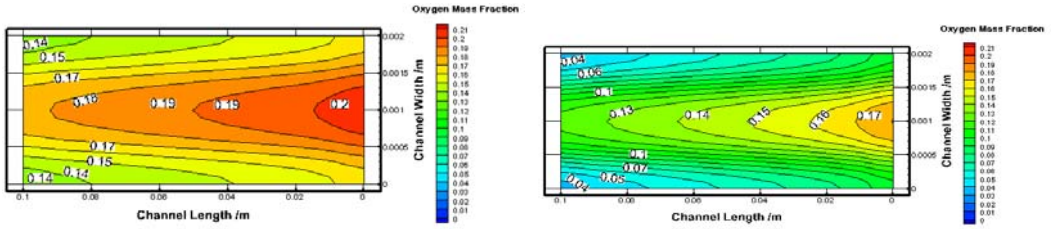

(c) Bruggeman

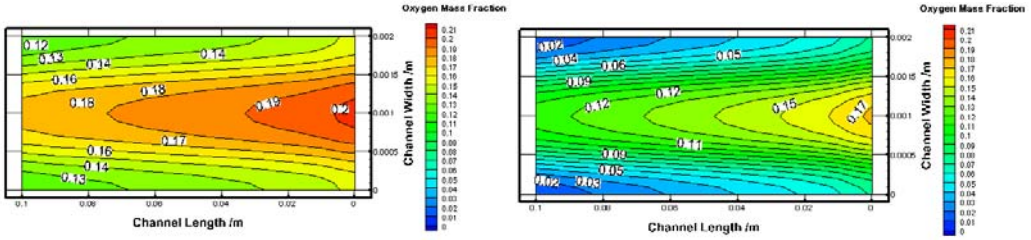

(d) Mezedur, Kaviany and Moore (2002)

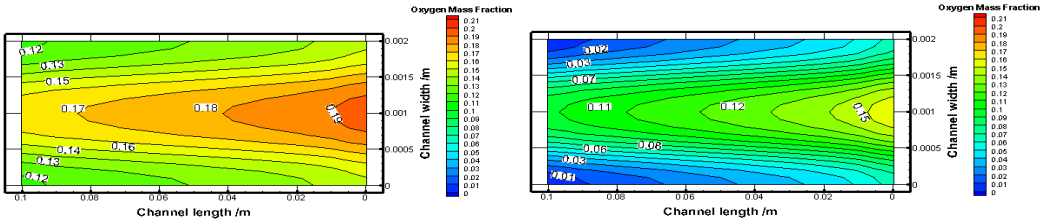

e) Tomakadis and Sotirchos (1993)

Figure 5.4 Oxygen contour plots at catalyst/membrane interface at an average current density of 0.5 Acm^{-2} (left) and 1.0 Acm^{-2} (right).

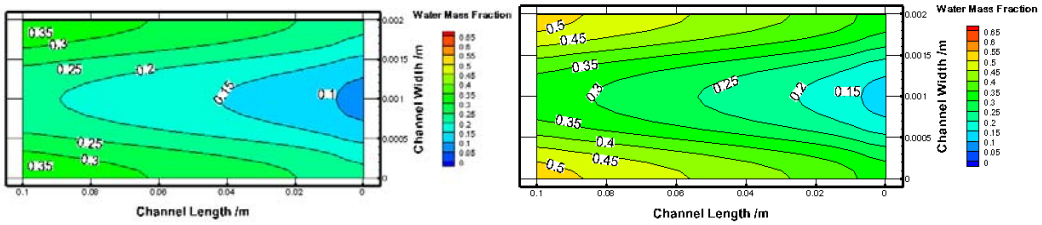

(a) Dawes et al. (2009)

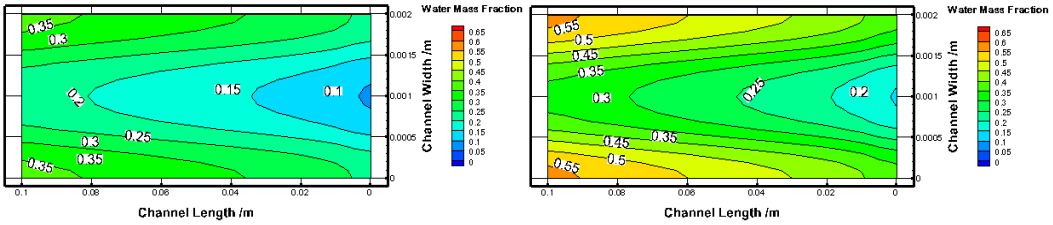

(b) Neale and Nader (1973)

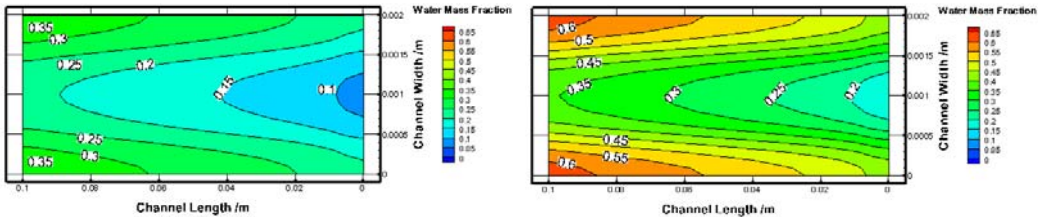

(c) Brugemman

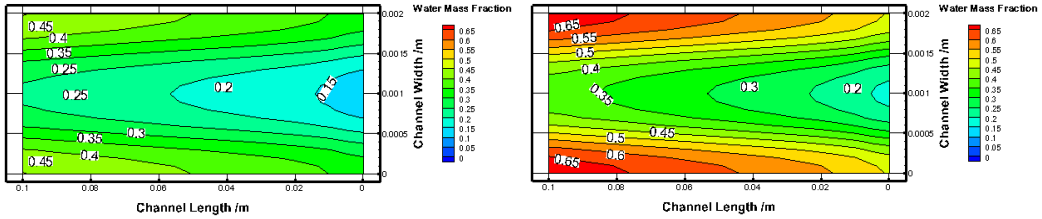

(d) Mezedur, Kaviany and Moore (2002)

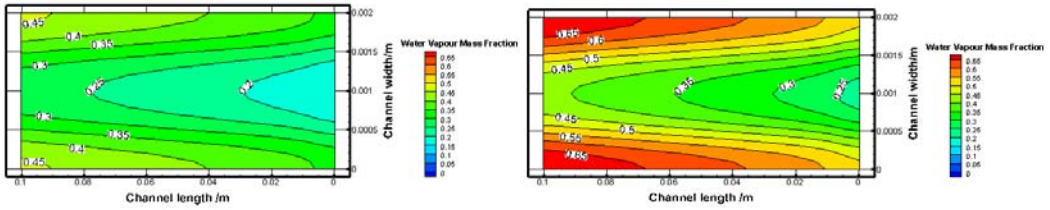

(e) Tomadakis and Storichos (1993)

Figure 5.5 Water vapour mass fraction distribution predicted by various effective diffusivity models at the catalyst/membrane interface for an average current density of 0.5 Acm^{-2} (left) and 1.0 Acm^{-2} (right) respectively.

This effect is more prominent at higher current density. A closer inspection of mass fraction of oxygen predicted by Tomadakis and Sotirchos (1993) model reveals much uniform oxygen distribution due to taking into account more realistic in-plane diffusion which is higher than the cross-plane diffusion.

Figure 5.5 shows the mass fraction of water vapour distribution predicted by various effective diffusivity models at the catalyst/membrane interface for average current density of 0.5 Acm^{-2} and 1.0 Acm^{-2} respectively. The predicted mass fraction of water vapour is higher under the land area compared to the channel area. There are large differences on the predicted peak values of water vapour among different diffusivity models particularly at average current density value of 1.0 Acm^{-2}. Dawes et al. (2009) and Neale and Nader (1973) models produce lower peak water vapour values compared to the Bruggeman model, whereas Mezedur, Kaviany and Moore (2002) and Tomadakis and Sotirchos (1993) produces higher water vapour level. The main implication of these finding is that any water management strategy developed based on Bruggeman correlation suggest inadequate water removal from the GDL.

5.3 Summary of the chapter

The diffusion of species through gas diffusion layer has been modelled using Bruggeman, Dawes et al. (2009), Neale and Nader (1973), Mezedur, Kaviany and Moore (2002), Tomadakis and Sotirchos (1993). Among these models, Tomadakis and Sotirchos (1993) is the only model which takes into account the anisotropy of GDL fibre distribution. Simulation results show that the effective diffusivity model has significant effects on the prediction of fuel cell characteristic. Dawes,

Neale and Nader models provide higher values of cell voltage compared to the Bruggeman model, while Mezedur, Kaviany and Moore model, Tomadakis and Sotirchos anisotropic model produces lower values of voltage compared to the Bruggeman model. Although Bruggeman correlation is being widely used in PEM fuel cell modelling, Tomadakis and Sotirchos anisotropic model produces cell voltage much closer to the experimental values and can be implemented in PEM fuel cell modelling to improve accurate cell performance prediction capability at high current density.

6

Chapter 6: Multi-Phase Model Results

It was observed using the single-phase model that the water vapour mass fraction increases along the channel due to the depletion of oxygen from the mixture. Most of the water accumulation was observed under the land area and in the gas diffusion layer of cathode and along the channel. This gives an idea about the potential regions where reactant transport becomes lower due to formation of liquid water. In these regions water vapour condenses to form liquid water droplets. The produced liquid water droplet blocks the pores and, hence cell performance is reduced due to limitations of fresh reactants reaching the catalyst layer. At higher current densities, a dried anode condition at the outlet was observed which leads to a higher ohmic overpotential and reduced the cell voltage. Therefore, a multiphase model would be beneficial to investigate the liquid water formation and reactants transport limitations in cathode GDL and CL at higher current densities. A multi-phase model based on water vapour to liquid phase change has been created and reactants distributions along the channel are presented in this chapter.

6.1 Model Validation

The condensation process of a PEM fuel cell is assumed to be governed by the partial pressure of vapor phase and temperature. However, Khan, Sundén, and Yuan (2011) have questioned the validity of this assumption and highlighted that slight difference in temperature could have significant effects, which supposes that several other unknown factors might influence the evaporation/condensation process. These unknown factors are taken into consideration through the condensation factor K_c in the simulation. Unfortunately, there has been no definite value for K_c and researchers have used very widely different values. The predicted fuel cell polarization curve of the multi-phase model for different condensation rate is shown in Figure.6.1. The simulation results are compared with single-phase simulation and experimental results by Ticianelli, Derouin, and Srinivasan (1988) to establish the accuracy of the simulated results. The multi-phase model simulation studies were carried out at two different condensation rates (K_c = 1.0 s^{-1} and 10.0 s^{-1}). Similar results are observed at current densities through the operating range compared to the single-phase model for condensation rate 1.0s^{-1}. Whereas, a better agreement was achieved by multi-phase model for condensation rate 10.0 s^{-1}. It was explained in earlier chapter that the single-phase model cannot illuminate the liquid water effect and excessive water flooding inside cathode on PEM fuel cell performance at higher current densities. The multi-phase model taken into consideration of liquid water formation effect, hence can demonstrate the exact situation at higher current densities.

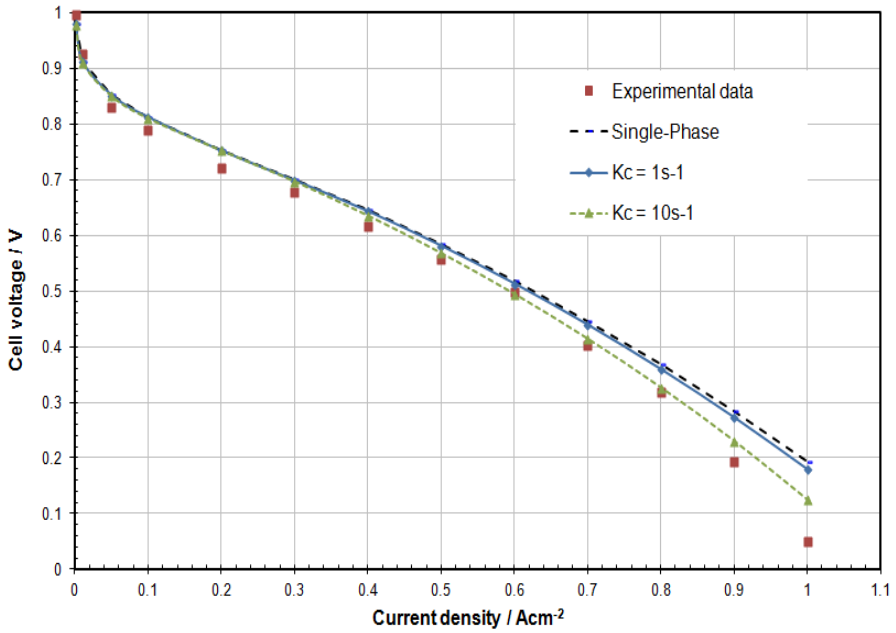

Figure 6.1 Comparison between the multi-phase model results and experiments (Ticianelli, Derouin, and Srinivasan 1988).

6.2 Liquid water formation inside cathode

The multi-phase models are used to investigate the liquid water production inside cathode at different current densities for condensation rate of 1.0 s^{-1}. Figure 6.2 shows the water vapour and water liquid mass fraction profiles at the average current density of 1.0 Acm^{-2}. It is observed from the figure that the water vapour mass fraction increases along the channel due to water produced by electrochemical reaction and water coming from anode side to cathode side by electro-osmotic process. Again, more water vapour is produced under land area because of low velocity of air under land allows more humidification of dry air. This water vapour condensed to produce liquid water droplet under the land area. Condensation depends on the partial pressure of water vapour and saturated water vapour pressure. At higher current densities, partial pressure of water vapour is higher

compared to saturated water vapour pressure and hence, more water vapour condense to form water droplet. At higher current densities, excess water vapour would produce inside the cell and low rate of water removal from the cell can cause formation of more liquid water droplet blocking the pores. Therefore, special attention is necessary to operate PEM fuel cells at higher current densities.

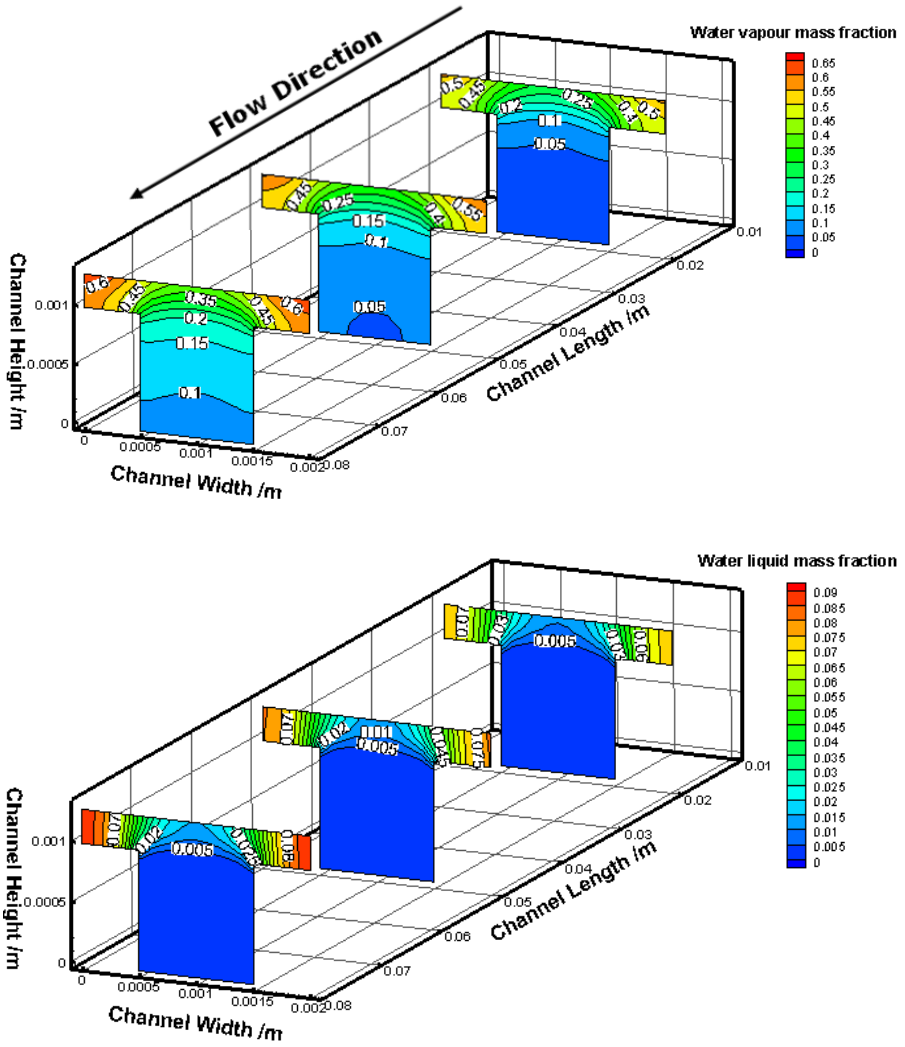

Figure 6.2 Water vapour (upper) and water liquid (lower) mass fraction contour plot at an average current density of I = 1.0 Acm^{-2}.

6.3 Effect of saturation function on cell performance

The effective diffusivity model considers the effect of porosity and saturation and is expressed as

$$D_k^{eff} = f(\epsilon)g(s)D_k \tag{6.1}$$

In previous chapter, the effects of different porosity models on PEM fuel cell performance were studied using single-phase model. Tomadakis and Sotirchos (1993) model has been shown to provide the best representation of species diffusivity and this percolation theory based diffusion model for random fibrous porous medium is given by

$$f(\varepsilon) = \varepsilon \left(\frac{\varepsilon-\varepsilon_p}{1-\varepsilon_p}\right)^{\alpha} \tag{6.2}$$

where ε_p is the percolation threshold and equal to 0.11. α is the empirical constant which depends on the direction. The value of α is 0.521 for in-plane and 0.785 for cross-plane diffusion. The effects of saturation on the effective diffusivity of species are generally given by power law model,

$$g(s) = (1-s)^m \tag{6.3}$$

Saturation, s, is defined as ratio of volume of liquid water present in each computational cell to the total volume of each cell (Dawes et al. 2009). Different scaling functions of water saturation were proposed by various authors. For example, Misra and Wu (2009) used a value of 3 and He, Yamazaki and Abudula (2010) used a value 2.5 and, whereas Jung et al. (2010) and Min (2010) used a value of 1.5. Nam and Kaviany (2003) have provided a detailed analysis of the effective gas diffusivity using a pore network model and shown that a combination of percolation based model for porosity effect and a power

law with an exponent of 2 for saturation has provided a good agreement with the results obtained from the pore network model. Dawes et al. (2009) have investigated the effective diffusivity effects and reported that the percolation based models for both porosity and saturation have provided a better agreement compared to the power law model with exponent of 1.5. A relative permeability model based on percolation theory to represent the effect of saturation was proposed by Dawes et al. (2009) and expressed as:

$$g(s) = \frac{\left((1-s)-0.11\right)^{0.9}}{(1-0.11)^{0.9}} \tag{6.4}$$

The effect of each saturation power law saturation model and percolation based model by Dawes et al. (2009) on effective diffusion models are investigated for different condensation rate and transport limitations at high current densities are summarized in the following sections.

6.3.1 Simulation studies for K_c =1.0 s^{-1}

The effects of saturation models on PEM fuel cell performance are summarized in Figure. 6.3. Saturation functions in the effective diffusivity model cause change in overall diffusion of species inside PEM cell. At higher current densities, small variation was observed compared to single-phase model. Six different saturation equations were implemented in the multi-phase model and simulation studies was performed to investigate their effect on overall cell performance. Although using multi-phase model is illustrating the liquid water formation, the effects of saturation functions were insignificant. This is due to low condensation rate which influence the amount of water vapour condensed to form liquid water inside cathode. A comprehensive investigation was carried out to investigate the

reactants transport inside cathode at high current density for different saturation functions.

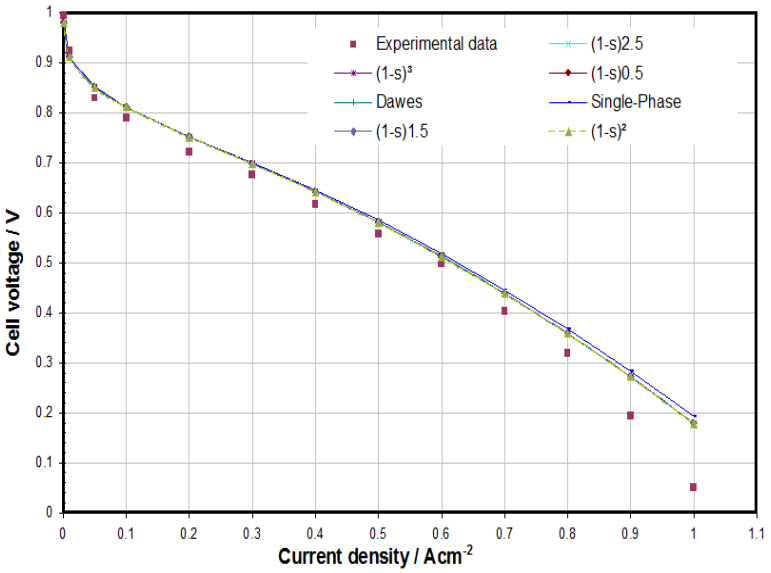

Figure 6.3 Polarization curve for different functions of saturation at K_c=1.0 s^{-1}.

Figure 6.4, 6.5 and 6.6 show the oxygen, water vapour and water liquid mass fraction respectively at an average current density of 1.0 Acm^{-2}. As there is no difference in cell voltage prediction was observed using different saturation model, only widely used three different functions of saturation were selected (m=1.5, 2.5 and percolation based saturation model). No change in reactant distribution was observed for different saturation functions. As condensation rate is very low, only a small fraction of water vapour was condensed to form liquid water. Therefore, water vapour fraction remains almost similar for different the saturation functions, which has no effect on liquid water transport inside cell and transport of reactants remain unchanged. It would be interesting to investigate the effect of saturation function for higher condensation rate of $10s^{-1}$.

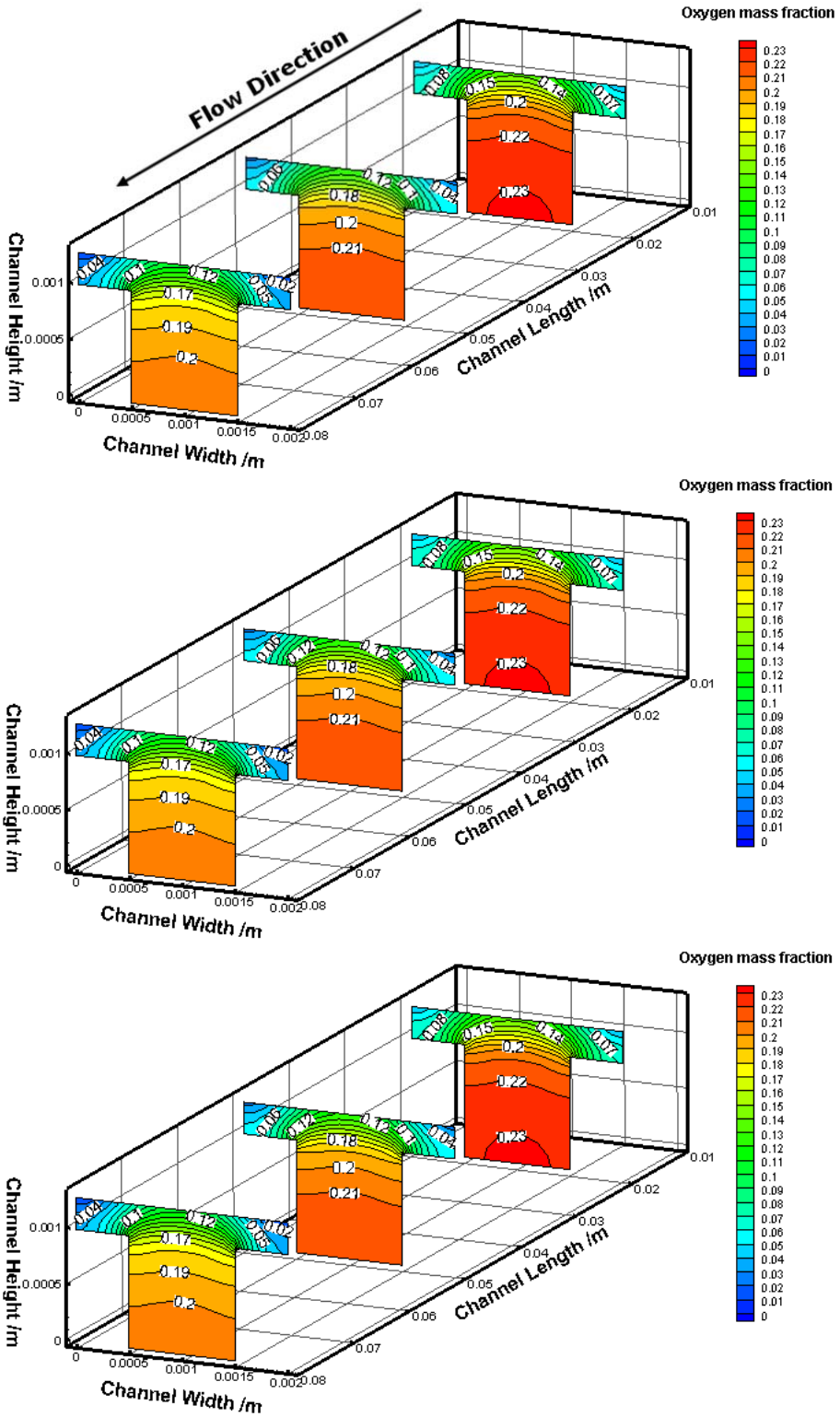

Figure 6.4 Oxygen mass fraction contour plots for different functions of saturation at K_c=1.0 s^{-1}: $(1-s)^{1.5}$ Upper, $(1-s)^{2.5}$ middle, Dawes et al. (2009) Model Lower.

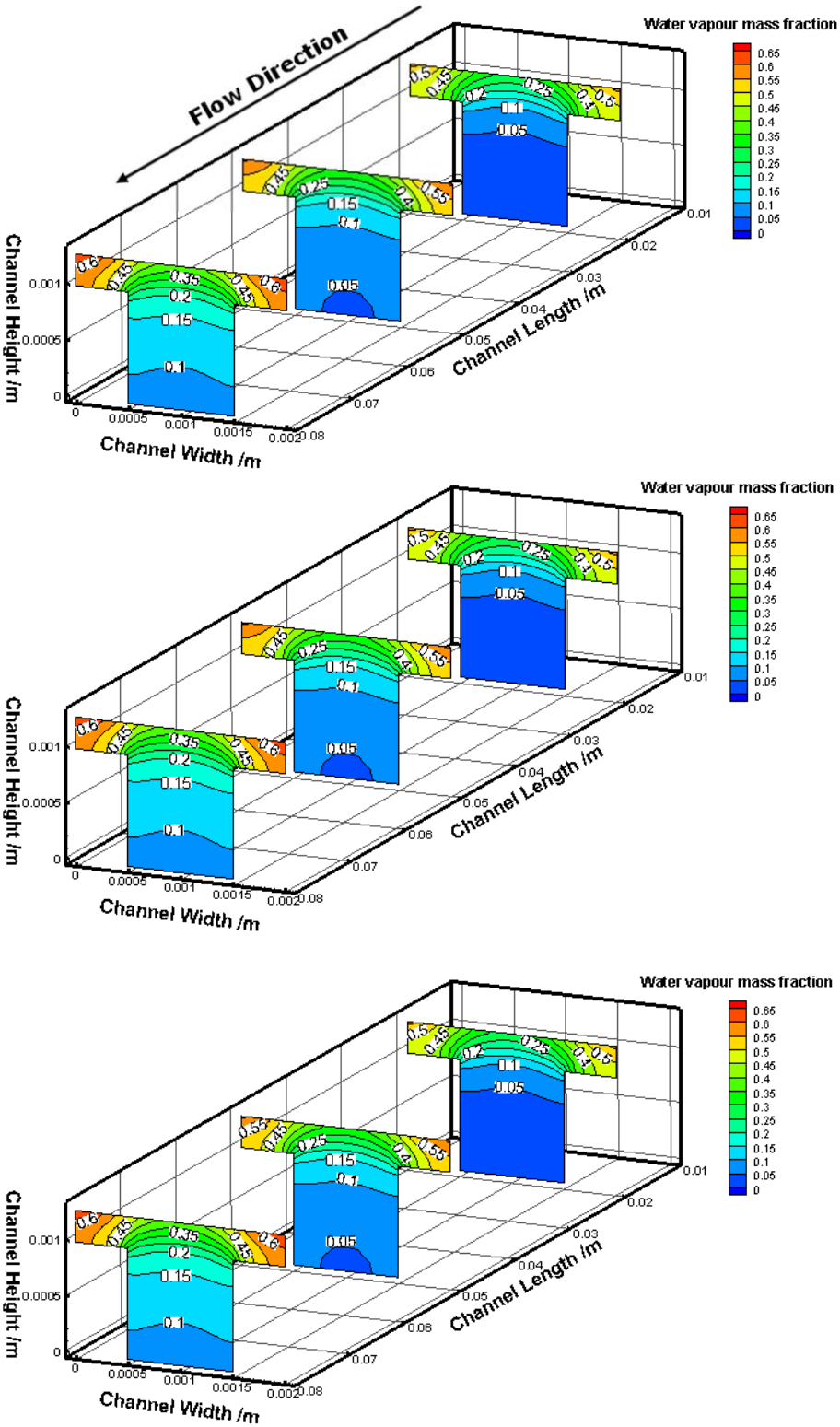

Figure 6.5 Water vapour mass fraction contour plots for different functions of saturation at K_c=1.0 s^{-1}: $(1-s)^{1.5}$ Upper, $(1-s)^{2.5}$ middle, Dawes et al. (2009) Model Lower.

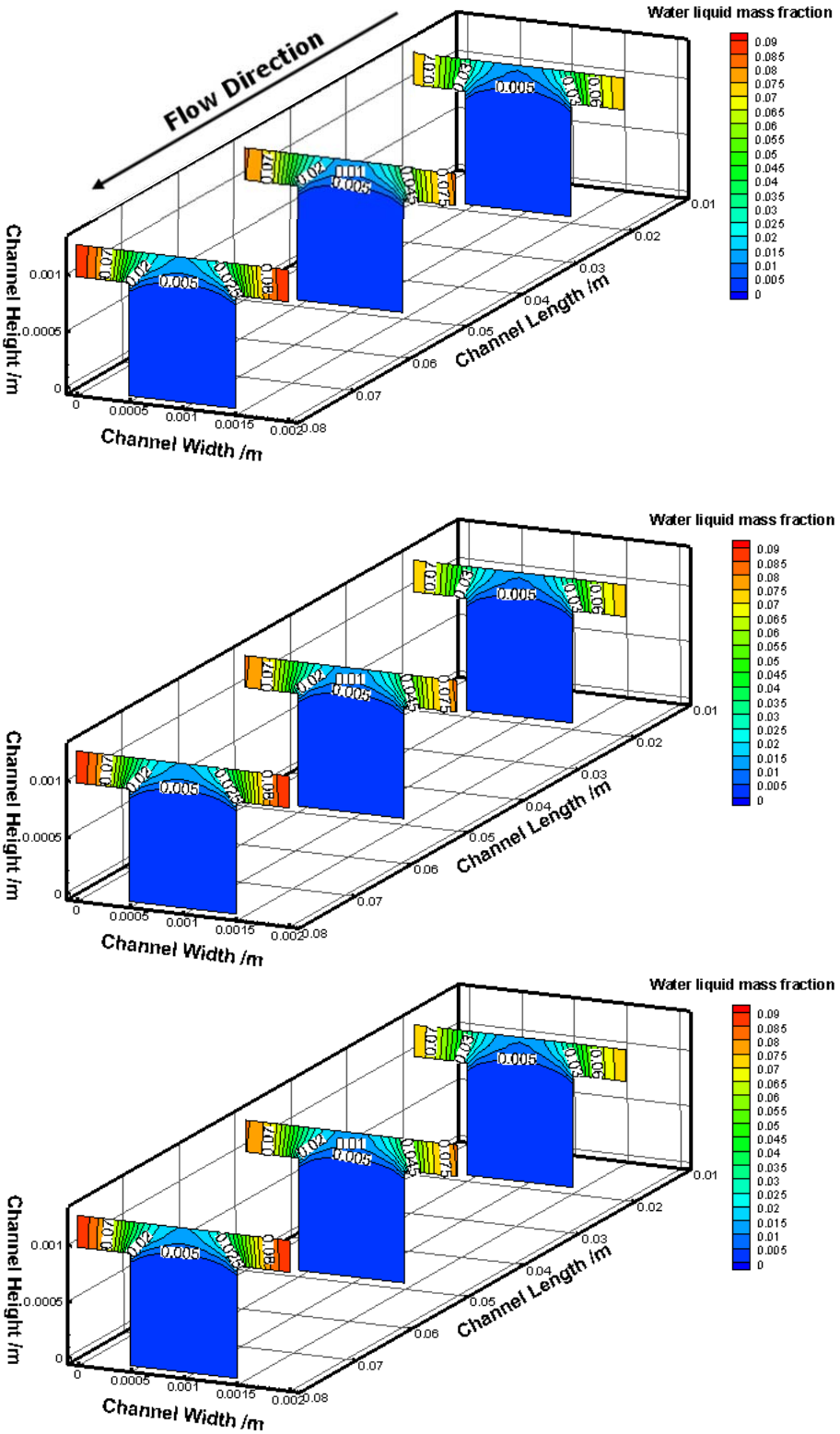

Figure 6.6 Water liquid mass fraction contour plots for different functions of saturation at K_c=1.0 s^{-1}: $(1-s)^{1.5}$ Upper, $(1-s)^{2.5}$ middle, Dawes et al. (2009) Model Lower.

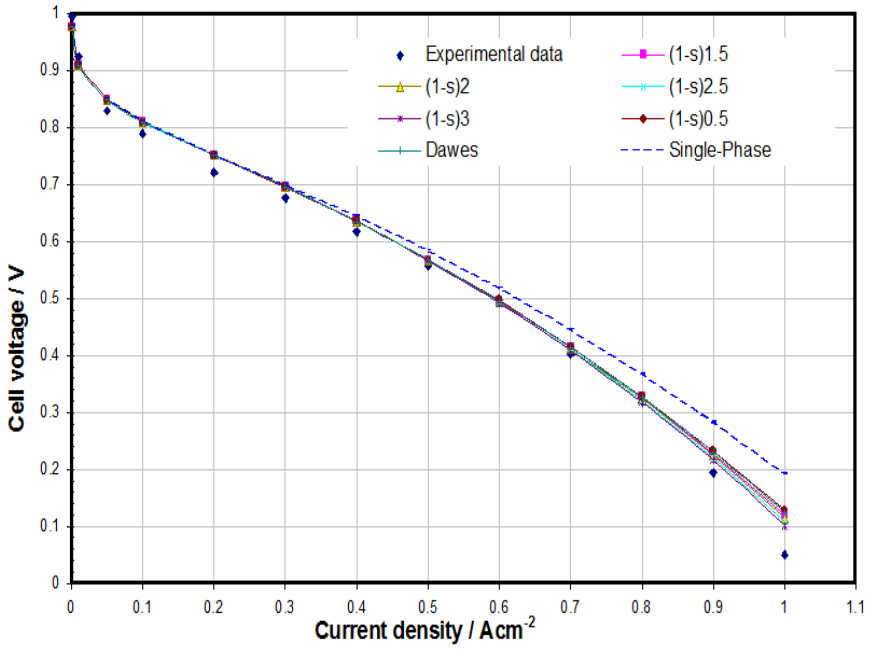

Figure 6.7 Polarization curve for different functions of saturation at K_c=10.0 s^{-1}.

6.3.2 Simulation studies for K_c =10.0 s^{-1}

The effect of saturation functions on PEM fuel cell performance for a condensation rate of 10s^{-1} is summarized in Figure. 6.7. The predicted simulation results using multi-phase models show better agreement and clear difference in cell performance was observed for higher current densities.

At low current densities, not so much deviation in results was observed. The effects of saturation functions were more prominent for high average current density of 1.0 Acm^{-2}. At higher current densities, excessive water vapour was observed inside cathode side. This influence the saturation and more liquid water form due to higher condensation rate. A detailed investigation was carried out to investigate the oxygen transport limitation due to production of liquid water inside cathode at different current densities (0.5 Acm^{-2} and 1.0

Acm^{-2}) for different saturation functions. Figure 6.8 shows the oxygen mass fraction contours for different saturation functions at 0.5 Acm^{-2}. Identical contour plots in the GDL and CL suggest that not so much difference at low current density. That's why the cell voltage remains unchanged for different saturation functions. While, clear difference is observed at higher current densities. At higher current densities, more water vapour condensed to form the liquid water and that blocks the pores in GDL and CL. This limits the fresh oxygen coming to CL. Figure 6.9 shows that oxygen transport limitation at cathode GDL and CL. The limitations mostly occur under the land area and downstream along the channel where most of the water vapor accumulates and turn to liquid water. The Dawes saturation model cannot illustrate the saturation effect and over predicting the amount of oxygen coming to CL compared to other models. Therefore, slightly higher voltage is predicted using this saturation model. This result highlights that the under land area is critical for water management and effective design or operating parameter should be found to remove this trapped liquid.

As the inclusion power law saturation model $(1-s)^{2.5}$ to two-phase flow modelling has significantly improved the prediction and brought the predicted cell voltage closer to the experimental data, this model is implemented for rest of parametric studies in following chapters.

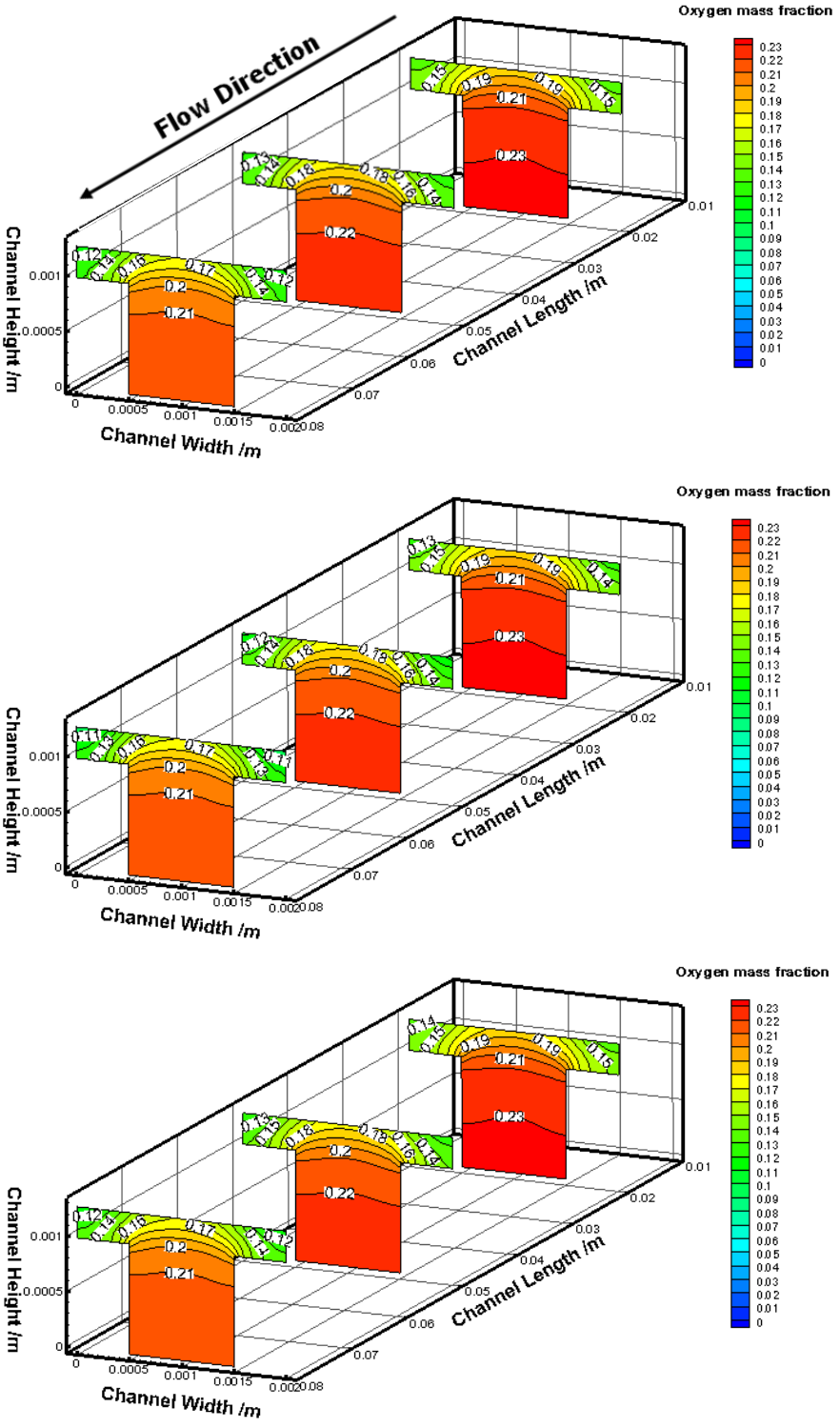

Figure 6.8 Oxygen mass fraction contour plots for different functions of saturation for a current density of 0.5 Acm^{-2} at K_c=10.0 s^{-1}: (1-s)$^{1.5}$ Upper, (1-s)$^{2.5}$ middle, Dawes et al. (2009) Model Lower.

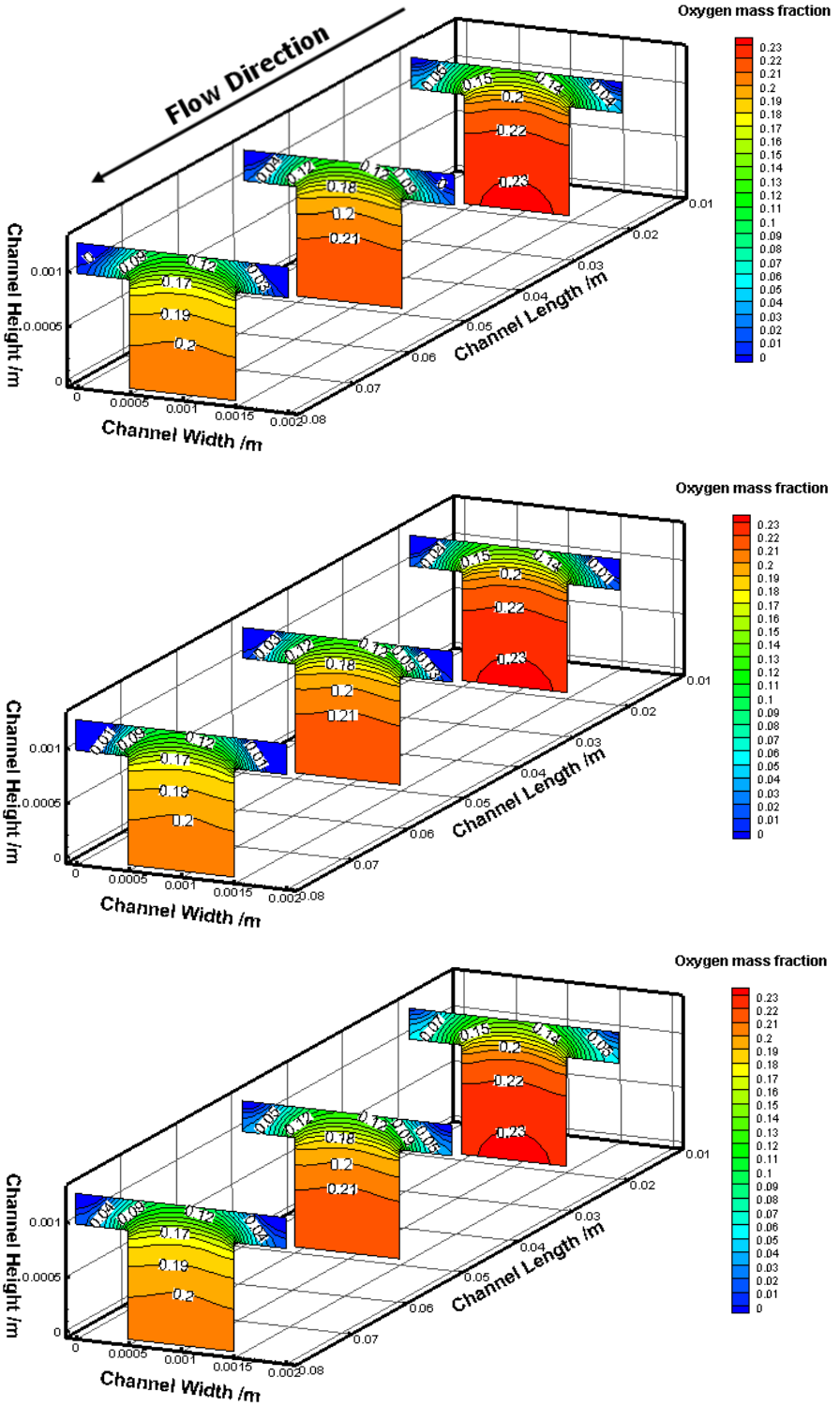

Figure 6.9 Oxygen mass fraction contour plots for different functions of saturation for a current density of 1.0 Acm^{-2} at K_c=10.0 s^{-1}: (1-s)$^{1.5}$ Upper, (1-s)$^{2.5}$ middle, Dawes et al. (2009) Model Lower.

6.4 Summary of Multi-Phase Results

A multi-phase model based on water vapour to liquid phase change is created and reactants distributions along the channel are presented in this chapter. liquid water droplets production was observed under the land area in cathode side at higher current density. The produced liquid water droplet blocks the pores and, hence cell performance is reduced due to limitations of fresh reactants reaching catalyst layer. The effect of condensation rate is explained and the model predicts better results for a value $10s^{-1}$. The effects of saturation functions are discussed and the influences are insignificant for lower condensation rate.

7

Chapter 7: Effect of GDL Permeability on Cell Performance- A parametric study

The permeability of gas diffusion layer is one of the key parameters that influence the PEM fuel cell performance. It was shown that the cell performance decreases for decreasing GDL permeability up to a certain range in the single-phase chapter. At lower current densities, the change in GDL permeability has no effect on cell performance. However, GDL permeability influences the cell at higher current densities. Lower permeability exhibits higher resistance to flow through porous medium. The effect of anisotropic GDL permeability on PEM fuel cell using multi-phase model is presented in this chapter.

7.1 Effect of Anisotropic GDL permeability of Gas Diffusion Layer

Literature review shows that different values of permeability of gas diffusion layer have been used in published modelling work. Such as, an isotropic permeability value of 1.76 x 10^{-11} has been widely used (Min 2010, Liu, Lou and Wen 2010, Jung, Lee and Chen 2012, Hu et al. 2004, Le and Zhou 2010) as well as 10^{-12} (Meng 2007b, Shimpalee and Van Zee 2007, Jeon et al. 2008) and 5 x 10^{-11} (Dawes et al. 2009) in computational modelling of PEM fuel cell. Dawes et al. (2009) performed a parametric study of permeability in the range of 1.5 x 10^{-8} to 1.5 x 10^{-12}. Gostick et al. (2006) measured through-plane and in-plane permeability of various commercially available gas diffusion layers to be in the range of 10^{-11} – 10^{-12}. Ahmed, Sung and Bae (2008) studied the effect of anisotropy in permeability numerically by setting various in-plane and through plane permeability combinations in the range of 1 x 10^{-9} to 1 x 10^{-15}. The study showed that the permeability had significant effects on water and thermal management especially at very low values of permeability. In Ahmed, Sung and Bae's (2008) study, the permeability values were arbitrarily set at an unrealistic low values and the analysis were done for single current density of 2.4 Acm^{-2}. This current density is unusually high. In contrary, Dawes et al. (2009) provided a parametric study of the effects of permeability on the cell performance. They showed that the effect of permeability became insignificant below a permeability of 5 x 10^{-11}.

In order to investigate the effects of GDL permeability on cell performance, simulations have been carried out for a range of permeability ($\mathbf{1 \times 10^{-8}}$ m^2 to $\mathbf{1 \times 10^{-12}}$ m^2). These values have been chosen as the most representative values of commonly used GDL in reported experimental and numerical studies. Table 7.1 shows the combinations of different case studies. C stand for case studies in the

Table. C11, C22 and C33 stand for isotropic permeability combinations. Similarly, C11, C12, C13, C21, C23, C31 and C32 stand for anisotropic permeability combinations. Though various combinations of permeability values have been simulated, Ahmed, Sung and Bae (2008) mentioned that the in-plane permeability of the GDLs is much higher than through-plane permeability in practice. Simulations have been performed to investigate the effect of permeability at average current density of 0.5 and 1.0 Acm^{-2}. The catalyst layer permeability has been fixed for the case studies at 1 x 10^{-10} m^2.

Table 7.1 Combinations of permeability for the model study.

In plane Permeability x-z direction	Through plane Permeability y direction		
	$1x10^{-8}$	**$1x10^{-10}$**	**$1x10^{-12}$**
$1x10^{-8}$	**C11**	**C12**	**C13**
$1x10^{-10}$	**C21**	**C22**	**C23**
$1x10^{-12}$	**C31**	**C32**	**C33**

Figure 7.1 shows vector plots at the mid plane of the assembly at different permeability cases (C11, C12, C13, C22, and C33). In these plots vector lengths are kept constant as the velocity varies widely among different zones. At high permeability case, the velocity direction is mainly longitudinal inside the GDL (C11) caused by high convective velocity in the flow channel. At low permeability cases however (C22 and C33) the direction of flow changes inside the GDL, and becomes perpendicular to the main flow directions. This is more evident in the

anode as the velocity in the anode channel is much lower than the cathode channel. In the case of anisotropic permeability (C12 and C13), the velocity vector plots are quite similar to C11 highlighting the effects of lower through plane permeability is negligible.

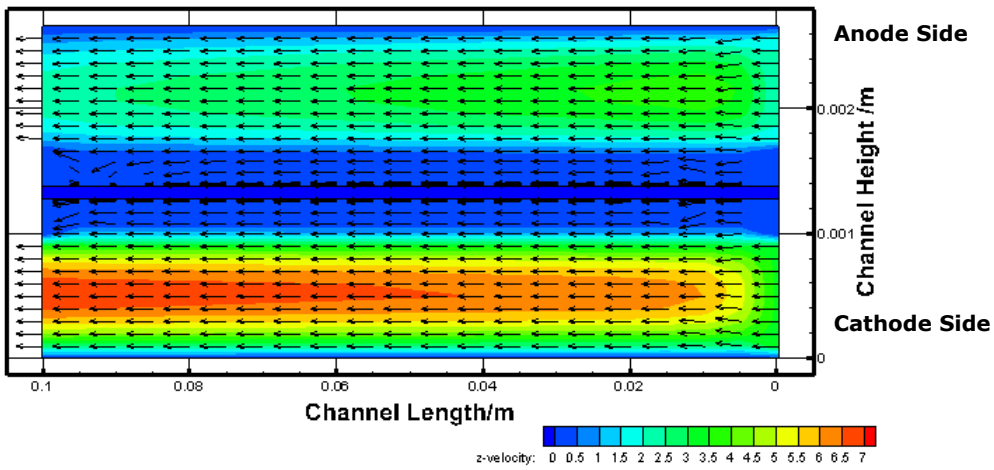

(a) C11

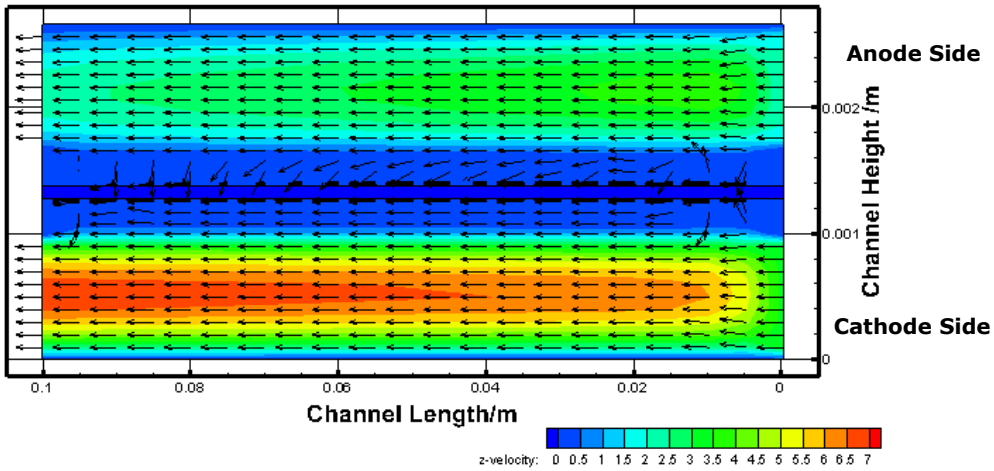

(b) C22

Figure 7.1 Velocity vector at mid plane for different permeability cases.

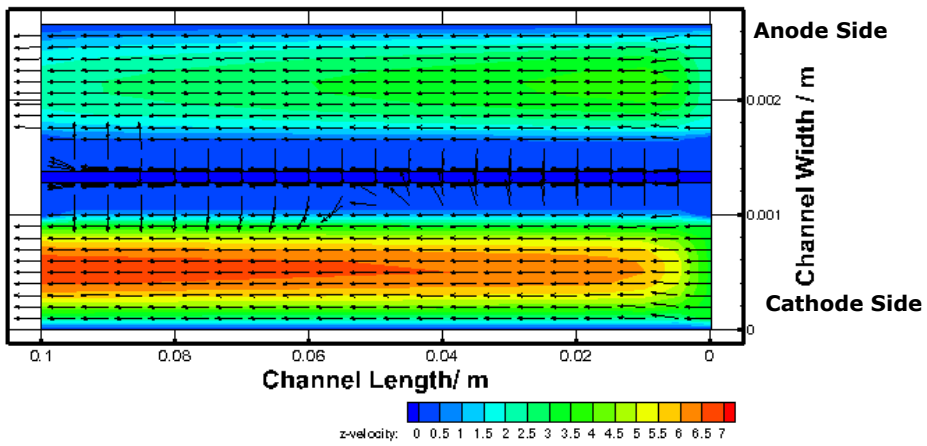

(c) C33

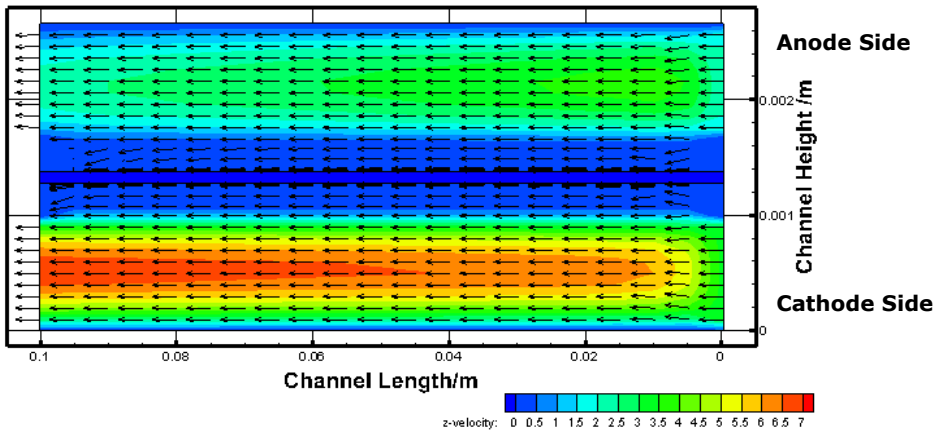

(d) C12

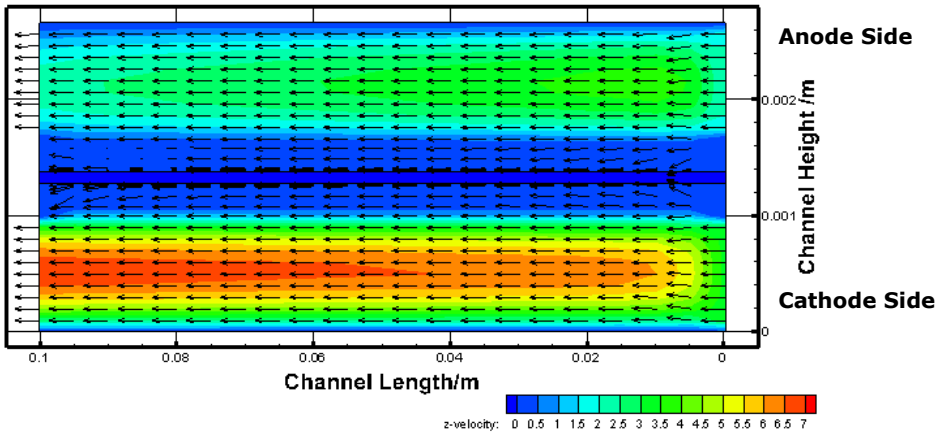

(e) C13

Figure 7.1: Velocity vector at mid plane for different permeability cases (Continued).

Table 7.2 Cell Voltage at isotropic and anisotropic permeability combination for an average current density of 0.5 Acm^{-2}.

Case Studies	Cell Voltage
C11	0.583
C22	0.571
C33	0.568
C12	0.584
C13	0.577
C21	0.571
C23	0.571
C31	0.568
C32	0.568

Table 7.3 Cell Voltage at isotropic and anisotropic permeability combinations for an average current density of 1.0 Acm^{-2}.

Case Studies	Cell Voltage
C11	0.206
C22	0.156
C33	0.026
C12	0.207
C13	0.190
C21	0.159
C23	0.148
C31	0.048
C32	0.052

Simulations have been carried out for 0.5 Acm^{-2} and 1.0 Acm^{-2} current densities and the calculated average cell voltages have been presented in Tables 7.2 and 7.3. The simulation studies show a very small change in cell voltage at low current density of 0.5 Acm^{-2} and effect of anisotropic or isotropic combinations are insignificant. However, large drop in cell voltage are observed at higher current density of 1.0Acm^{-2}. It is observed that cell voltage deteriorate for low isotropic permeability for average current density of 1.0 Acm^{-2}. C11 is the highest isotropic permeability combinations. By decreasing permeability in isotropic conditions, more restriction of flow is observed

in the GDL. Small number of reactants can pass to catalyst layer and less water are produced as a by-product of electro-chemical reactions. Hence, the cell voltage drops for lower isotropic permeability combinations. This result agrees with previous work by Ahmed, Sung and Bae (2008).

For anisotropic cases C11, C12, C13, where the in-plane permeability is kept fixed at $1X10^{-8}$, and the through plane permeability has been varied $1X10^{-8}$, $1X10^{-10}$ and $1X10^{-12}$, the effect is less significant with voltage dropping from 0.206 to 0.19. For the cases C11, C21, C31, where the through plane permeability is kept at a high value of $1X10^{-8}$, whereas the in-plane permeability is varied $1X10^{-8}$, $1X10^{-10}$, $1X10^{-12}$, the effect is rather significant with the voltage decreasing from 0.206 to 0.048. The implication of this is that either the permeability of GDL should be isotropic with high enough value or anisotropic with higher in-plane permeability. The anisotropic GDL with higher through-plane permeability and lower in-plane permeability would lead to the poor performance of fuel cell. This finding is in contrary to the findings of Ahmed, Sung and Bae (2008) who concluded that higher permeability in either in-plane or through-plane and a lower permeability in other direction would produce similar fuel cell performance. This contradiction is due to the results of using very low permeability values in Ahmed, Sung and Bae (2008) work. Again for C13 and C31 cases, the computed average cell voltages are 0.19 and 0.048 respectively, which clearly shows that the higher in-plane permeability compared to through plane permeability produces better cell performance.

A comprehensive simulation studies were performed to investigate this further by investigating the oxygen, water vapour and water liquid mass fraction at three different locations at cathode GDL/catalyst layer interface.

7.2 Isotropic permeability combinations

Mass fraction distributions of oxygen, water vapour and water liquid are considered at three different locations inside cathode for different isotropic conditions (C11, C22 and C33). The results are showed in the following figures from 7.2 to 7.4. Figure 7.2 shows a decrease in oxygen mass fraction along the channel for the isotropic conditions. At the inlet, a decrease in oxygen mass fraction is observed for low permeability combination. A significant reduction in oxygen mass fraction results from changing permeability combination C11 to C22. However, further reduction in permeability proved to be insignificant. At higher permeability, low restriction to flow was observed and more oxygen is accumulated under the land area. In addition at lower permeability, flow is more restricted and saturation is affecting the relative permeabilities of gas mixture. Similar decreasing trend demonstrate the low permeability effect at the middle of the channel and exit. A further reduction at the exit suggests more water vapour is produced which limits the fresh oxygen to reach catalyst layer. Figure 7.3 and 7.4 show the water vapour and water liquid mass fraction along the channel at GDL/CL interface for the isotropic conditions at a current density of 1.0 Acm^{-2}. The trend observed in oxygen mass fraction distribution is further investigated by investigating these figures. At higher current densities, more water is produced inside cell. In addition, more water is transferred from anode side and accumulated under the land due to lower velocities of gas mixture. That's why water vapour tends to increase along the length and remove oxygen from the GDL and CL. With decreasing permeabilities, water removal rate is so less that it condensed to form liquid water. The liquid water droplets block the pores in GDL and CL section. Although decreasing isotropic permeability combination show decrease of cell performance, the influence is insignificant below a permeability value of 10^{-12}.

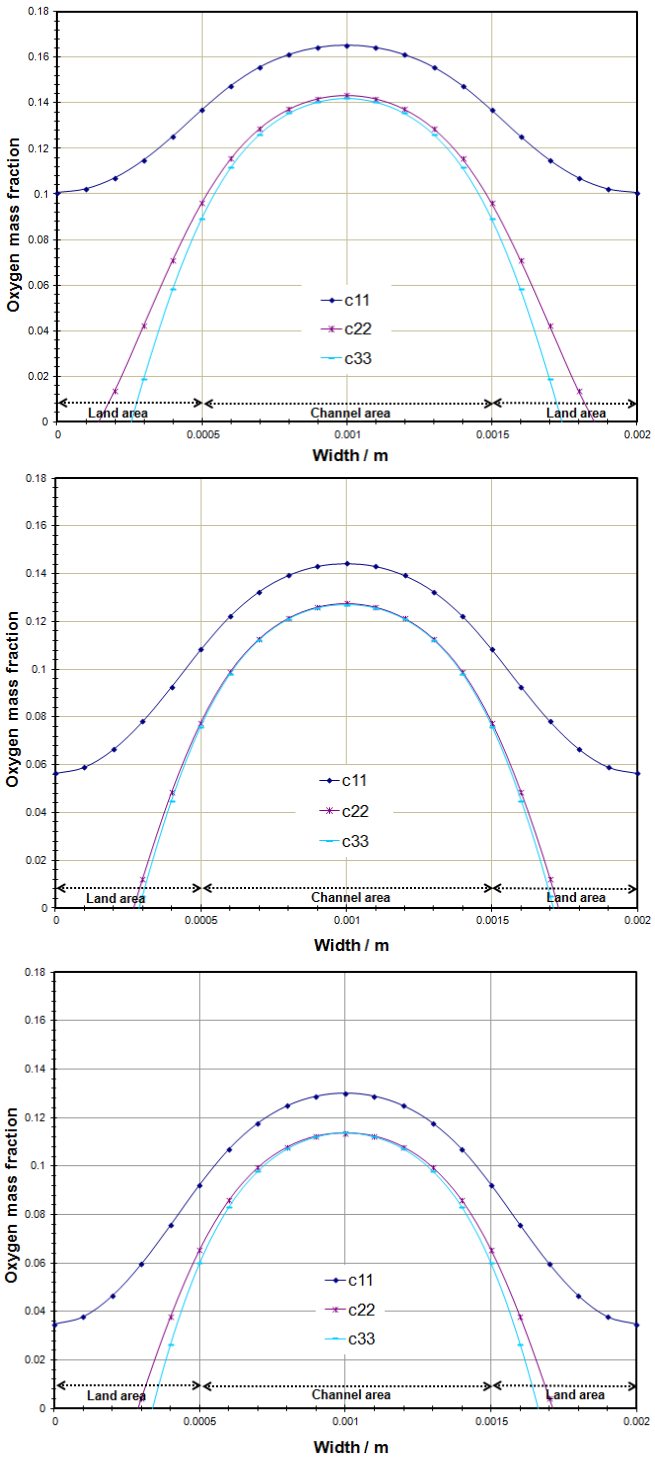

Figure 7.2 Distribution of oxygen mass fraction at the cathode GDL/CL interface for isotropic permeability study for an average current density of 1.0 Acm^{-2} (C11, C22, and C33): Channel Inlet (upper), Channel Middle (middle), Channel Exit (lower).

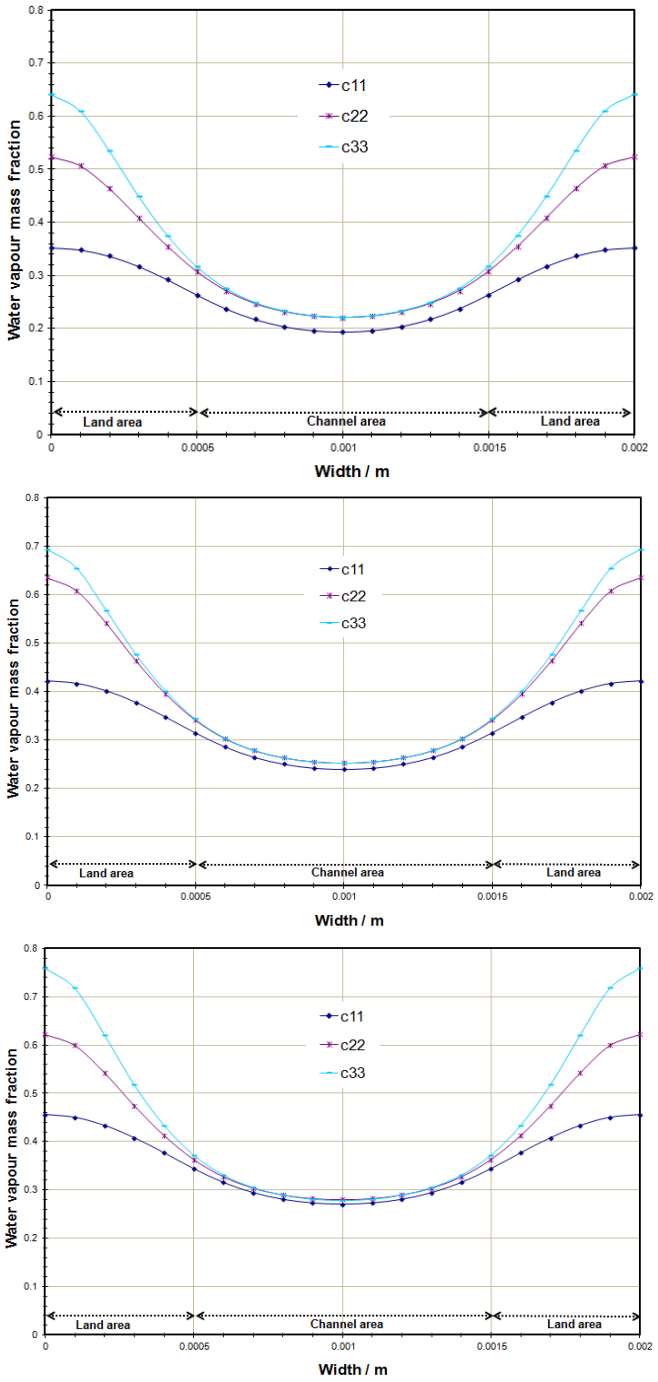

Figure 7.3 Distribution of water vapour mass fraction at the cathode GDL/CL interface for isotropic permeability study for an average current density of 1.0 Acm^{-2} (C11, C22, and C33): Channel Inlet (upper), Channel Middle (middle), Channel Exit (lower).

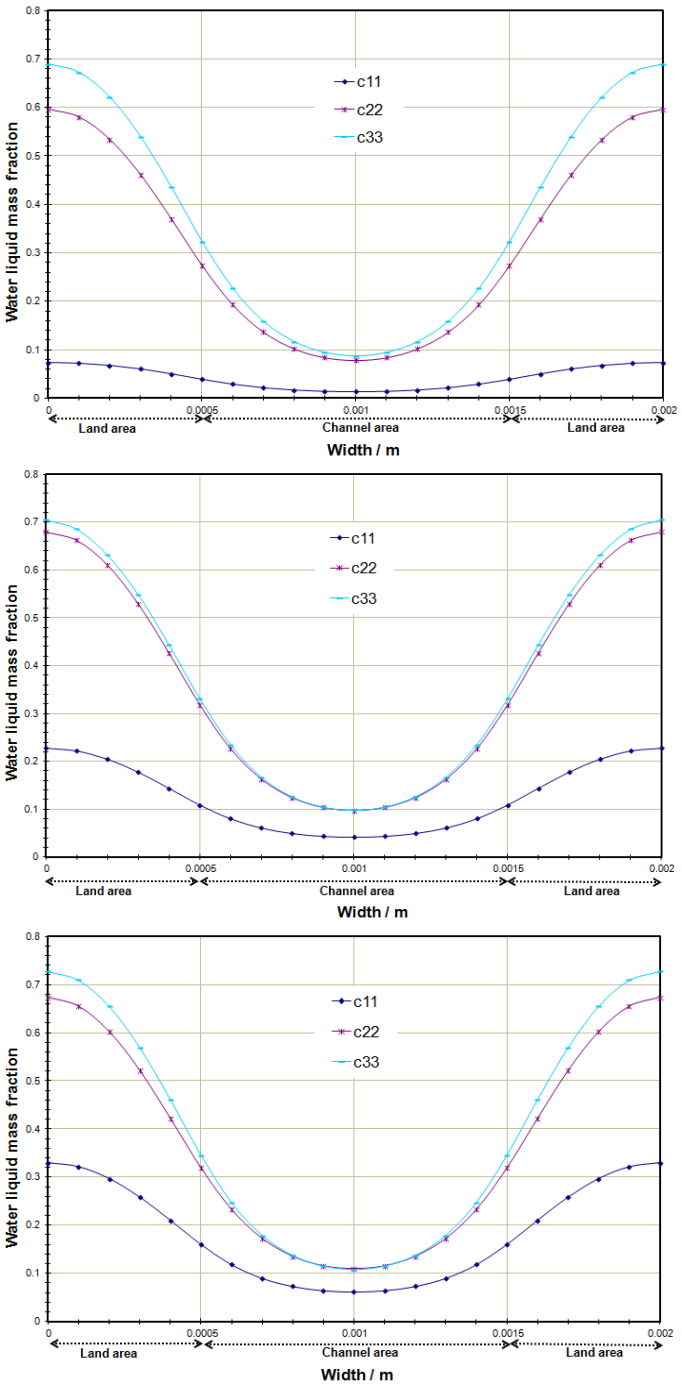

Figure 7.4 Distribution of water liquid mass fraction at the cathode GDL/CL interface for isotropic permeability study for an average current density of 1.0 Acm^{-2} (C11, C22, and C33): Channel Inlet (upper), Channel Middle (middle), Channel Exit (lower).

7.3 Anisotropic permeability combinations

Anisotropic permeability combinations are investigated to check the effect of in-plane and through-plane permeability on cell performance. Table 7.3 show that at high current densities, anisotropic permeability has major influence on cell performance. The anisotropic GDL with higher through-plane permeability and lower in-plane permeability would lead to the poor performance of fuel cell.

Case studies (C11, C12, and C13) are selected for examining the oxygen, water vapour and water liquid mass fraction distributions along the length of the channel at three different locations at GDL/CL interface and plotted in the figures 7.5 to 7.7. At the channel inlet, mass fraction of oxygen remains constant under the channel area for C11 to C13. Whereas, a small decrease in mass fraction was observed under the land area for C13. A significant variation in mass fraction is observed at the exit of the channel for C13. At lower through-plane permeability (less than value of 10^{-10}), the flow is increasingly restricted in through-plane direction. No significant variation was observed in the water vapour distribution at the inlet and middle of the channel. However, more water vapour at exit for case C13 suggests that water vapour remain trapped in the GDL/CL interface for higher restriction to flow.

A significant variation was found for liquid water for anisotropic permeability case C13. More liquid water is formed compared to other cases. Lower through-plane permeability exhibits higher restriction and trap the water vapour under the land. The trapped water vapour formed water droplets under the land area. Therefore, a higher mass fraction for liquid water in noticed inside the channel for case C13.

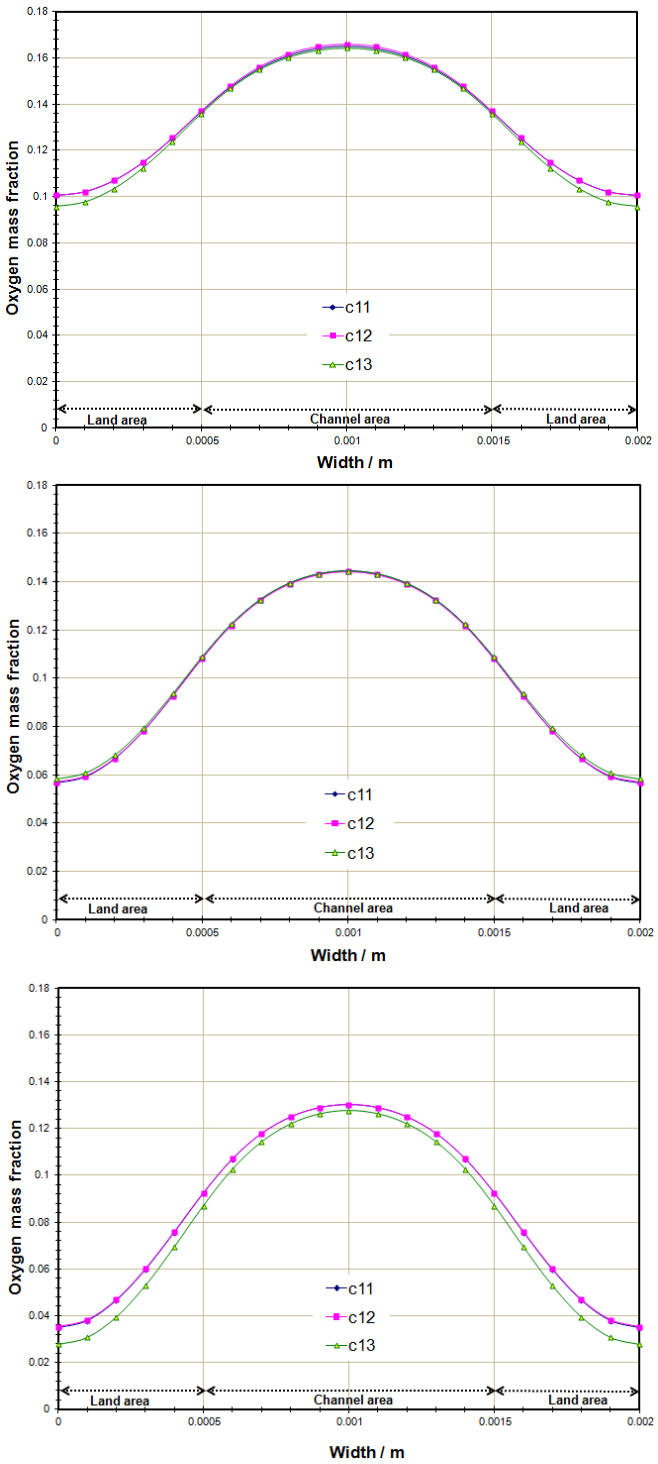

Figure 7.5 Distribution of oxygen mass fraction at the cathode GDL/CL interface for anisotropic permeability study for an average current density of 1.0 Acm^{-2} (C11, C12, and C13): Channel Inlet (upper), Channel Middle (middle), Channel Exit (lower).

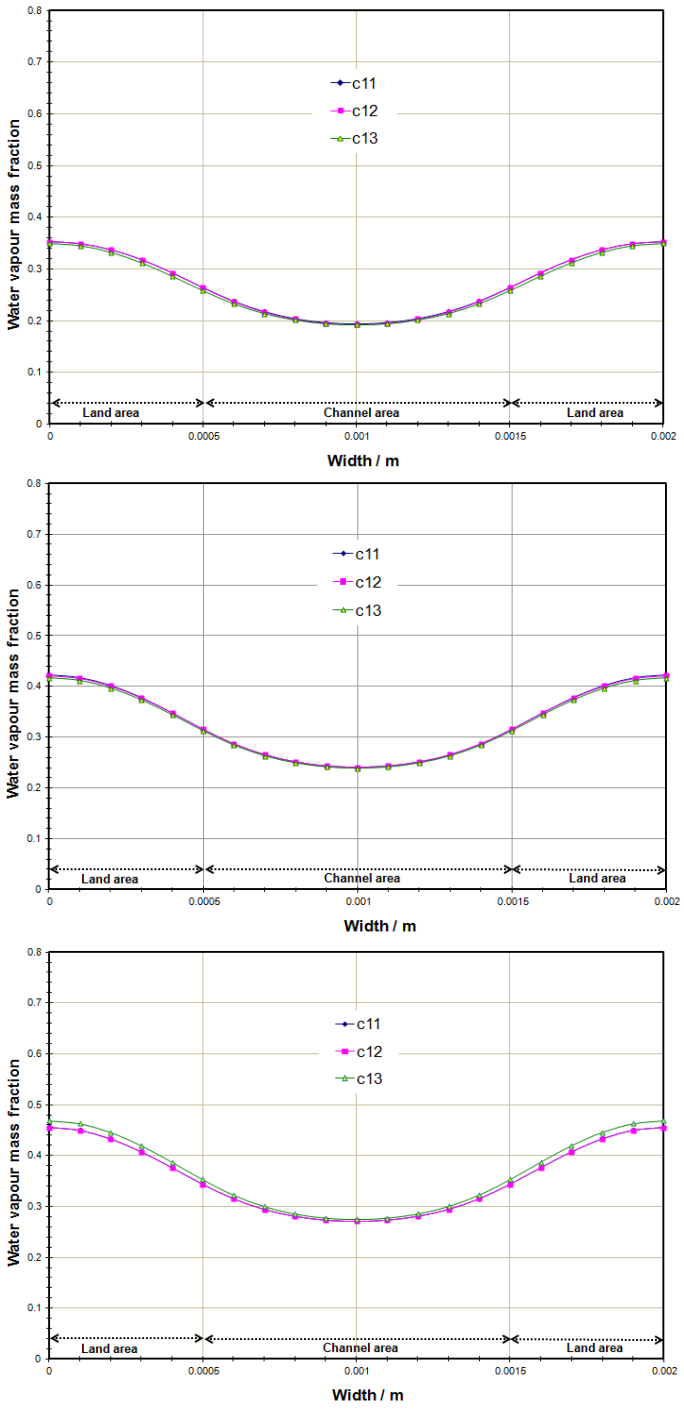

Figure 7.6 Distribution of water vapour mass fraction at the cathode GDL/CL interface for anisotropic permeability study for an average current density of 1.0 Acm^{-2} (C11, C12, and C13): Channel Inlet (upper), Channel Middle (middle), Channel Exit (lower).

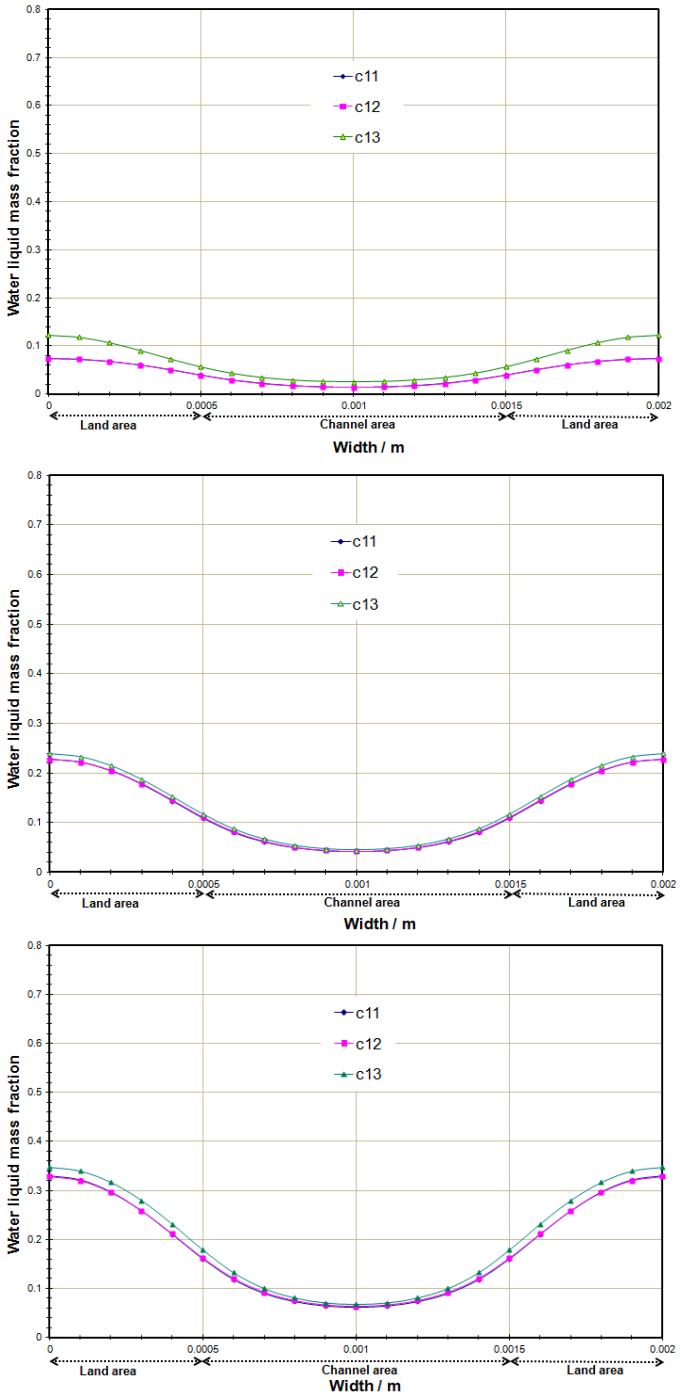

Figure 7.7 Distribution of water liquid mass fraction at the cathode GDL/CL interface for anisotropic permeability study for an average current density of 1.0 Acm^{-2} (C11, C12, and C13): Channel Inlet (upper), Channel Middle (middle), Channel Exit (lower).

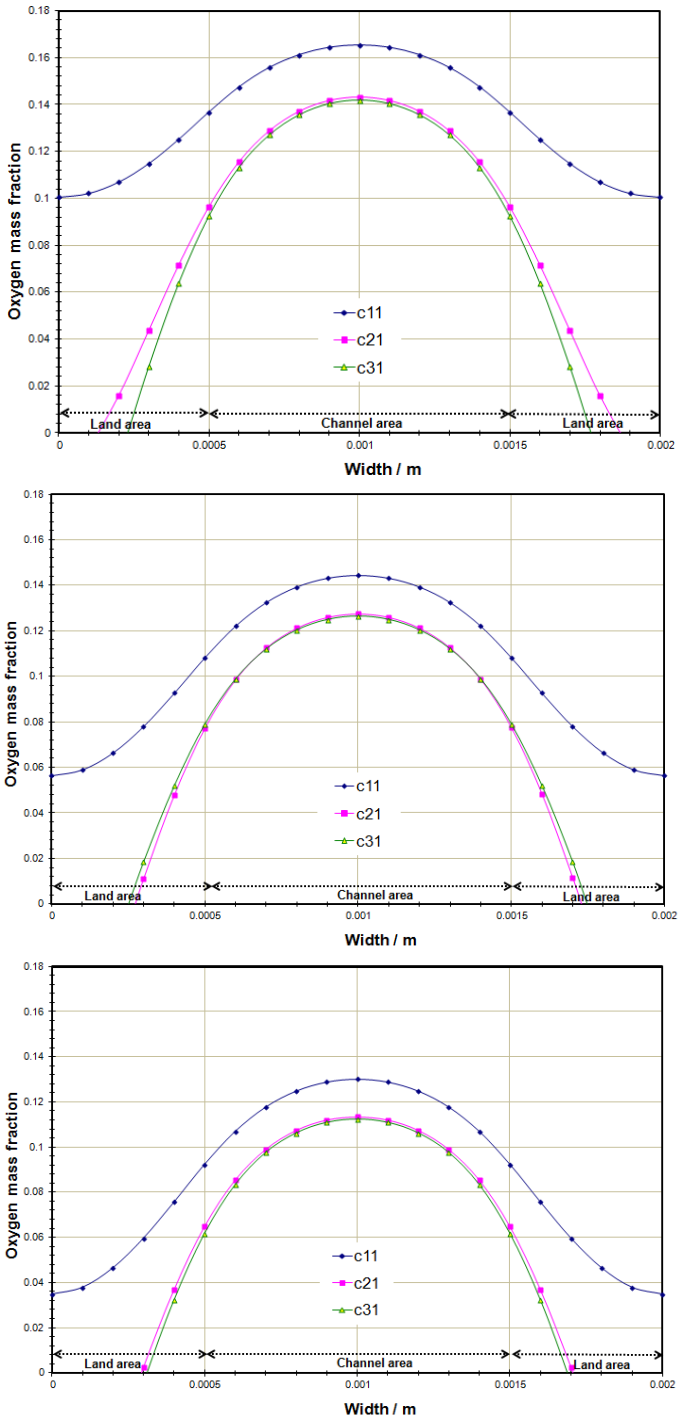

Figure 7.8 Distribution of oxygen mass fraction at the cathode GDL/CL interface for anisotropic permeability study for an average current density of 1.0 Acm^{-2} (C11, C21, and C31): Channel Inlet (upper), Channel Middle (middle), Channel Exit (lower).

Further insights into the effects of permeability are gained from the profiles of mass fraction of oxygen at the catalyst/GDL interface at three different locations as shown in Figures 7.8. In Figure 7.8, the profile of mass fraction of oxygen shows two distinct groupings. For C11, adequate oxygen is available under the land area, but C21 and C31 cases, no oxygen is available under the land area. There are two possible reasons behind this: (i) less amount of oxygen is diffusing due to low in-plane permeability and (ii) more importantly the presence of liquid water blocking the fresh oxygen to reach the reaction sites. Water removal rate is very good for the case of C11, C12, C13 with less amount of water (both liquid and vapour form) is present under the land area as shown in Figures 7.6 and 7.7. As a result, C11, C12 and C13 cases are the most efficient. This is also evidenced from in the cell voltage values given in Table 7.2.

7.4 Summary of the Chapter

The effects of anisotropic and isotropic permeability have been investigated and the simulated results show that in order to get higher fuel cell performance, the permeability of gas diffusion layer has to be high in both in-plane and through-plane directions. The higher in-plane and lower through plane permeability also produces good fuel cell performance. On the other hand, higher through-plane and lower in-plane permeability produces poor fuel cell performance. As this investigation shows, this performance deterioration arises from inadequate water removal under the land area. The results show that higher performance of a PEM fuel cell is achieved by optimizing the permeability of gas diffusion layers.

8

Chapter 8: Conclusion and Future Work

A comprehensive three-dimensional, isothermal, steady-state, straight channel PEM fuel cell model was developed to investigate the transport limitations of fresh reactants at high current densities. Computational fluid dynamics (CFD) techniques were implemented to investigate complex interactions of different electrochemical processes and transport phenomena under steady state conditions for various operating conditions and design parameters. Simulation predicted cell performances for different average current densities are validated with experimental results and optimum design parameters are obtained based on parametric studies. Uncertainty of modelling accuracy related to effective diffusivity models and effect of anisotropic permeability are studied.

8.1 Achievements

A steady state, single-phase, three-dimensional PEM fuel cell model was developed in the first phase of PhD studies. The single-phase model considered the existing models (Min 2010, Mazumder and Cole 2003 and Liu, Lou and Wen 2010). and improves the existing PEM fuel cell models to predict reactants transport limitations at higher current densities using there-dimensional framework. A user defined function (UDF) code was developed considering source terms for porous zones, effective diffusivity models for species transport inside cells and electrochemistry algorithm to predict cell voltage at an average current density. Water transport through membrane was implemented considering electro-osmotic drag and back diffusion inside PEM fuel cell. Volume averaged concentration at the anode and cathode side was used to approximate the water concentration gradient across membrane. The UDF code is interpreted by commercial CFD solver ANSYS Fluent 12.0. The single-phase model was validated against experimental results and used to investigate the species distribution at higher average current densities. Parametric studies were performed to determine the optimal operating and geometrical design of PEM fuel cell. Increasing stoichiometric flow ratio from 2.0 to 5.0 shows improved fuel cell performance at higher current densities. GDL permeability has no effect on cell performance for a value lower than 10^{-11}. GDL porosity is one of the major design parameters which have significant influence on limiting current density, hence on cell performance. A GDL porosity value between 0.4 to 0.6 shows improved cell performance over the entire operating range. Decreasing land area width for a fixed channel width shows improved performance. Low membrane thickness provides higher cell performance and approximately 50% reduction in membrane thickness results approximately 100% improvement in cell performance at high current density of 1.0 Acm^{-2}.

Most of the previous PEM fuel cell models used Bruggeman correlation for explaining the diffusion of species though porous GDL and CL, but this thesis considered other types of effective diffusion models and investigated the effect of diffusion models on cell performance at high current densities. The diffusion of species through gas diffusion layer has been modelled using Bruggeman, Dawes et al. (2009), Neale and Nader (1973), Mezedur, Kaviany and Moore (2002), Tomadakis and Sotirchos (1993). Among these models, Tomadakis and Sotirchos (1993) is the only model which takes into account the anisotropy of GDL fibre distribution. Simulation results show that the effective diffusivity model has significant effects on the prediction of fuel cell characteristic. Dawes et al., Neale and Nader models provide higher values of cell voltage compared to the Bruggeman model, while Mezedur, Kaviany and Moore model, Tomadakis and Sotirchos anisotropic model produces lower values of voltage compared to the Bruggeman model. Tomadakis and Sotirchos anisotropic model produces cell voltage much closer to the experimental values. Therefore, anisotropic diffusion model should be utilized in PEM fuel cell modelling to minimize modelling uncertainties.

A two-phase flow, steady-state, three-dimensional PEM fuel cell model to take into account liquid/water vapour phase change was developed in the last phase of the PhD. Flooding inside the cell was captured at high current density using the model and close to experimental results was obtained for condensation value of 10.0 s^{-1}. Finally, parametric studies were performed based on isotropic and anisotropic GDL permeability cases. Higher in-plane and lower through-plane permeability produces good fuel cell performance. On the other hand, higher through-plane and lower in-plane permeability produces poor fuel cell performance. Modelling results suggest that isotropic permeability cases have strong influence on cell performance

compared to anisotropic cases and can be utilized for cell performance improvement at high current density.

8.2 Future Work

A comprehensive PEM fuel cell model was developed to provide improved fundamental understanding of species transport in the porous zones and identified the best effective diffusion model for accurate modelling. However, further improvements in the model need to be considered in order to perform simulation studies at high temperature. The following improvements can lead towards developing a better PEM fuel cell model for the proposed future works:

- implementations of energy equations in the porous regions;
- effect of model parameters in PEM fuel cell modeling;
- mass transfer rate of water from liquid phase to vapour phase;

Lists of possible future works using the present model are summarized below:

- **Dynamic modelling of PEM fuel cells**

The dynamic transport of liquid water in the PEM fuel cell is very important to understand the transient behaviour of the fuel cell during start-up, shut down and load change. Frequent pressure fluctuations generate in the channels during dynamic conditions. Therefore, it is important to investigate the effect of pressure fluctuations on fuel cell performance. A two-phase, dynamic model provides better understanding of the dynamic operating behaviour of a PEM fuel cell. Most of the dynamic models available in literature investigated the current density variation with step change in voltage. Also the models

identified the under-shoot and over-shoot characteristics and transport limitations for different operating conditions. But a small number of those actually look into details of water management issues and possible solution to improve cell performance. Therefore, a three dimensional non-isothermal two-phase flow dynamic PEM fuel cell model is essential to understand the water management issue during different transient operating conditions.

- **Effect of flow channel geometry on cell performance**

According to the published numerical research, it was found that flow field designs affect the mass transport to and from catalyst layers and water removal in PEM fuel cell. In addition, serpentine flow field configurations can be used to minimize water flooding. Narrow channel with wider shoulder width configuration gives higher cell performance for stationary conditions. Comparative studies can be performed based on different flow channel geometry (stepped, tapered, serpentine, wavy, triangular, etc.) using the developed PEM fuel cell model.

Flow-field design showed strong influence on steady-state water management issue and considered to be as one of the crucial parameters. Still this parameter was not been investigated for dynamic conditions in details. Investigation of the flow-field effect on water management in PEM fuel cell using dynamic model can be a suitable future work and a novel flow-field design can be proposed for maximizing fuel cell performance under dynamic loading.

- **Effects of micro-porous layer in PEM fuel cells**

According to the previous experimental research, it was found that using micro-porous layer in cathode side of PEM fuel cell improves the cell performance. Numerical models can be developed considering

micro-porous layers at anode and cathode side. Investigations can be carried out at different operating conditions such as current density, temperature and different relative humidity at cathode and anode sides. The effects of porosity and thickness of micro-porous layer on PEM fuel cell performance can be investigated using the developed using the developed PEM fuel cell model.

References

AHMED, D. H. and SUNG, H. J., 2006. Effects of channel geometrical configuration and shoulder width on PEMFC performance at high current density. *Journal of Power Sources*, 162, pp. 327–339.

AHMED, D. H. and SUNG, H. J., 2007. Local current density and water management in PEMFCs. *International Journal of Heat and Mass Transfer*, 50, pp. 3376-3389.

AHMED, D. H., SUNG, H. J., BAE, J. and LEE, D. R., 2008. Reactants flow behavior and water management for different current densities in PEMFC. *International Journal of Heat and Mass Transfer*, 51, pp. 2006–2019.

AHMED D. H., SUNG H. J. and BAE, J., 2008. Effect of GDL permeability on water and thermal management in PEMFCs – I. isotropic and anisotropic permeability. *International Journal of Hydrogen Energy*, 33, pp. 3767-3785.

AL-BAGHDADI, M. A. R. S. and AL-JANABI, H. A. K. S., 2007 a. Parametric and optimization study of a PEM fuel cell performance using three-dimensional computational fluid dynamics model. *Renewable Energy*, 32 (7), pp. 1077-1101.

AL-BAGHDADI, M. A. R. S. and AL-JANABI, H. A. K. S., 2007 b. Optimization study of a PEM fuel cell performance using 3-D multi-phase computational fluid dynamics model. *Journal of Zhejiang University Science A*, 8(2), pp. 285-300.

AL-BAGHDADI, M. A. R. S. and AL-JANABI, H. A. K. S., 2007 c. Modeling optimizes PEM fuel cell performance using three-dimensional multi-phase computational fluid dynamics model. *Energy Conversion and Management*, 48, pp. 3102-3119.

ANSYS FLUENT 12.0 UDF Manual, 2010.

BARBIR, F., 2007. PEM Fuel cells. In: L. SAMMES, ed. *Fuel Cell Technology: Reaching Towards Commercialization*. Springer, Germany, pp. 27-51.

BERNING, T. and DJILALI, N., 2003. Three-dimensional computational analysis of transport phenomena in a PEM fuel cell – a parametric study. *Journal of Power sources*, 124, pp. 440-452.

BERNING, T., 2008. A three-dimensional, two-fluid model of PEM fuel cell cathodes. *ECS Transactions*, 16(2), pp. 23-34.

CARCADEA, E., ENE, H., INGHAM, D. B., LAZAR, R., MA, L., POURKASHANIAN, M. and STEFANESCU, I., 2007. A computational fluid dynamics analysis of a PEM fuel cell system for power generation.

International Journal of Numerical Methods for Heat and Fluid Flow, 17(3), pp. 302-312

CHEN, F., SU, Y. G., SOONG, C. Y., YAN, W. M. and CHU, H. S., 2004. Transient behavior of water transport in the membrane of a PEM fuel cell. *Journal of Electroanalytical Chemistry*, 566, pp. 85–93.

DAWES, J. E., HANSPAL, N. S., FAMILY, O. A. and TURAN, A., 2009. Three-dimensional CFD modelling of PEM fuel cells: An investigation into the effects of water flooding. *Chemical Engineering Science*, 64, pp. 2781 – 2794.

DOKKAR, B., SETTOU, N. E., IMINE, O., SAIFI, N., NEGROU, B. and NEMOUCHI, Z., 2011. Simulation of species transport and water management in PEM fuel cells. *International Journal of Hydrogen Energy*, 36, pp. 4220-4227.

DONG, Q., MENCH, M. M., CLEGHORN, S., and BEUSCHER, U., 2005. Distributed Performance of Polymer Electrolyte Fuel Cells under Low-Humidity Conditions. *Journal of Electrochemical Society*, 152, pp. A2114-A2122.

DUTTA, S., SHIMPALEE, S. and VAN ZEE, J.W., 2000. Three-dimensional numerical simulation of straight channel PEM fuel cells. *Journal of Applied Electrochemistry*, 30, pp. 135-146.

DUTTA, S., SHIMPALEE, S. and VAN ZEE, J.W., 2001. Numerical prediction of mass-exchange between cathode and anode channels in a PEM fuel cell. *International Journal of Heat and Mass Transfer*, 44 (11), pp. 2029–2042.

GOSTICK, J. T., FOWLER, M. W., PRITZKER, M. D., IOANNIDIS, M. A. and BEHRA, L. M., 2006. In-plane and through-plane gas permeability of carbon fiber electrode backing layers. *Journal of Power Sources*, 162, pp. 228-238.

GU, W.B. and WANG, C.Y., 2000. Thermal–electrochemical modeling of battery systems. *Journal of Electrochemical Society*, 147, pp. 2910–2922.

GURAU V., LIU, H. and KAKAC, S., 1998. Two dimensional model for proton exchange membrane fuel cells. *AIChE Journal*, 44 (11), pp. 2410- 2422.

HASHEMI, F., ROWSHANZAMIR, S. and REZAKAZEMI, M., 2012. CFD simulations of PEM fuel cell performance: Effect of straight and serpentine flow fields. *Mathematical and Computer modelling*, 55, pp. 1540-1557.

HE, G., YAMAZAKI, Y. and ABUDULA A., 2010. A three-dimensional analysis of the effect of anisotropic gas diffusion layer (GDL) thermal conductivity on the heat transfer and two-phase behavior in a proton exchange membrane fuel cell (PEMFC). *Journal of Power Sources*, 195 (6), pp. 1551-1560.

HU, M., GU, A., WANG, M., ZHU, X. and YU, L., 2004. Three dimensional, two phase flow mathematical model for PEM fuel cell: Part I. Model development. *Energy Conversion and Management*, 45, pp. 1861-1882.

HU, G. and FAN, J., 2006. A three-dimensional, multicomponent, two-phase model for a proton exchange membrane fuel cell with straight channel. *Energy & Fuels*, 20, pp. 738- 747.

INAMUDDIN, CHEEMA, T. A., ZAIDI, S.M.J. and RAHMAN, S.U., 2011. Three dimensional numerical investigations for the effects of gas diffusion layer on PEM fuel cell performance. Renewable energy, 36, pp. 529-535

INTERNATIONAL ENERGY AGENCY, 2010. *World energy outlook 2010*, France. Available from: www.worldenergyoutlook.org [Accessed 1st August, 2011]

JEON, D.H., GREENWAY, S., SHIMPALEE, S. and VAN ZEE, J. W., 2008. The effect of serpentine flow-field designs on PEM fuel cell performance. *International Journal of Hydrogen Energy*, 33 (3), pp. 1052-1066

JU, H., MENG, H. and WANG, C. Y., 2005. A single-phase, non-isothermal model for PEM fuel cells. *International Journal of Heat and Mass Transfer*, 48, pp. 1303–1315.

JU, H., WANG, C. Y., CLEGHORN, S. and BEUSCHER, U., 2005. Nonisothermal modelling of polymer electrolyte fuel cells I. Experimental Validation. *Journal of Electrochemical Society*, 152 (8), pp. A1645-A1653.

JUNG, C. Y., PARK, C. H., LEE, Y. M., KIM, W. J. and YI, S. C., 2010. Numerical analysis of catalyst agglomerates and liquid water transport in proton exchange membrane fuel cells. *International Journal of Hydrogen Energy*, 35(16), pp. 8433-8445.

JUNG, S. P., LEE, C. I. and CHEN, C. C., 2012. An efficient method for numerical predictions of the performance characteristics of fuel cells. I. Model development and validation. *Journal of Power Sources*, 199, pp. 179-194.

KARIMI, G., JAFARPOURA, F. and LI, X., 2009. Characterization of flooding and two-phase flow in polymer electrolyte membrane fuel cell stacks. *Journal of Power Sources*, 187, pp. 156–164.

KARNIK , A. Y., STEFANOPOULOU, A. G. and Sun, J., 2007. Water equilibria and management using a two-volume model of a polymer electrolyte fuel cell. *Journal of Power Sources*, 164, pp. 590–605.

KHAN, M. A., SUNDÉN, B. and YUAN, J., 2011. Analysis of multi-phase transport phenomena with catalyst reactions in polymer electrolyte membrane fuel cells – A review. *Journal of Power Sources*, 196(19), pp. 7899-7916.

KIM, J., LEE, S. M., SRINIVASAN, S. and Chamberlin, C. E., 1995. Modelling of proton exchange membrane fuel cell performance with an empirical equation. *Journal of Electrochemical Society*, 142(8), pp. 2670–2674.

LARMINIE, J. and DICKS, A., 2003. *Fuel Cell Systems Explained.* 2nd ed. John Wiley & Sons Ltd, England, pp. 75-79.

LE, A. D. and ZHOU, B., 2010. A numerical investigation on multi-phase transport phenomena in a proton exchange membrane fuel cell stack. *Journal of power sources*, 195, pp. 5278-5291

LIU, X., TAO, W., LI, Z. and HE, Y., 2006. Three-dimensional transport model of PEM fuel cell with straight flow channels. *Journal of Power Sources*, 158, pp. 25-35.

LIU, X., LOU, G. and WEN, Z., 2010. Three-dimensional two-phase flow model of proton exchange membrane fuel cell with parallel gas distributors. *Journal of Power Sources*, 195, pp. 2764-2773.

LUM, K. W., 2003. *Three-dimensional computational modelling of a polymer electrolyte membrane fuel cell*, Thesis submitted in partial fulfillment for the award of Degree of Doctor of Philosophy of Loughborough University, UK, Unpublished.

LUM, K. W. and MCGUIRK, J. J., 2005. Three-dimensional model of a complete polymer electrolyte membrane fuel cell-model formulation, validation and parametric studies. *Journal of Power Sources*, 143, pp. 103–124.

MATAMOROS, L. and BRUGGEMANN, D., 2006. Simulation of the water and heat management in proton exchange membrane fuel cells. *Journal of Power Sources*, 161, pp. 203–213.

MAZUMDER, S. and COLE, J. V., 2003. Rigorous 3-D mathematical modelling of PEM fuel cells I. Model prediction without liquid water transport. *Journal of Electrochemical Society*, 150(11), pp. A1503-A1509.

MENG, H., 2006. A three-dimensional PEM fuel cell model with consistent treatment of water transport in MEA. *Journal of Power Sources*, 162, pp. 426–435.

MENG, H., 2007a. A three-dimensional mixed-domain PEM fuel cell model with fully-coupled transport phenomena. *Journal of Power Sources*, 164, pp. 688–696.

MENG, H., 2007b. A two-phase non-isothermal mixed-domain PEM fuel cell model and its application to two-dimensional simulations. *Journal of Power Sources*, 168, pp. 218–228.

MENG, H. and WANG, C.Y., 2005. Model of two-phase flow and flooding dynamics in polymer electrolyte fuel cells. *Journal of Electrochemical Society*, 152(9), pp. A1733-A1741.

MEZEDUR, M., KAVIANY, M. and MOORE, W., 2002. Effect of pore structure, randomness sand size on effective mass diffusivity. *AIChE Journal*, 48, pp. 15–24.

MIN, C. H., 2009. Performance of a proton exchange membrane fuel cell with stepped flow field design. *Journal of Power Sources*, 186, pp. 370-376.

Min, C.H., 2010. A novel three-dimensional, two-phase and non-isothermal numerical model for proton exchange membrane fuel cell. *Journal of power sources*, 195, pp. 1880-1887.

MISHRA, B. and WU, J., 2009. Study of the effects of various parameters on the transient current density at polymer electrolyte membrane fuel cell start-up. *Renewable Energy*, 34 (10), pp. 2296-2307.

NAM, J. H. and KAVIANY, M. , 2003. Effective diffusivity and water-saturation distribution in single- and two-layer PEMFC diffusion medium. *International Journal of Heat and Mass Transfer*, 46, pp. 4595-4611.

NEALE, G. H. and NADER, W. K., 1973. Prediction of transport processes within porous media - diffusive flow processes within an

homogeneous swarm of spherical-particles. *AIChE Journal*, 19, pp. 112–119.

NGUYEN, T.V. and WHITE, R. E., 1993. A water and heat management model for proton exchange membrane fuel cells. Journal of Electrochemical society, 140(8), pp. 2178-2186

NGUYEN, P. T., BERNING, T. and DJILALI, N., 2004. Computational model of a PEMFC with serpentine gas flow channels. *Journal of Power Sources*, 130, pp. 149-157.

OBUT, S. and ALPER, E., 2011. Numerical assessment of dependence of polymer electrolyte membrane fuel cell performance on cathode catalyst layer parameters. *Journal of Power sources*, 196, pp. 1920-1931.

PENG, J. and LEE, S. J., 2006. Numerical simulation of proton exchange membrane fuel cells at high operating temperature. *Journal of Power Sources*, 162, pp. 1182–1191.

PHAROAH, J. G., KARAN, K. and SUN, W., 2006. On effective coefficients in PEM fuel cell electrodes: anisotropy of the porous transport layers. *Journal of Power Sources*, 161, pp. 214-224.

POTTER, M.J., 1999. *Parametric analysis of a solid polymer fuel cell using current distribution mapping*, Thesis submitted in partial fulfillment for the award of Degree of Doctor of Philosophy of Loughborough University, UK, Unpublished.

RISMANCHI, B. and AKBARI, M.H., 2008. Performance prediction of proton exchange membrane fuel cells using three-dimensional model. *International Journal of Hydrogen Energy*, 33, pp. 439-448.

SCHWARZ, D. H. and DJILALI, N, 2007. 3D Modelling of catalyst layers in PEM fuel cells. *Journal of Electrochemical Society*, 154(11), pp. B1167-B1178

SINGH, D., LU, D. M. and DJILALI, N., 1999. A two dimensional analysis of mass transport in proton exchange membrane fuel cells. *International Journal of Engineering Science*, 37, pp. 431-452.

SIVERTSEN, B. R. and DJILALI, N., 2005. CFD-based modeling of proton-exchange membrane fuel cells. *Journal of Power Sources*, 141(1), pp. 65-78.

SHIMPALEE, S. and ZEE, J.W.V., 2007. Numerical studies on rib & channel dimension of flow-field on PEMFC performance. *International Journal of Hydrogen Energy*, 32, pp. 842-856.

SHIMPALEE, S., DUTTA, S., LEE, W. K. and VAN ZEE, J. W., 1999. Effect of humidity on PEM fuel ceil performance Part II: Numerical simulation. *Proceedings of ASME IMECE, HTD,* 14-19 November 1999. Nashville, TN, 364 (1), pp. 367–374.

SPIEGEL, C., 2008. *PEM fuel Cell Modeling and Simulation using MATLAB ®.* Elsevier Inc., USA, pp. 1-14.

SPRINGER, T. E., ZAWODZINSKI, T. A. and GOTTESFELD, S., 1991. Polymer electrolyte fuel cell model. *Journal of Electrochemical Society*, 138 (8), pp. 2334–2342.

TICIANELLI, E. A., DEROUIN, C.R. and SRINIVASAN, S., 1988. Localization of platinum in low catalyst loading electrodes to attain

high power densities in SPE fuel cells. *Journal of Electroanalytical Chemistry*, 251, pp. 275-295.

TOMADAKIS, M. M. and SOTIRCHOS, S. V., 1993. Ordinary and transition regime diffusion in random fiber structures. *AIChE Journal*, 39, pp. 397–412.

UM, S., WANG, C.Y. and CHEN, K.S., 2000. Computational fluid dynamics modeling of proton exchange membrane fuel cells. *Journal of Electrochemical. Society*, 147, pp. 4485–4493.

UM, S. and WANG, C. Y., 2004. Three-dimensional analysis of transport and electrochemical reactions in polymer electrolyte fuel cells. *Journal of Power Sources*, 125, pp. 40-51.

U.S. DEPARTMENT OF ENERGY, Fuel Cell Technologies Program, 2011. [online]. Available from: http://www1.eere.energy.gov/hydrogenandfuelcells/fuelcells/pdfs/fc_comparison_chart.pdf [Accessed 15 January 2012]

VERSTEEG, H. K. and MALALASAKERA, W., 2007. *An Introduction to Computational Fluid Dynamics: The Finite-Volume Method*. 2nd ed. Pearson Education Limited, England.

WANG, L. HUSAR, A. ZHIU, T. and LIU, H., 2003, A parametric study of PEM fuel cell performances. *International Journal of Hydrogen Energy*, 28, pp. 1263-1272.

WORLD WIND ENERGY ASSOCIATION, 2011. [online] Available from: http://www.wwindea.org/home/index.php?option=com_content&task=blogcategory&id=21&Itemid=43 [Accessed 20 December 2011]

YI, J. S., and NGUYEN, Y. V., 1998. An along the channel model for proton exchange membrane fuel cells. *Journal of Electrochemical Society*, 145(4), pp. 1149-1159.

YOU, L. and LIU, H., 2002. A two-phase flow and transport model for the cathode of PEM fuel cells. *International Journal of Heat and Mass Transfer*, 45, pp. 2277–2287.

YU, L. J., REN, G. P., QIN, M. J. and JIANG, X. M., 2009. Transport mechanisms and performance simulations of a PEM fuel cell with interdigitated flow field. *Renewable Energy*, 34, pp. 530-543.

YUAN, J., SUNDEN, B., HOU, M. and ZHANG, H., 2004. Three-dimensional analysis of two-phase flow and its effects on cell performance of PEMFC. *Numerical Heat Transfer*, *Part A*, 46, pp. 669-694.

YUAN, W., TANG, Y., PAN, M., LI, Z. and TANG, B., 2010. Model prediction of effects of operating parameters on proton exchange membrane fuel cell performance. *Renewable Energy*, 35, pp. 656-666.

ZIEGLER, C., 2005. *Modeling and simulation of the dynamic behavior of portable proton exchange membrane fuel cells*, Thesis submitted in partial fulfillment for the award of Degree of Doktors der Naturwissenschaften (Dr. rer. nat.) of University of Konstanz, Germany. Available from: http://kops.ub.uni-konstanz.de/bitstream/handle/urn:nbn:de:bsz:352-opus-17126/ZieglerC.pdf?sequence=1

ZONG, Y., ZHOU, B. and SOBIESIAK, A., 2006. Water and thermal management in a single PEM fuel cell with non-uniform stack temperature. *Journal of Power Sources*, 161, pp. 143–159.

ZHOU, B., HUANG, W., ZONG, Y. and SOBIESIAK, A. 2006. Water and pressure effects on a single PEM fuel cell. *Journal of Power Sources*, 155, pp. 190–202.

Appendix A: UDF Code

```
/************************************************************************/
/************************************************************************/
/* PEM fuel cell User Define Functions Code                             */
/* Sheikh Zahidul Islam, Robert Gordon University                       */
/* Single-Phase Model steady state straight channel                     */
/* Version 2011 a.10                                                    */
/* Analysis: Effect of diffusion models                                 */
/* Reference: ANSYS FLUENT 12.0 UDF Manual                              */
/************************************************************************/
/************************************************************************/
/************************************************************************/
/************************************************************************/


/* Reactants in anode and cathode side                                  */
/* User defined Scalars                                                 */
/* Scalar 1: C_UDSI(c,t,0) = Oxygen mass fraction                       */
/* Scalar 2: C_UDSI(c,t,1) = Water vapour mass fraction                 */
/* Scalar 3: C_UDSI(c,t,2) = Hydrogen mass fraction                     */
/* Scalar 4: C_UDSI(c,t,3) = Nitrogen mass fraction                     */
/* Scalar 5: C_UDSI(c,t,4) = Average current density                    */
```

```
#include "udf.h"


/*********************************************************************/
/* UDF for specifying velocity at cathode and anode inlet            */
/*********************************************************************/


DEFINE_PROFILE(cathode_velocity,t,i)
{
  cell_t c;
  real x[ND_ND];
  real zeta = 5.0;
  real I_ref = 10000;
  real F = 96485.3;
  real R =8.314;
  real P = 101325.0;
  real x_o2 = 0.21;
  real Am = 2 * 100;
  real Ach = 1*1;

  begin_c_loop(c,t)
    {
      C_CENTROID(x,c,t);
      F_PROFILE(c,t,i) = (zeta * I_ref * R * C_T(c,t) * Am )/ (4 * F * P * Ach * x_o2);
     }
  end_c_loop(c,t)
}



DEFINE_PROFILE(anode_velocity,t,i)
{
  cell_t c;
  real x[ND_ND];
  real zeta = 5.0;
  real I_ref = 10000;
  real F = 96485.3;
  real R =8.314;
  real P = 101325.0;
  real x_h2 = 0.69;
  real Am = 2 * 100;
  real Ach = 1*1;

  begin_c_loop(c,t)
    {
      C_CENTROID(x,c,t);
      F_PROFILE(c,t,i) = (zeta * I_ref * R * C_T(c,t) * Am )/ (2 * F * P * Ach * x_h2);
     }
  end_c_loop(c,t)
}
```

```
/************************************************************************/
/* UDF for specifying density and viscosity                             */
/************************************************************************/


DEFINE_PROPERTY(mix_viscosity,c,t)
{
  real mu_lam;
  real mu_o2= 24.385e-6;
  real mu_n2= 19.799e-6;
  real mu_h2= 9.805e-6;
  real mu_h2o= 11.81e-6;

  mu_lam = mu_o2 * C_UDSI(c,t,0) + mu_h2o * C_UDSI(c,t,1) + mu_h2 *
C_UDSI(c,t,2)+ mu_n2 * C_UDSI(c,t,3);

        if (mu_lam <= 0.0)
        {
          mu_lam = 0.1e-6;
        }

  return mu_lam;

}


DEFINE_PROPERTY(mix_density, c, t)
{
   real rho;
   real P = 101325;
   real R = 8.3144;
        real T = C_T(c,t);

        rho = (P / (1000* R * T)) * ( 1/ ((C_UDSI(c,t,0)/32.)+ (C_UDSI(c,t,1)/18.)+
(C_UDSI(c,t,2)/2.)+ (C_UDSI(c,t,3)/28.)));

        if (rho > 1.109)
        {
                rho = 1.109;
        }

        return rho;

}



/************************************************************************/
/* UDF for specifying an momentum source term in a GDL and CL           */
/************************************************************************/

DEFINE_SOURCE(xmom_sourceC,c,t,dS,eqn)   /*  cathode x momentum source   */
{
  real x[ND_ND];
  real source;
  real mu = C_MU_L(c,t);
  real K;
```

```
 if (THREAD_ID(t) == 7)  /* cathode GDL */
 {
        K = 1.76e-11;
 }
 else if (THREAD_ID(t) == 8) /* cathode CL */
 {
        K = 1.76e-11;
 }

 C_CENTROID(x,c,t);
 source = - mu * C_U(c,t) / K;
 dS[eqn] = - mu / K;
 return source;
}


DEFINE_SOURCE(xmom_sourceA,c,t,dS,eqn)  /*  anode x momentum source   */
{
 real x[ND_ND];
 real source;
 real mu = C_MU_L(c,t);
 real K;
 if (THREAD_ID(t) == 3)  /* anode GDL */
 {
        K = 1.76e-11;
 }
 else if (THREAD_ID(t) == 4) /* anode CL */
 {
        K = 1.76e-11;
 }

 C_CENTROID(x,c,t);
 source = - mu * C_U(c,t) / K;
 dS[eqn] = - mu / K;
 return source;
}


DEFINE_SOURCE(ymom_sourceC,c,t,dS,eqn)  /*  cathode y momentum source   */
{
 real x[ND_ND];
 real source;
 real mu = C_MU_L(c,t);
 real K;
 if (THREAD_ID(t) == 7) /* cathode GDL */
 {
        K = 1.76e-11;
 }
 else if (THREAD_ID(t) == 8) /* cathode CL */
 {
        K = 1.76e-11;
 }

 C_CENTROID(x,c,t);
 source = - mu * C_V(c,t) / K;
 dS[eqn] = - mu / K;
 return source;
}
```

```
DEFINE_SOURCE(ymom_sourceA,c,t,dS,eqn) /*  anode y momentum source   */
{
  real x[ND_ND];
  real source;
  real mu = C_MU_L(c,t);
  real K;
  if (THREAD_ID(t) == 3) /* anode GDL */
  {
          K = 1.76e-11;

  }
  else if (THREAD_ID(t) == 4) /* anode CL */
  {
          K = 1.76e-11;

  }

  C_CENTROID(x,c,t);
  source = - mu * C_V(c,t) / K;
  dS[eqn] = - mu / K;
  return source;
}


DEFINE_SOURCE(zmom_sourceC,c,t,dS,eqn) /*  cathode z momentum source   */
{
  real x[ND_ND];
  real source;
  real mu = C_MU_L(c,t);
  real K;
  if (THREAD_ID(t) == 7) /*  cathode GDL   */
  {
          K = 1.76e-11;

  }
  else if (THREAD_ID(t) == 8) /*  cathode CL   */
  {
          K = 1.76e-11;

  }

  C_CENTROID(x,c,t);
  source = - mu * C_W(c,t) / K;
  dS[eqn] = - mu / K;
  return source;
}


DEFINE_SOURCE(zmom_sourceA,c,t,dS,eqn) /*  anode z momentum source   */
{
  real x[ND_ND];
  real source;
  real mu = C_MU_L(c,t);
  real K;
  if (THREAD_ID(t) == 3)
  {
```

```
        K = 1.76e-11;

 }
 else if (THREAD_ID(t) == 4)
 {
        K = 1.76e-11;

 }

 C_CENTROID(x,c,t);
 source = - mu * C_W(c,t) / K;
 dS[eqn] = - mu / K;
 return source;
}



/************************************************************************/
/* UDF for diffusivity in the porous zones                              */
/************************************************************************/


DEFINE_ANISOTROPIC_DIFFUSIVITY(diff_eff_O2,c,t,i,dmatrix)   /* Oxygen diffusion in
cathode side */


{

        real p = 101325;
        real p0 = 101325.0;
        real T = C_T(c,t);
        real T0 = 293.2;
        real diff = 0.22e-4;


        if (THREAD_ID(t) == 7) /* cathode GDL */
        {
                dmatrix [0][0]= diff * p0/p* pow((T/T0),1.5)* (0.4)*(pow(((0.4-
0.11)/0.89), 0.521));
                dmatrix [0][1]= 0.0;
                dmatrix [0][2]= 0.0;
                dmatrix [1][0]= 0.0;
                dmatrix [1][1]= diff * p0/p* pow((T/T0),1.5)* (0.4)*(pow(((0.4-
0.11)/0.89), 0.785));
                dmatrix [1][2]= 0.0;
                dmatrix [2][0]= 0.0;
                dmatrix [2][1]= 0.0;
                dmatrix [2][2]= diff * p0/p* pow((T/T0),1.5)* (0.4)*(pow(((0.4-
0.11)/0.89), 0.521));

        }

        else if (THREAD_ID(t) == 8) /* cathode CL */
        {
                dmatrix [0][0]= diff * p0/p* pow((T/T0),1.5)* (0.4)*(pow(((0.4-
0.11)/0.89), 0.521));
                dmatrix [0][1]= 0.0;
                dmatrix [0][2]= 0.0;
```

```
                dmatrix [1][0]= 0.0;
                dmatrix [1][1]= diff * p0/p* pow((T/T0),1.5)* (0.4)*(pow(((0.4-
0.11)/0.89), 0.785));
                dmatrix [1][2]= 0.0;
                dmatrix [2][0]= 0.0;
                dmatrix [2][1]= 0.0;
                dmatrix [2][2]= diff * p0/p* pow((T/T0),1.5)* (0.4)*(pow(((0.4-
0.11)/0.89), 0.521));
        }

        else {
                dmatrix [0][0]= diff * p0/p* pow((T/T0),1.5);
                dmatrix [0][1]= 0.0;
                dmatrix [0][2]= 0.0;
                dmatrix [1][0]= 0.0;
                dmatrix [1][1]= diff * p0/p* pow((T/T0),1.5);
                dmatrix [1][2]= 0.0;
                dmatrix [2][0]= 0.0;
                dmatrix [2][1]= 0.0;
                dmatrix [2][2]= diff * p0/p* pow((T/T0),1.5);
        }

 }



DEFINE_ANISOTROPIC_DIFFUSIVITY(diff_eff_H2O,c,t,i,dmatrix)  /* water vapour
diffusion in anode and cathode */
{

        real p = 101325;
        real p0 = 101325.0;
        real T = C_T(c,t);
        real T0 = 307.5;
        real diff = 0.256e-4;

        if (THREAD_ID(t) == 7) /* cathode GDL */
        {
                dmatrix [0][0]= diff * p0/p* pow((T/T0),1.5)* (0.4)*(pow(((0.4-
0.11)/0.89), 0.521));
                dmatrix [0][1]= 0.0;
                dmatrix [0][2]= 0.0;
                dmatrix [1][0]= 0.0;
                dmatrix [1][1]= diff * p0/p* pow((T/T0),1.5)* (0.4)*(pow(((0.4-
0.11)/0.89), 0.785));
                dmatrix [1][2]= 0.0;
                dmatrix [2][0]= 0.0;
                dmatrix [2][1]= 0.0;
                dmatrix [2][2]= diff * p0/p* pow((T/T0),1.5)* (0.4)*(pow(((0.4-
0.11)/0.89), 0.521));

        }

        else if (THREAD_ID(t) == 3) /* anode GDL */
        {
                dmatrix [0][0]= diff * p0/p* pow((T/T0),1.5)* (0.4)*(pow(((0.4-
0.11)/0.89), 0.521));
```

```
                dmatrix [0][1]= 0.0;
                dmatrix [0][2]= 0.0;
                dmatrix [1][0]= 0.0;
                dmatrix [1][1]= diff * p0/p* pow((T/T0),1.5)* (0.4)*(pow(((0.4-
0.11)/0.89), 0.785));
                dmatrix [1][2]= 0.0;
                dmatrix [2][0]= 0.0;
                dmatrix [2][1]= 0.0;
                dmatrix [2][2]= diff * p0/p* pow((T/T0),1.5)* (0.4)*(pow(((0.4-
0.11)/0.89), 0.521));

        }

        else if (THREAD_ID(t) == 8) /* cathode CL */
        {
                dmatrix [0][0]= diff * p0/p* pow((T/T0),1.5)* (0.4)*(pow(((0.4-
0.11)/0.89), 0.521));
                dmatrix [0][1]= 0.0;
                dmatrix [0][2]= 0.0;
                dmatrix [1][0]= 0.0;
                dmatrix [1][1]= diff * p0/p* pow((T/T0),1.5)* (0.4)*(pow(((0.4-
0.11)/0.89), 0.785));
                dmatrix [1][2]= 0.0;
                dmatrix [2][0]= 0.0;
                dmatrix [2][1]= 0.0;
                dmatrix [2][2]= diff * p0/p* pow((T/T0),1.5)* (0.4)*(pow(((0.4-
0.11)/0.89), 0.521));
        }

        else if (THREAD_ID(t) == 4) /* anode CL */
        {
                dmatrix [0][0]= diff * p0/p* pow((T/T0),1.5)* (0.4)*(pow(((0.4-
0.11)/0.89), 0.521));
                dmatrix [0][1]= 0.0;
                dmatrix [0][2]= 0.0;
                dmatrix [1][0]= 0.0;
                dmatrix [1][1]= diff * p0/p* pow((T/T0),1.5)* (0.4)*(pow(((0.4-
0.11)/0.89), 0.785));
                dmatrix [1][2]= 0.0;
                dmatrix [2][0]= 0.0;
                dmatrix [2][1]= 0.0;
                dmatrix [2][2]= diff * p0/p* pow((T/T0),1.5)* (0.4)*(pow(((0.4-
0.11)/0.89), 0.521));
        }

        else {
          /* cathode and anode gas channels */
                dmatrix [0][0]= diff * p0/p* pow((T/T0),1.5);
                dmatrix [0][1]= 0.0;
                dmatrix [0][2]= 0.0;
                dmatrix [1][0]= 0.0;
                dmatrix [1][1]= diff * p0/p* pow((T/T0),1.5);
                dmatrix [1][2]= 0.0;
                dmatrix [2][0]= 0.0;
                dmatrix [2][1]= 0.0;
                dmatrix [2][2]= diff * p0/p* pow((T/T0),1.5);
        }
```

```
}


DEFINE_ANISOTROPIC_DIFFUSIVITY(diff_eff_H2,c,t,i,dmatrix) /* Hydrogen diffusion
in anode side */
{
   real p = 101325;
        real p0 = 101325.0;
        real T = C_T(c,t);
        real T0 = 307.1;
        real diff = 0.915e-4;


        if (THREAD_ID(t) == 3) /* anode GDL */
        {
                dmatrix [0][0]= diff * p0/p* pow((T/T0),1.5)* (0.4)*(pow(((0.4-
0.11)/0.89), 0.521));
                dmatrix [0][1]= 0.0;
                dmatrix [0][2]= 0.0;
                dmatrix [1][0]= 0.0;
                dmatrix [1][1]= diff * p0/p* pow((T/T0),1.5)* (0.4)*(pow(((0.4-
0.11)/0.89), 0.785));
                dmatrix [1][2]= 0.0;
                dmatrix [2][0]= 0.0;
                dmatrix [2][1]= 0.0;
                dmatrix [2][2]= diff * p0/p* pow((T/T0),1.5)* (0.4)*(pow(((0.4-
0.11)/0.89), 0.521));

        }

        else if (THREAD_ID(t) == 4) /* anode CL */
        {
                dmatrix [0][0]= diff * p0/p* pow((T/T0),1.5)* (0.4)*(pow(((0.4-
0.11)/0.89), 0.521));
                dmatrix [0][1]= 0.0;
                dmatrix [0][2]= 0.0;
                dmatrix [1][0]= 0.0;
                dmatrix [1][1]= diff * p0/p* pow((T/T0),1.5)* (0.4)*(pow(((0.4-
0.11)/0.89), 0.785));
                dmatrix [1][2]= 0.0;
                dmatrix [2][0]= 0.0;
                dmatrix [2][1]= 0.0;
                dmatrix [2][2]= diff * p0/p* pow((T/T0),1.5)* (0.4)*(pow(((0.4-
0.11)/0.89), 0.521));
        }

        else {
                dmatrix [0][0]= diff * p0/p* pow((T/T0),1.5);
                dmatrix [0][1]= 0.0;
                dmatrix [0][2]= 0.0;
                dmatrix [1][0]= 0.0;
                dmatrix [1][1]= diff * p0/p* pow((T/T0),1.5);
                dmatrix [1][2]= 0.0;
                dmatrix [2][0]= 0.0;
                dmatrix [2][1]= 0.0;
                dmatrix [2][2]= diff * p0/p* pow((T/T0),1.5);
        }
```

```
}


/*********************************************************************/
/* Electrochemistry at cathode side: Activation overpotential        */
/*********************************************************************/


DEFINE_ADJUST(voltagecathode,d)
{
        Thread *t;
        cell_t c;
        real t_m = 0.23e-3;
        real R = 8.3144;
        real F = 96485.3;
        real P_o2;
        real mas_o2;
        real mas_h2o;
        real P0 = 101325;
        real wat_acv;
        real wat_acva;
        real dif;
        real P_ext;
        real P_sat;
        real dens_mem = 2000.0;
        real Mas_mem = 1.1;
        real wat_conc;
        real M_O2 = 32.0/1000;
        real concc;
        real conc_c;
        real div;
        real I_Lc;
        real n_concc;
        real Hd = 0.000254;
        real diffo;
        real diff_O2 = 0.22e-4;
        real T10 = 293.2;
        real P = 101325;
        real hm;
        real volume;
        real watcnc;
        real vol_tot;
        real watcncav;


        thread_loop_c(t,d)
        {
                if (THREAD_ID(t)== 8) /* cathode CL */
                {
                        begin_c_loop(c,t)
                        {
                                volume = C_VOLUME(c,t);

                                /* water vapour saturation pressure     */
                                dif = C_T(c,t) -273;
```

```
                                P_ext = 0.00644367 + 0.000213948*(dif)+3.43293e-
5* pow(dif,2.)-2.70381e-7*pow(dif,3.)+8.77696e-9*pow(dif,4.)-3.14035e-
13*pow(dif,5.)+3.82148e-14*pow(dif,6.);
                                P_sat = P0 * P_ext;

                                /* water activity */
                                mas_h2o = C_UDSI(c,t,1);
                                if (mas_h2o < 0)
                                        {
                                                mas_h2o =0.0;
                                        }
                                wat_acv = mas_h2o * C_R(c,t)* R * C_T(c,t)/(0.018 *
P_sat);

                                /* water concentration */
                                if (wat_acv <= 1)
                                        {
                                        watcnc = dens_mem * (0.043 + 17.8*
wat_acv - 39.8* pow(wat_acv, 2.) + 36 * pow(wat_acv,3.)) / Mas_mem;

                                        }
                                else if (wat_acv > 1)
                                        {
                                        watcnc = dens_mem * (14 + 1.4 * (wat_acv -
1)) / Mas_mem;
                                        }

                                vol_tot += volume;
                                watcncav += watcnc * volume;


                                mas_o2 = C_UDSI(c,t,0);
                                if (mas_o2 < 0)
                                {
                                        mas_o2 = 0;
                                }

                                /* partial pressure of oxygen in cathode catalyst layer
*/
                                P_o2 = mas_o2 * C_R(c,t)* R * C_T(c,t)/0.032;
                                C_UDMI(c,t,11)= P_o2;


                                /* concentration cathode */
                                concc = mas_o2 * C_R(c,t) /M_O2;
                                if (concc < 0)
                                {
                                        concc = 0.0;
                                }


                                /* reaction overpotential on cathode side */

                                div = C_UDSI(c,t,4) * 3.39/(2* 160 * 2.87e-5 *
(concc+0.00001));
                                C_UDMI(c,t,1) = ((R*C_T(c,t))/(2*0.5*F))* log(div +
sqrt(pow(div,2.)+1.));
```

```
                                if (C_UDMI(c,t,1) < 0)
                                {
                                        C_UDMI(c,t,1) = 0;
                                }
                        }
                        end_c_loop(c,t)
                }

        }
        watcncav /= vol_tot;
        thread_loop_c(t,d)
        {
                if (THREAD_ID(t) == 8)
                {
                        begin_c_loop(c,t)
                        {
                        C_UDMI(c,t,2) = watcncav;
                        }
                        end_c_loop(c,t)
                }
        }


}



/************************************************************************/
/* Electrochemistry at anode side:  Ohmic overpotential                 */
/************************************************************************/



DEFINE_ADJUST(voltageanode,d)
{
        Thread *t;
        cell_t c;
        real mcona;
        real t_m = 0.23e-3;
        real R = 8.3144;
        real F = 96485.3;
        real P_h2;
        real mas_h2o;
        real mas_h2;
        real P0 = 101325;
        real wat_acva;
        real dif;
        real P_ext;
        real P_sat;
        real dens_mem = 2000.0;
        real Mas_mem = 1.1;
        real wat_conc_ano;
        real ee;
        real nd;
        real ndav;
        real ex;
        real Dw;
        real alpha;
```

```
        real wat_conc;
        real div;
        real Mh2 = 2.0/1000;
        real conca;
        real P = 101325;
        real T20 = 307.1;
        real diff_H2 = 0.915e-4;
        real diffh;
        real Hd = 0.000254;
        real hm;
        real conc_a;
        real n_conca;
        real I_La;
        real volume;
        real watcna;
        real vol_tot;
        real watcnaav;
        real R_el = 0.1/(100 * 100);
        real Hm = 0.00023;
        real Km;
        real Dwav;

        thread_loop_c(t,d)
        {
                if (THREAD_ID(t)== 4) /* Anode CL */
                {
                        begin_c_loop(c,t)
                        {
                                volume = C_VOLUME(c,t);


                                /* water vapour saturation pressure */
                                dif = C_T(c,t) -273;
                                P_ext = 0.00644367 + 0.000213948*(dif)+3.43293e-
5* pow(dif,2.)-2.70381e-7*pow(dif,3.)+8.77696e-9*pow(dif,4.)-3.14035e-
13*pow(dif,5.)+3.82148e-14*pow(dif,6.);
                                P_sat = P0 * P_ext;

                                /* water activity*/
                                mas_h2o = C_UDSI(c,t,1);
                                if (mas_h2o < 0)
                                        {
                                                mas_h2o =0.0;
                                        }
                                wat_acva = mas_h2o * C_R(c,t)* R * C_T(c,t)/(0.018
* P_sat);

                                /* water concentration */
                                if (wat_acva <= 1)
                                        {
                                        watcna = dens_mem * (0.043 + 17.8*
wat_acva - 39.8* pow(wat_acva, 2.) + 36 * pow(wat_acva,3.)) / Mas_mem;

                                        nd = 0.0049 + 2.02* wat_acva - 4.53*
pow(wat_acva, 2.) + 4.09 * pow(wat_acva,3.);
                                        }
                                else if (wat_acva > 1)
                                        {
```

```
                                        watcna = dens_mem * (14 + 1.4 * (wat_acva
-1)) / Mas_mem;
                                        nd = 1.59 + 0.159 * (wat_acva -1);
                                        }

                                vol_tot += volume;
                                watcnaav += watcna * volume;
                                ndav += nd * volume;

                                /* water diffusion coefficient */
                                        ex = exp(2416.*((1/303.)-(1/C_T(c,t))));
                                        Dw = nd * 5.5e-11 * ex;
                                        Dwav += Dw * volume;


                                mas_h2 = C_UDSI(c,t,2);
                                if (mas_h2 < 0)
                                {
                                        mas_h2 = 0;
                                }

                                /* partial pressure of hydrogen in anode catalyst
layer*/
                                P_h2 = mas_h2 * C_R(c,t)* R * C_T(c,t)/0.002;
                                C_UDMI(c,t,10)= P_h2;

                                /* concentration anode */
                                conca = mas_h2 * C_R(c,t)/ Mh2 ;
                                if (conca < 0)
                                {
                                        conca = 0.0;
                                }


                                /* reaction overpotential on anode side */

                                div = (C_UDSI(c,t,4)/(2* 2e+8 * 2.87e-5)) *
sqrt(56.4/(conca + 0.00001));
                                C_UDMI(c,t,5) = ((R*C_T(c,t))/(4*0.5*F))* log(div +
sqrt(pow(div,2.)+1));


                                if (C_UDMI(c,t,5) < 0)
                                {
                                        C_UDMI(c,t,5) = 0;
                                }


                        }
                        end_c_loop(c,t)
                }
        }

        watcnaav /= vol_tot;
        ndav /= vol_tot;
        Dwav /= vol_tot;

        thread_loop_c(t,d)
```

```
        {
                if (THREAD_ID(t) == 4)
                {
                        begin_c_loop(c,t)
                        {
                        C_UDMI(c,t,3) = watcnaav;
                        C_UDMI(c,t,6) = ndav;
                        C_UDMI(c,t,7) = Dwav;

                        /* Membrane conductivity */
                                ee = exp(1268.*((1/303.)-(1/C_T(c,t))));
                                Km = 100.*(0.00514*(Mas_mem/dens_mem)*
C_UDMI(c,t,3)- 0.00326)* ee;

                                /* Ohmic overpotential  */
                                C_UDMI(c,t,9) = C_UDSI(c,t,4) * (R_el + (Hm / Km));

                        }
                        end_c_loop(c,t)
                }
        }


}


/*****************************************************************/
/* Net water transfer coefficient                                */
/*****************************************************************/


DEFINE_ADJUST(net_water_transfer,d)
{
        Thread *t;
        cell_t c;

        real F = 96485.3;
        real wat_conc_cat;
        real wat_conc_ano;
        real n_d;
        real D_w;
        real t_m = 0.23e-3;
        real alpha;
        real I;


thread_loop_c(t,d)
        {
        if (THREAD_ID(t) == 8) /* cathode CL */
                {
                        begin_c_loop(c,t)
                        {

                                wat_conc_cat = C_UDMI(c,t,2);
                        }
                                end_c_loop(c,t)
                }
        else if (THREAD_ID(t) == 4) /* anode CL */
```

```
		{
			begin_c_loop(c,t)
			{

			wat_conc_ano = C_UDMI(c,t,3);
			n_d = C_UDMI(c,t,6);
			D_w = C_UDMI(c,t,7);
			I = C_UDSI(c,t,4);
			}
			end_c_loop(c,t)
		}

		/* net water transfer coefficient */

			alpha = n_d - (((F * D_w * (wat_conc_cat -
wat_conc_ano))/((I+0.000001) * t_m)));
			if (alpha <0)
				{
					alpha = 0;
				}
			else if (alpha > 2.)
				{
					alpha = 2.;
				}
	}

	thread_loop_c(t,d)
	{
		if (THREAD_ID(t) == 8 || THREAD_ID(t) == 4)
		{
			begin_c_loop(c,t)
			{
			C_UDMI(c,t,8) = alpha;
			}
			end_c_loop(c,t)
		}
	}

}


/*****************************************************************/
/* Oxygen source term at cathode CL                              */
/*****************************************************************/



DEFINE_SOURCE(ox_con,c,t,dS,eqn)
{
  real x[ND_ND];
  real source;
  real F =96485.3;
  real M_O2 = 32.0/1000;
  real A = 0.00287/100;


			if (THREAD_ID(t) == 8)
				{
```

```
                                source = - C_UDSI(c,t,4) * M_O2 / (4 * F * A);
                                dS[eqn] = 0;
                                }

 else
 {
        source = dS[eqn] = 0;
 }
   return source;
}


/************************************************************************/
/* Hydrogen source term at anode CL                                     */
/************************************************************************/


DEFINE_SOURCE(H2_con,c,t,dS,eqn)
{
 real x[ND_ND];
 real source;
 real F =96485.3;
 real M_H2 = 2.0/1000;
 real A = 0.00287/100;


 if (THREAD_ID(t) == 4)
 {

                                source = - C_UDSI(c,t,4) * M_H2 / (2 * F * A);
                                dS[eqn] = 0;
                                }


 else
 {
        source = dS[eqn] = 0;
 }

 return source;
}


/************************************************************************/
/* Water vapour source term at cathode CL                               */
/************************************************************************/


DEFINE_SOURCE(CCL_water,c,t,dS,eqn)
{
 real x[ND_ND];
 real source;
 real F =96485.3;
 real M_H2O = 18.0/1000;
 real A = 0.00287/100;
```

```
  if (THREAD_ID(t) == 8)
  {

                                source = C_UDSI(c,t,4) * M_H2O * (1+ 2*
C_UDMI(c,t,8)) / (2 * F * A);
                                dS[eqn] = 0;
                                }

  else
  {
          source = dS[eqn] = 0;
  }

  return source;
}


/************************************************************************/
/* water vapour source term at anode CL                                 */
/************************************************************************/


DEFINE_SOURCE(ACL_water,c,t,dS,eqn)
{
  real x[ND_ND];
  real source;
  real F =96485.3;
  real M_H2O = 18.0/1000;
  real A = 0.00287/100;



  if (THREAD_ID(t) == 4)
  {

                                source = - C_UDSI(c,t,4) * M_H2O * C_UDMI(c,t,8) /
(F * A);
                                dS[eqn] = 0;
                                }

  else
  {
          source = dS[eqn] = 0;
  }

  return source;
}




/************************************************************************/
/* Cell Voltage at average current density                              */
/************************************************************************/

DEFINE_ADJUST(cellvoltage,d)
{
```

```
        Thread *t;
        cell_t c;
        real F = 96485.3;
        real E;
        real R = 8.314;
        real Po2;
        real Ph2;
        real n_cat;
        real n_anod;
        real U;
        real n_ohm;
        real n_concc;
        real n_conca;
        real T;
        real diff_H2 = 0.915e-4;
        real diffh;
        real Hd = 0.000254;
        real hm;
        real conc_a;
        real I_La;
        real conc_c;
        real I_Lc;
        real diffo;
        real diff_O2 = 0.22e-4;
        real P0 = 101325;
        real P = 101325;
        real T10 = 293.2;
        real T20 = 307.1;


thread_loop_c(t,d)
        {

        if (THREAD_ID(t) == 8) /* cathode CL */
                {
                        begin_c_loop(c,t)
                        {

                                Po2 = C_UDMI(c,t,11)/101325.0;
                                n_cat = C_UDMI(c,t,1);

                                T = C_T(c,t);
                        }
                                end_c_loop(c,t)
                }

        else if (THREAD_ID(t) == 4) /* anode CL */
                {
                        begin_c_loop(c,t)
                        {

                        Ph2 = C_UDMI(c,t,10)/101325.0;
                        n_anod = C_UDMI(c,t,5);

                        n_ohm = C_UDMI(c,t,9);
                        }
                        end_c_loop(c,t)
```

```
        }

    else if (THREAD_ID(t) == 7) /* Cathode GDL */
        {
            begin_c_loop(c,t)
            {

                /* cathode concentration overpotential */
                diffo = diff_O2 * P0/P *
pow((C_T(c,t)/T10),1.5)*(0.4)*(pow(((0.4-0.11)/0.89), 0.785));
                conc_c = 0.21 * P / (R * C_T(c,t));
                I_Lc = (2* F* conc_c * diffo)/ Hd;
                C_UDMI(c,t,13) = - (R*C_T(c,t)/(2 * F))* log(1 -
(C_UDSI(c,t,4)/I_Lc));
                n_concc = C_UDMI(c,t,13);
            }
            end_c_loop(c,t)
        }

    else if (THREAD_ID(t) == 3) /* anode GDL */
        {
            begin_c_loop(c,t)
            {

                /* anode concentration overpotential */
                diffh = diff_H2 * P0/P *
pow((C_T(c,t)/T20),1.5)*(0.4)*(pow(((0.4-0.11)/0.89), 0.785));
                conc_a = 0.69 * P / (R * C_T(c,t));
                I_La = (2* F* conc_a * diffh)/ Hd;
                C_UDMI(c,t,14) = - (R*C_T(c,t)/(2 * F))* log(1 -
(C_UDSI(c,t,4)/I_La));
                n_conca = C_UDMI(c,t,14);

            }
            end_c_loop(c,t)
        }

    /* equilibrium thermodynamic potential- Nernst Equation */

            E = 1.23 - (0.9e-3 * (T - 298.0))+ 2.3* (R * T /(4*F))*
log(pow(Ph2, 2.)* Po2);

            if (E <0)
                {
                    E = 0;
                }
            else if (E > 1.23)
                {
                    E = 1.23;
                }

            if ( n_concc <0.0)
                {
                    n_concc = 0.0;
                }
                else if (n_concc > 1.23)
                {
                    n_concc = 1.23;
```

```
                }

            /* cell voltage */
            U = E - n_cat - n_anod - n_ohm - n_conca- n_concc;

            if (U <0.0)
                {
                    U = 0.0;
                }
            else if (U > 1.23)
                {
                    U = 1.23;
                }

}

    printf("Cell Voltage: %0.6f, %0.6f, %0.6f, %0.6f, %0.6f, %0.6f, %0.6f\n", E,
n_cat, n_anod, n_ohm, n_concc, n_conca, U);

}


/************************************************************************/
/* Nitrogen mass fraction at cathode side                               */
/************************************************************************/



DEFINE_ADJUST(nitro,d)
{
    Thread *t;
    cell_t c;


thread_loop_c(t,d)
    {
    if (THREAD_ID(t) == 6) /* cathode GC */
        {
            begin_c_loop(c,t)
            {
                C_UDSI(c,t,3)= 1- C_UDSI(c,t,0) - C_UDSI(c,t,1)-
C_UDSI(c,t,5);
            }
                end_c_loop(c,t)
        }
    else if (THREAD_ID(t) == 7) /* cathode GDL */
        {
            begin_c_loop(c,t)
            {
            C_UDSI(c,t,3)= 1- C_UDSI(c,t,0) - C_UDSI(c,t,1)-
C_UDSI(c,t,5);
            }
            end_c_loop(c,t)
        }
    else if (THREAD_ID(t) == 8) /* cathode CL */
        {
            begin_c_loop(c,t)
            {
```

```
                        C_UDSI(c,t,3)= 1- C_UDSI(c,t,0) - C_UDSI(c,t,1)-
C_UDSI(c,t,5);
                        }
                        end_c_loop(c,t)
                }

        }
}


/*****************************************************************************/
/**********      Single Phase V a.10                                 ***********/
/*****************************************************************************/
/*****************************************************************************/
```

Appendix B: Publications

Journal Papers:

1. Numerical study of the effect of effective diffusivity coefficient and permeability of gas diffusion layer on fuel cell performance. Submitted to: **IMECHE Journal of Power and Energy** (Accepted JPE 1373).

2. Investigation of species transport in a gas diffusion layer of a polymer electrolyte membrane fuel cell through two-phase modelling. Submitted to: **Renewable Energy, Elsevier**. (Under Review)

3. Water dynamics inside a cathode channel of a polymer electrolyte membrane fuel cell. Submitted to: **Renewable Energy**, Elsevier. (Under Review)

4. Parametric sensitivity analysis of three-dimensional PEM fuel cell models.
   Going to be submitted to: **International Journal of Energy Research**. John Wiley & Sons

Conference Papers:

S. Z. Islam, M. Hossain, P. Pollard, A parametric study to predict performance of proton exchange membrane fuel cell. 4th World Hydrogen Technologies Convention, September 2011, Glasgow. UK. (Paper No: 0130)

Presentation:

- Northern Research Partnership (NRP), Graduate Student Symposium, University of Aberdeen, Aberdeen, UK, August, 2009. (**Best Presentation Award)**

- Northern Research Partnership (NRP), Graduate Student Symposium, University of Dundee, UK, January, 2011.
